Control and Enhancement of Saturated Flow-Boiling Thermal Conductance and Crisis with Porous Metasurfaces: Hydrodynamic-Stability and Capillary-Viscous Limit Theories, Direct Simulations, and Experimental Verification

by

Júlio Ferreira

A dissertation submitted in partial fulfillment
of the requirements for the degree of
Doctor of Philosophy
(Mechanical Engineering)
in the University of Michigan
2022

Doctoral Committee:

 Professor Massoud Kaviany, Chair
 Associate Professor Eric Johnsen
 Professor Annalisa Manera
 Professor William Schultz

Júlio Ferreira

fjulio@umich.edu

ORCID iD: 0000-0001-9881-6080

DEDICATION

To my parents, my brother, my two cats, and then my wife, in no particular order.

ACKNOWLEDGMENTS

TABLE OF CONTENTS

LIST OF FIGURES

viii

LIST OF TABLES

LIST OF APPENDICES

NOMENCLATURE

A	area (m^2)
Bo_L	Bond number, $\frac{(\rho_l - \rho_g)gL^2}{\sigma}$
b	systematic uncertainty
C	constant, inertial coefficient
c_d	discharge coefficient
C_J	Leverett constant
c_p	heat capacity (J/kg-K)
D, d	diameter (m)
E	turbulent kinetic energy (J/kg), energy (J)
Eo_L	Eötvos number, $\frac{(\rho_l - \rho_g)gL^2}{\sigma}$
F	force (N)
f	phase identifier, friction factor
Fr_L	Froude number, $\left[\frac{\rho_l u_{l,\text{o}}^2}{g(\rho_l - \rho_g)L}\right]^{1/2}$
G/A	thermal conductance [K/W-m^2]
G	filter function)
g	gravity (m/s^2)
H, h	height (m)
Δh_{lg}	heat of evaporation (kJ/kg)
$J(s)$	Leverett function
K	permeability (m^2), coverage factor
k	thermal conductivity (W/m-K)
k_B	Boltzmann constant (J/K)
L, l	length (m)
M	molar mass (kg/kmol)
$\dot{M}$	mass flow rate (kg/s)
Ma_g	Mach number, $\frac{v_{g,\text{o}}}{u_a}$
N	number
p	pressure (Pa)
P	first velocity gradient invariant (1/s)
Q	heat flow rate (W), second velocity gradient invariant ($1/\text{s}^2$)
q	heat flux (W/m^2)
r	radius (m)
R	curvature radius (m), third velocity gradient invariant ($1/\text{s}^3$)

Re_L	Reynolds number, $\frac{\rho_f u_f L}{\mu_f}$
$\boldsymbol{S}$	symmetric part of strain rate tensor (1/s)
s	random uncertainty
t	time (s)
T	temperature (K,°C)
$\boldsymbol{u}$	velocity vector (m/s)
u	axial velocity (m/s), combined uncertainty
U	expanded uncertainty
$u_{l,\mathrm{o}}$	inlet liquid velocity (m/s)
u_a	speed of sound (m/s)
v	lateral velocity (m/s)
V	volume (m^3)
w	perpendicular velocity (m/s), liquid track (m)
W, w	width (m)
We_L	Weber number, $\frac{\rho_l u_{l,\mathrm{o}}^2 L}{\sigma}$
X	generic parameter
x	axial position (m)
y	lateral position (m)
z	perpendicular position (m)
Z	Melrose function
Z_m	dimensionless figure of merit

Greek symbols

α	void fraction
Γ	blending function
γ	heat capacity ratio
Δ_p	post spacing (m)
δ	liquid thickness (m), interfacial perturbation
δ_{ij}	Kronecker delta
ϵ	porosity
ε	turbulent dissipation rate (J/kg-s)
θ_c	contact angle
κ	wavenumber (1/m)
κ_{vK}	von Karman constant
λ	length scale (m), wavelength (m)
μ	dynamic viscosity (Pa-s)
ν	kinematic viscosity (m^2/s)
ρ	density (kg/m^3)
σ	surface tension (N/m)
σ_{ij}	viscosity stress tensor
τ_{ij}	shear stress tensor
ω	vorticity (1/s)

Ω	antisymmetric part of strain rate tensor (1/s)
ϕ	inclination angle , generic variable
φ	level-set function
$\Delta\varphi$	voltage (V)

Subscripts

c	capillary, critical
ca	canopy
ch	channel, choking
CHF	critical heat flux
$c\text{-}v$	capillary-viscous
e	evaporator
f	fluid
g	gas/vapor
h	hydrodynamic
i	index
j	index
k	index
K	Kolmogorov
KH	Kelvin-Helmholtz
l	liquid, levee
lg	liquid-gas phase change
max	maximum
min	minimum
n	normal
o	outlet
p	particle, post
per	perforation
ps	plain surface
RT	Rayleigh-Taylor
s	surface
sgs	subgrid scale
sh	superheat
t	turbulent
w	wick, wicking
Z	Zuber

Others

$\overline{}$	temporal average
$\sim$	filtered
$'$	perturbation/fluctuation

$\langle \ \rangle$ spatial average

$*$ dimensionless

LIST OF ABBREVIATIONS

C-GMR	Confined-Geometric Modulation Regime
CFD	Computational Fluid Dynamics
CHF	Critical Heat Flux
CSF	Continuum Surface Force
DNB	Departure from Nucleate Boiling
DNS	Direct Numerical Simulation
FBCW	Flow-Boiling Canopy Wick
GMR	Geometric Modulation Regime
LBM	Lattice-Boltzmann Method
LES	Large Eddy Simulation
MAE	Mean Absolute Error
PID	Proportional Integral Differential
PLIC	Piecewise-Linear Interface Calculation
RANS	Reynolds-Averaged Navier-Stokes
TIM	Thermal Interface Material
WMR	Wavelength Modulation Regime

ABSTRACT

CONTROL AND ENHANCEMENT OF SATURATED FLOW-BOILING THERMAL CONDUCTANCE AND CRISIS WITH POROUS METASURFACES: HYDRODYNAMIC-STABILITY AND CAPILLARY-VISCOUS LIMIT THEORIES, DIRECT SIMULATIONS, AND EXPERIMENTAL VERIFICATION

Flow-boiling heat transfer is used in high heat flux and thermal conductance applications and is bounded by the boiling crisis, i.e., the critical heat flux (CHF). This is when the vapor generation in the leading-edge region of the forced liquid flow over the heated surface intensifies, interrupting the liquid supply to the surface (dryout) resulting in rapid surface temperature rise. The thermal-hydraulic triggering this phenomenon and its control has been at the center of boiling heat transfer research. In this study, the flow-boiling crisis mechanism is investigated in the near-field region, as an extension to the Zuber pool-boiling hydrodynamic instability theory. This is the coupled interfacial Kelvin-Helmholtz and Rayleigh-Taylor instabilities of downward liquid flow countered by rising vapor columns arranged in a 2-D periodic unit cell based on the critical wavelength. We also analyze the far-field region, tracking the liquid-vapor turbulent two-phase flow using CFD with the large eddy simulations and down to the Kolmogorov scale. The control of the crisis is achieved with porous metasurfaces (periodic, 3-D multiscale capillary structures). The theoretical analyses are accompanied by direct numerical simulations and predict the flow-boiling crisis and lead to introduction of two CHF enhancement regimes, the *wavelength modulation* and the *geometric modulation* regimes, and these predictions are verified experimentally for saturated water flow boiling.

In the Zuber theory, the critical wavelength marks the onset of dryout and depends on the fluid properties. This wavelength was previously controlled using modulated porous surface coatings, increasing the CHF from the Zuber limit to the capillary-length limit. Here, this wavelength modulation is achieved with the liquid velocity and the relation among the liquid velocity, the critical wavelength and the CHF is developed and verified with the existing experimental data for plain surfaces. The leading-edge liquid track shear instability theory of flow-boiling crisis is introduced and verified by the direct numerical simulations.

To achieve yet higher CHF, the geometry of the Zuber unit cell is modified for flow boiling using aligned, rectangular and leveed vapor sites designed to reduce shearing of the leading-edge surface liquid track. This geometric modulation regime results in a very large hydrodynamic CHF. This unit-cell based surface is realized experimentally with a porous metasurface, i.e., the flow-boiling canopy wick (FBCW). The FBCW is a periodic, 3-D porous and perforated structure enabling capillary separation of the liquid and vapor and their direction along low resistance paths. The porous canopy separates the liquid channel flow from the vapor space beneath it and the canopy is connected to porous posts delivering liquid to a thin evaporator wick. The vapor generated on the meniscus flows through the vapor space between the posts and escapes into the channel through the canopy perforations (vapor flow sites) interacting with the flowing liquid. The FBCW results in large hydrodynamic CHF and thermal conductance, however, the FBCW internal wick flow resistance, i.e., the capillary-viscous limit, may become the bottleneck. This capillary-viscous CHF is predicted by point-wise (direct simulations), volume-averaged (using effective properties), and resistance-network treatments.

A collaborative-work fabrication (multimold, oven sintered copper particles), optimization and testing of the FBCW with saturated water at one atm, verifies the wavelength and geometric modulation regimes. The maximum measured CHF of $5.1\,\mathrm{MW/m^2}$ is within the geometric modulation regime and controlled by the capillary-viscous limit. The maximum measured thermal conductance is $0.36\,\mathrm{MW/m^2}$-K. Both are record values.

CHAPTER 1

Introduction

In this chapter, a brief overview of the boiling heat transfer and its limit, the so-called critical heat flux and thermal conductance (heat transfer coefficient) are introduced. Attempts to increase the critical heat flux, in relation to various applications, in particular the current challenges in thermal management of high heat flux devices, are also discussed. There has also been theoretical treatments of the flow boiling crisis, suggesting various crisis triggering mechanisms. A historical perspective on these and the current opportunities for further insight into the crisis and its control with engineered surface structures are also discussed. The chapter ends presenting the objectives of this work and the routine of the dissertation.

1.1 Significance of Boiling Heat Transfer

Boiling is the phase change process in which liquid is turned into vapor by the addition of heat [1]. Pool boiling refers to lower horizontal surface heating of a pool of saturated liquid and under gravity bubbles rise from the surface and a counterflow liquid replenishes the surface for a steady heat transfer. There is no net mass flow rate [2]. Flow boiling generally refers to a forced liquid flow augmenting the phase-density buoyant flow occurring in pool boiling [3]. In the literature, the tilted heated surface condition is also referred to as flow boiling. Boiling is characterized with variation of the variation of the surface superheat, which is the surface temperature above the fluid saturation temperature (which depends on the pressure), with the surface heat flux. Under nucleate boiling [4], the surface superheat can be rather small (large thermal conductance), which is very

desirable. So, in general boiling, which uses change in the physical bond between molecules [5] is more effective that single-phase heat transfer which uses only the sensible heat. One of the oldest and relevant application is in boilers (which are also a component in power plants) [6].

In gas-liquid two-phase flows, the phase distributions has characteristic topologies called the flow patterns or flow regimes [7]. Flow patterns can affect key parameters from two-phase flows (e.g., pressure drop, phasic slip ratio), and are a useful tool in the analysis and diagnostics of two-phase flows [3], in fact, even the simplest phase distribution can have complex hydrodynamics [8]. In flow boiling, different from adiabatic (no phase change) two-phase flows, different flow patterns can occur simultaneously in different portions of the stream, increasing the complexity of the problem [9]. Vapor is generated at the heated surface and transported downstream by the liquid inertia, changing the phase distribution along the flow [10].

Due to its inherent complexities, the study of boiling has been mostly empirical [11, 12]. The use of visualization techniques including high-speed cameras and other imaging techniques (e.g., particle image velocimetry, laser induced fluorescence) provide visual evidence to support the construction of physical models [13, 14, 15, 16]. Also, with the recent advances in computational capabilities, high-fidelity computational models have been used to simulate and predict the flow boiling phenomena. A review of the computational treatments of various aspects of flow boiling is given in [17]. In [18], an extensive review of flow boiling applications using CFD solvers is presented. Most investigations consider low and moderate pressures, close to the saturated states (although there are also subcooled boiling studies), and a review on flow boiling at high reduced pressure is available in [19].

1.2 History of Boiling Crisis Theories

The boiling crisis marks and leads to the dryout of the heated surface, resulting in the sudden rise in the surface and if not mitigated the meltdown [20]. This occurs at high heat flux and is marked as the critical heat flux (CHF). The co-occupancy and competition between the liquid and vapor

phase is dynamically played out (hydrodynamics) as the liquid moves toward the surface while the vapor escapes from it. The theoretical prediction of the CHF has attracted much attention and also proven to be rather challenging.

The link between the CHF and the hydrodynamic effects was first suggested in [21]. In [22], for pool boiling, it was proposed that the interaction between two distinct interfacial instability mechanisms, namely the Rayleigh-Taylor and the Kelvin-Helmholtz, would create the conditions for the rising vapor generated at the heated surface to prevent the downward liquid supply, leading to dryout. This mechanism was further investigated in [23, 24, 25] and it is discussed in further detail in Section 2.1.

The destabilizing effect of vapor recoil was also suggested as a mechanism responsible for the boiling crisis [26]. The vapor recoil force consists of a non-uniform pressure acting on the liquid-vapor interface near the contact line that increases with the evaporation rate, causing the liquid film to recede, drying the surface. The thickness of the wetting layer reflects the magnitude of the vapor recoil pressure force. The uncontrollable growth of dry spots underneath the generated vapor bubbles is proposed as the trigger mechanism for the CHF [27].

Due to the prevalence of boiling heat transfer in engineering applications, the accurate description of the boiling crisis phenomenon remains a very active research field. In [28], using a transparent heater (also used in [29]), high-speed imaging is employed to gain new insights on the surface dryout by monitoring the dry spot thermal behavior. The authors suggest that at a dry spot becomes irreversible when its temperature surpasses a critical temperature, found from 3-D conduction simulations of the heater, preventing the liquid supply from ever reaching the dry spot again. In this model, the liquid film recession caused by the vapor recoil force from neighboring evaporation sites contributes to the expansion of the irreversible dry spot. The growth of this irreversible dry spot is uncontrollable and triggers the boiling crisis.

Direct numerical simulation of boiling is often used to generate new insights into the boiling crisis. The CHF trigger mechanism is investigated using the Lattice Boltzmann Method (LBM) in [30]. The authors simulate the dynamics of the wet and dry portions of the surface, decomposing

the wall heat flux into wet and dry components. The wet heat flux component dominates, but as the dry fraction of the area increases due to the increasing wall superheat, a maximum is reached which is the CHF. The driving force for the dry area fraction increase is associated with the vapor recoil force. This mechanism was further investigated in [31] for a large number of vapor sites. The stochastic characteristic of the vapor nucleation in boiling was incorporated by using statistical distributions and the boiling crisis was triggered when the number of isolated nucleation sites reached a maximum, after which any new nucleation site would lead to coalescence and the increase of the nonrewettable dry area. In [32], the boiling mechanism is described by a reduction in the fluid density using the LBM. The authors found this effect to be more pronounced in concave corners, in agreement with the previous observations of vapor nucleation inside cavities.

Although the boiling crisis, the focus of this study, is a phenomenological instability governed by microscopic interfacial instabilities (i.e., Kelvin-Helmholtz and Rayleigh-Taylor), other types of instabilities can occur in flow boiling. A thorough review on other flow boiling static (e.g., flow excursion, flow pattern transition) and dynamic instabilities (e.g., density wave oscillations, pressure drop oscillations, thermal oscillations) is given in [33]. Recent studies including experiments [34] and physical modeling [35] of flow boiling under subcooled conditions are available (the boiling crisis is often called departure from nucleate boiling, DNB). A comprehensive review on the experimental and physical modeling efforts to characterize this phenomenon including the construction of a flow regime map is given in [36].

In this study, boiling crisis is viewed as the unit-cell vapor-liquid surface conditions and flow as proposed by Zuber based on the Kelvin-Helmholtz and Rayleigh-Taylor instabilities, and the goal is to control the crisis by altering the conditions using porous metasurfaces. These porous metasurfaces generate vapor through meniscus evaporation (not bubble nucleation) and are able to separate and direct the phases to increase the dryout limit.

1.3 History of Boiling Enhancements

The physics of the boiling crisis trigger mechanism offers insights into ways of controlling and enhancing the CHF. There is about a century of boiling heat transfer research [37]. In the last few decades, there has been active research on enhancing boiling CHF. In [38], these efforts are divided into four main categories: fluid properties improvement, usually by the addition of nanoparticles; surface modification with intricate fabrication techniques to alter the heated surface, favoring bubble nucleation or improving the liquid and vapor flow paths; modified channel structures to create mini/microchannels for instability inhibition; and hybrid techniques, where a combination of the three techniques is used (e.g., surface coating on microchannels).

Regarding the first category, improvement of fluid properties, despite many studies reaching an agreement regarding the CHF enhancement by nanofluids, no major consensus exists about the physical mechanism responsible for this enhancement in both pool and flow boiling configurations. One feature of this technique is that nano-particles deposit on the heated surface, thus influencing bubble nucleation, etc. [39], and there is some lingering debate about the criteria for performance enhancement over the base fluid. Additionally, there are several practical challenges and questions regarding the long term use of nanofluids in engineering applications [40].

Great interest has been elicited by the second category, surface modification, with several studies on the CHF and thermal conductance enhancements in recent years. The use of nanoscale surface coatings with various deposition methods (e.g., electrochemical deposition, chemical vapor deposition, etc.) for wettability control and nanoscale porous coatings for superheat reduction is reported in [41]. The authors also mention recent studies using carbon nanotubes and nanowire coatings to increase nucleation sites for pool boiling.

In [42], the authors analyze flow-boiling CHF enhancement by length scale (namely milli, micro, and nanoscales). The milliscale consists of the use of pin fins, channel inserts and ribbed walls with moderate CHF enhancement at the cost of significantly increasing the pressure drop. At the microscale, the use of porous coatings and foams is reported to increase the flow boiling heat transfer performance. A review on the use of microscale modulated porous structures, the

so-called porous metasurfaces, is given in [43]. This capillary, porous structures are employed to ensure liquid supply to the heated surface, separating the competition between liquid and vapor flows, thus enhancing the CHF. Additionally, the thermal conductance enhancement is observed due to the formation of menisci in the porous wick that leads to meniscus evaporation, requiring smaller superheat. The use of porous metasurfaces for CHF and thermal conductance enhancement is further discussed in Chapter 4.

The use of microchannels for CHF enhancement follows the miniaturization trend in electronics with the ever increasing heat flux density needs. An analysis of evaporation differences in both micro and macroscales is given in [44]. The author analyzes various experimental studies and suggests that in a microchannel, the hydraulic diameter is of the same scale as the bubble departure diameter, indicating that only one bubble can exist in the channel. In [42], suppression methods of the main two-phase flow instabilities observed in microchannels, namely severe pressure drop oscillation [45], capable of triggering premature CHF, and mild parallel channel instability, are discussed. Upstream throttling, downstream expansion, and vapor venting are some of the instability suppression methods revised by the authors. These were shown to reduce the microchannel pressure drop.

The most recent advances in flow boiling enhancements with enhanced microchannels, a combination of microchannels and surface modification techniques, are discussed in [46]. The CHF and thermal conductance enhancements are achieved by either surface coatings such as porous layers and nanostructures which increase the heat transfer area and favor bubble nucleation, or modified flow passages with micro pin fins or porous microchannels which enhance flow distribution, modifying the two-phase flow pattern. Concerns regarding the durability of enhanced microchannels, increased pressure drop, and fabrication difficulties have prevented its wide application.

Under reduced gravity, such as space applications, the inertial force is the solely responsible for controlling bubble growth and establishing the liquid supply. A review of the experimental methods and flow-boiling CHF enhancement in microgravity with liquid inertia is available in [47].

In this work, the inertia of liquid and the use of porous microstructures will be addressed for saturated water (one atm) flow boiling. These enhancements, however, are not limited to water as the working fluid and to the near-saturation conditions. A thorough review on CHF enhancement for a wide range of fluids including refrigerants and synthetic coolants (e.g., R-134a, FC-72) for the various enhancement techniques (e.g., mini/microchannels, nanofluids, surface coatings) is given in [48].

1.4   Objective of Thesis

The major objective of this study is to explore means for delaying the flow boiling crisis to achieve even higher CHF and thermal conductance limits. The first step is to understand the fundamental forces in the interaction and competition between the liquid and vapor phases leading to the boiling crisis. This understanding is leveraged to potentialize the contributing factors, leading to significant performance enhancements. By using direct simulations, the trigger mechanism of leading-edge surface liquid track destabilization by the vapor flows is postulated in a wavelength modulation regime controlled by the inlet liquid velocity.

Beyond the wavelength modulation, the control of the liquid and vapor flow paths is investigated and the phase-change mechanism is altered through the usage of porous metasurfaces which enable meniscus evaporation. Metasurfaces allow for the control of vapor sites geometry, replacing the columnar vapor jets with optimally arranged vapor space and venting sites, thus increasing the CHF. Direct simulations and experimental validations are used to verify the propositions and the predicted CHF and thermal conductance enhancements.

The document is organized as follows: In Chapter 2, the two-phase flow interfacial instability is discussed in light of the boiling crisis. The flow-boiling crisis trigger mechanism is presented as an extension to the current pool boiling theory and the flow of inlet liquid velocity and the inertial force is clarified. Chapter 3 presents the direct numerical simulation of the flow-boiling crisis to verify the proposed CHF trigger mechanism and a characteristic wavelength modulation

7

regime is identified. In Chapter 4, the CHF and thermal conductance enhancement through the use of porous metasurfaces is presented and a new multiscale porous metasurface, the flow-boiling canopy wick, is proposed. Chapter 5 discusses the limitations introduced by the use of the FBCW and the relevancy of wick effective properties, and Chapter 6 uses direct numerical simulations to verify said limits and estimate the wick properties. In Chapter 7, a novel, more effective regime of CHF modulation is proposed based on the vapor sites and their geometric confinement, and in Chapter 8, direct numerical simulations are performed to verify these enhancements in both the geometric and confined-geometric modulation regimes. Chapter 9 discusses the fabrication and testing of the FBCW in a flow-boiling loop. The experimental results are compared to the numerical results in Chapter 10, showing good agreement and validating the adopted assumptions. Final remarks and conclusions are summarized in Chapter 11 and extensions to the present work are suggested in Chapter 12. Appendix A presents an overview on uncertainty propagation for the measured quantities and Appendix B discusses the visualization of the phase-interactions in experimental and numerical video recordings.

CHAPTER 2

Flow-boiling Crisis Hydrodynamics-Stability Theory: Wavelength Modulation Regime of Hydrodynamic Critical Heat Flux

In this chapter, the roles of the two-phase flow interfacial instabilities in the boiling crisis are discussed. Flow-boiling crisis theory is presented as an extension to the pool boiling definition mentioned in Section 1.2 and a formal physical treatment for the hydrodynamic CHF enhancement reported in Section 1.3 is presented. A novel mechanism responsible for triggering the flow-boiling crisis is proposed, the surface liquid-track dryout model, and the role of the flow inlet velocity on the hydrodynamic CHF modulation is explained.

2.1   Zuber Pool-Boiling CHF Theory and Unit Cell

Horizontal two-phase flow initially arranged in stratified regime is subject to instabilities resulting from relative motion between the phases [49]. Traditional linear stability analysis considers the interface between the liquid and vapor (gas) phases to be planar and horizontal with the phases moving with axial velocities u_g and u_l, neglecting viscous effects [50]. The balance of gravity, inertia and surface tension forces are considered with the vapor (less dense) occupying the top portion of the channel and the liquid (more dense) at the bottom. The full derivation is available in [50, 51]. The Kelvin-Helmholtz (K-H) instability arises when the relative velocity is larger than
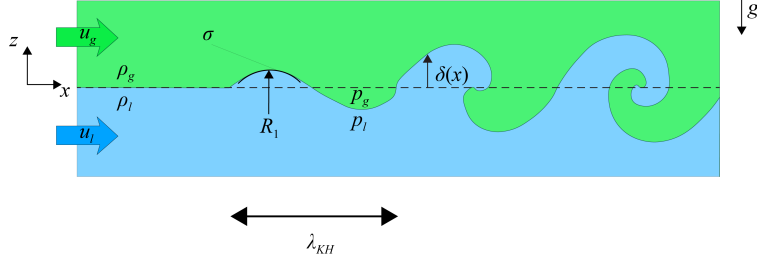
Figure 2.1: Evolution of interfacial instability on a horizontal stratified liquid-vapor interface and the Kelvin-Helmholtz instability and wavelength.

some critical value $|u_g - u_l| = u_c$, this is illustrated in Figure 2.1. The corresponding K-H critical wavelength is

$$\lambda_{\text{KH}} = \lambda_c = 2\pi \left[\frac{\sigma}{g \left(\rho_l - \rho_g \right)} \right]^{1/2}. \tag{2.1}$$

Viscous force effects on the critical velocity and critical wavelength are considered in [52] for air and water and found to be negligible.

In a different configuration, if the more dense phase is on top and both phases are at rest ($u_g = u_l = 0$), gravity-induced movement will occur at the interface and the Rayleigh-Taylor (R-T) instability arises with the critical wavelength (the most dangerous wavelength), this is illustrated in Figure 2.2

$$\lambda_{\text{RT},d} = 3^{1/2} 2\pi \left[\frac{\sigma}{g \left(\rho_l - \rho_g \right)} \right]^{1/2} = 3^{1/2} \lambda_c. \tag{2.2}$$

Both the K-H and R-T critical wavelengths are related. Both Eqs. (2.1) and (2.2) can be expressed with the Bond (or Eötvos) number (would become equal to 2π and $3^{1/2} 2\pi$), which is the ratio of buoyancy and surface tension forces

$$\text{Bo}_\lambda = \frac{g \left(\rho_l - \rho_g \right) \lambda_c^2}{\sigma} = \frac{\text{We}_\lambda}{\text{Fr}_\lambda^2}, \tag{2.3}$$

where the Froude and Weber numbers are a ratio of the inertial and gravity forces and a ratio of the

10
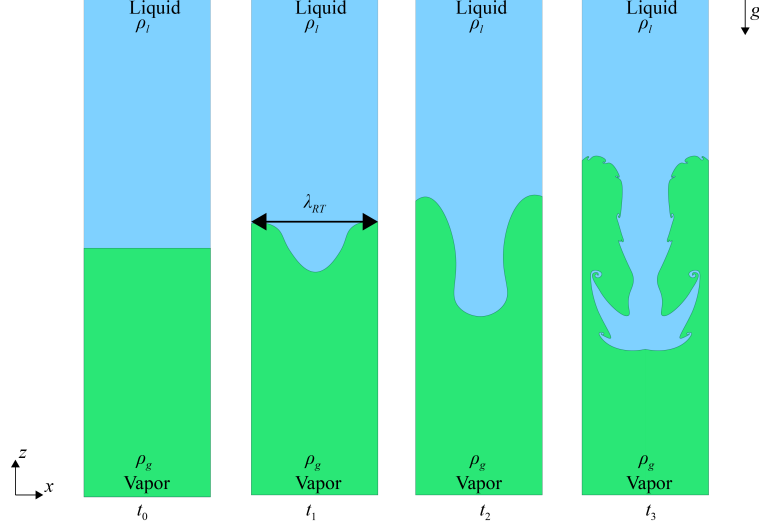
Figure 2.2: Evolution of the interfacial instability on horizontal liquid-vapor interface and the formation of the Rayleigh-Taylor instability and wavelength.

inertial and surface tension forces, respectively

$$\text{Fr}_\lambda = \left[\frac{\rho_l u_{l,o}^2}{g\left(\rho_l - \rho_g\right)\lambda_c}\right]^{1/2} ; \ \ \text{We}_\lambda = \frac{\rho_l u_{l,o}^2 \lambda_c}{\sigma}. \tag{2.4}$$

The capillary length l_c is defined by the Bond number of unity, $\text{Bo}_\lambda = 1$, when gravity and surface tension forces are in equilibrium

$$l_c = \left[\frac{\sigma}{g\left(\rho_l - \rho_g\right)}\right]^{1/2}. \tag{2.5}$$

For saturated water (one atm) it is $l_c = 2.5\,\text{mm}$. The K-H and R-T wavelengths are proportional to the capillary length.

Different pool-boiling critical heat flux (CHF) mechanisms are summarized in Section 1.2. The Helmholtz instability mechanism states that the generated bubbles create an unstable columnar vertical liquid-vapor interface and the CHF occurs when these columns impede the counterflow of make-up liquid, ceasing the liquid supply. Zuber [22] adopted this mechanism as a basis for his theory for a flat plate, assuming that vapor jets become unstable at the peak heat flux.

As shown in Figure 2.3, the vapor columns are arranged in a square array with side $\lambda_c = \lambda_{RT,d}$

11

from Eq. (2.2), corresponding to the most dangerous R-T waveforms, and column diameter $d_g = a\lambda_c$, where $a = 1/2$. The wavelength of the square arrangement proposed by Zuber was later corrected by [24]. The CHF is then calculated as the heat removed from this rising vapor columns

$$q_{CHF} = \rho_g v_{g,Z} \Delta h_{lg} \left(\frac{A_g}{A} \right)_Z, \tag{2.6}$$

and the vapor velocity is found from K-H wavelength

$$v_{g,Z} = \left(\frac{2\pi\sigma}{\lambda_{KH}\rho_g} \right)^{1/2}, \tag{2.7}$$

with the area ratio

$$\left(\frac{A_g}{A} \right)_Z = \frac{\pi a^2 \lambda_c^2}{4\lambda_c^2}. \tag{2.8}$$

Substituting this velocity and area ratio into Eq. (2.6) results in the pool-boiling CHF

$$q_{CHF} = \rho_g \Delta h_{lg} \left(\frac{2\pi^3 a^4 \sigma}{\lambda_{KH}\rho_g} \right)^{1/2}, \tag{2.9}$$

with $\lambda_{KH} = \lambda_{RT,d} = \pi d_g$. Substituting this into Eq. (2.6) we find the Zuber CHF

$$q_{CHF,Z} = \frac{\pi}{24} \rho_g \Delta h_{lg} \left[\frac{\sigma (\rho_l - \rho_g) g}{\rho_g^2} \right]^{1/4}. \tag{2.10}$$

The wavelength originally adopted by Zuber corresponds to a Bond number $\mathrm{Bo}_\lambda = 81$ and for saturated water at one atm, $q_{CHF,Z} = 1.1 \, \mathrm{MW/m^2}$. A slightly higher value of $q_{CHF,Z} = 1.25 \, \mathrm{MW/m^2}$ is encountered by using the wavelength discussed in [24].

The work from Liter et al. [53] expanded on this innate dependence on the characteristic wavelength by proposing and testing the use of a porous metasurface to modulate the critical wavelength. The rationale is that the introduction of a geometrically defined wavelength supersedes the dependence on R-T instabilities. The pool-boiling hydrodynamic CHF can be enhanced according
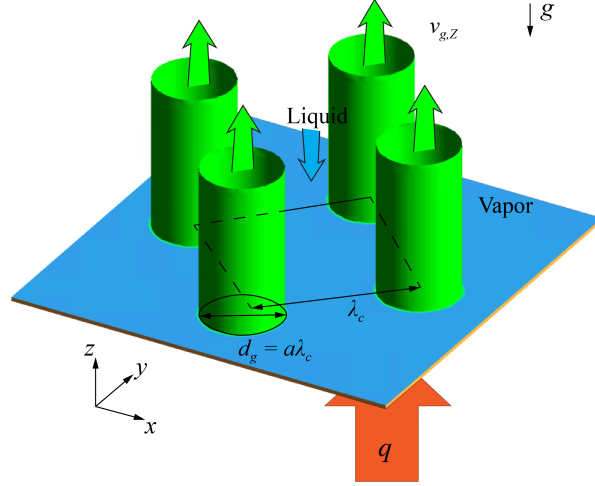
Figure 2.3: Spatial distribution of vapor columns, with counter flowing liquid, on a horizontal flat plate in the Zuber critical heat flux model. This is the Zuber unit cell.

to

$$q_{CHF,h} = \frac{\pi}{8} \Delta h_{lg} \left(\frac{\sigma \rho_g}{\lambda_c} \right)^{1/2},$$ (2.11)

where $\lambda_c \leq \lambda_{RT,d}$ is the modulated wavelength. The smaller wavelength corresponds to smaller vapor columns, allowing for a larger vapor velocity when the K-H instability is triggered.

The $q_{CHF,h}$ enhancement achieved by the wavelength modulation is similar to the pool-boiling heater-size effect. Measured $q_{CHF,h}$ over the $q_{CHF,Z}$ have been reported using progressively smaller heaters, and the smallest heater size is considered to be the capillary length l_c [23, 54].

2.2 Flow-Boiling CHF Theories

Differing from the pool boiling where the pressure gradient and the liquid momentum are in the gravity direction (z direction), the forced, axial inertial component of flow boiling breaks the symmetry of the counter, columnar two-phase flow of the Zuber unit cell shown in Figure 2.3. The smallest axial flow fundamentally alters the boundary conditions. Figure 2.4 illustrates this transition from pool to flow boiling, using the Zuber unit cell as the basis. The four relevant forces that can affect the two-phase interface are the gravitational force F_g, surface tension force F_σ, inertial

13

force F_u, and viscous force F_μ. Their expressions per unit area are as follows

$$\frac{F_g}{A} = g\left(\rho_l - \rho_g\right)\lambda_c, \quad \frac{F_\sigma}{A} = \frac{\sigma}{\lambda_c},$$
$$\frac{F_u}{A} = \rho_l u_{l,o}^2, \quad \frac{F_\mu}{A} = \frac{\mu u_{l,o}}{\lambda_c}, \tag{2.12}$$

they are also illustrated in Figure 2.4. The dimensionless numbers can be derived from different ratios of these forces, for instance the Weber and Froude numbers, given in Eq. (2.4), are defined as the ratio of surface tension and inertial forces, and gravitation and inertial forces, respectively. The Bond number is the ratio of gravity and surface tension forces, as shows Eq. (2.3). As mentioned earlier, the viscous forces are neglected in the linear stability analysis, but they are considered in the Reynolds number, the ratio of inertial and viscous forces

$$\mathrm{Re}_\lambda = \rho_l u_{l,o}^2 \frac{\lambda_c}{\mu u_{l,o}} = \frac{\rho_l u_{l,o} \lambda_c}{\mu}. \tag{2.13}$$

Traditionally, due to the innate complexities of the problem, authors have resorted to empirical correlations in the prediction of the flow-boiling CHF. Although the correlations can provide useful results, they cannot be used outside the limits of their experiments, so an investigation of the physical mechanisms responsible triggering the CHF is more desirable.

Determining the liquid supply mechanism in flow boiling is essential in defining the mechanisms responsible for the boiling crises. Four different mechanisms have been proposed and are widely accepted [47], namely, boundary-layer separation model [55], bubble-crowding model [56], sublayer dryout model [57], and interfacial lift-off model [58, 59]. Of those, only the boundary-layer separation model and the interfacial lift-off model were conceived for horizontal flow. In the boundary-layer separation dryout model [55], the flow-boiling crisis is treated as a purely hydrodynamic phenomenon, analogous to single-phase flow with gas injection at the permeable heated surface: the generated vapor decreases the liquid velocity gradient adjacent to the surface, what causes this gradient to gradually diminish and eventually the separation of the liquid layer and dryout. A general expression for the CHF is given in [60], where the CHF is related to the two-phase friction factor f_{lg} and a constant C dependant on the vapor quality and the degree of subcooling

$$q_{CHF,h} = \frac{C\rho_l u_l \Delta h_{lg}}{f_{lg}}.$$ (2.14)
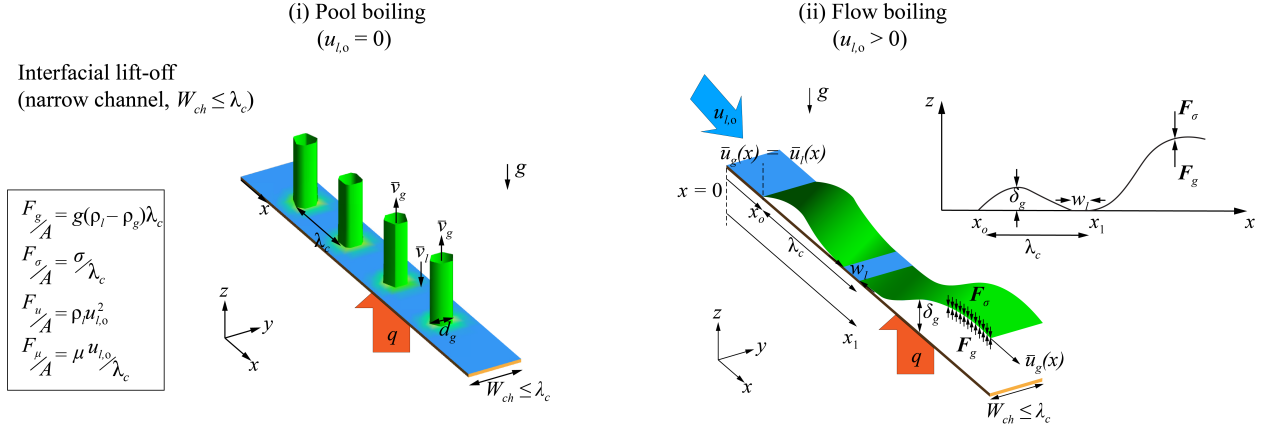
Figure 2.4: Schematic representation of the liquid- and vapor-phase flow distribution in the transition from (i) pool boiling to (ii) flow boiling for the 2-D interfacial lift-off model [58, 59] (narrow channel). The models are based on the Zuber unit cell, and the dominant forces governing the CHF are the buoyancy, surface tension, inertial, and viscous.

The interfacial lift-off model [58, 59] shown in Figure 2.4 postulates that CHF occurs when the momentum of the generated vapor produced in small portions of the surface called the wetting fronts, responsible for providing liquid to the heated surface, overcomes the interfacial pressure force, lifting the liquid away from the surface. The model states that the liquid supply mechanism occurs from the top at the wetting fronts, placed in the Zuber unit cell in a moving frame of reference [61].

In order to perform said balance, it employs three submodels. (i) A separated-flow model to resolve the flow velocities and thicknesses of liquid and vapor layers in the channel. (ii) A hydrodynamic stability model which employs the results from the previous model to predict the interfacial shape and the critical wavelength of the vapor layer. (iii) A CHF trigger mechanism model, determined considering both the critical wavelength of the vapor and the Helmholtz wavelength in the wetting front [61]. This is identical to the Zuber formulation, where the surface is modeled as square unit cells containing vapor jets surrounded by liquid, with the jet diameter half the critical vapor wavelength from the second submodel, $d_g = \lambda_c/2$. The implementation of this model for

15

saturated water (one $\mathtt{atm}$) is discussed in [62, 63].

The interfacial lift-off model is based on experimental measurements in a narrow channel ($W < \lambda_c$) with a single row of vapor jets. Figure 2.4 schematically illustrates the liquid and vapor flows in a narrow channel for pool and flow boiling conditions. The vapor expansion occupies the entire bottom portion of the channel, diverting the liquid upward and preventing the formation of a surface liquid track and axial liquid supply. Instead, liquid is supplied perpendicularly from the and limited to the wetting fronts. The critical vapor wavelength λ_c corresponds to the vapor momentum lifting the interface, interrupting the liquid supply.

The axial velocities u_f ($f = g$ or l for vapor and liquid) are found from the 2-D separated-flow submodel and employed in the following submodel (hydrodynamic stability theory) to determine the critical wavelength λ_c. The generated vapor ascending velocity and the liquid make-up velocity are found from the third submodel. Similar to Zuber CHF model, a second critical wavelength is found from the interaction between rising columnar vapor jets and descending liquid at the wetting fronts [61]. The effect of the axial flow on the wetting fronts mimics the behavior of a moving wall generating said columnar vapor jets – the same rationale present in Zuber analysis, but with a moving frame of reference.

Similar to the pool boiling $q_{CHF,h}$ of Eq. (2.11), the interfacial lift-off theory [58, 59, 61] of flow-boiling dryout results in an inverse dependency on the critical wavelength λ_c

$$q_{CHF,h} = \rho_g \Delta h_{lg} \frac{\pi}{8} \left(\frac{\sigma}{\lambda_c} \right)^{1/2} \left[\frac{\left(\frac{\rho_l + \rho_g}{\rho_l \rho_g} \right)^{1/2}}{1 + \frac{\rho_g}{\rho_l} \frac{\pi}{(16-\pi)}} \right], \qquad (2.15)$$

where λ_c is found from the 2-D separated flow model and interfacial instability submodels [61]

$$\lambda_c = 2\pi \left[\frac{\rho_l' \rho_g' (u_g - u_l)^2}{2\sigma \left(\rho_l' + \rho_g' \right)} + \left\{ \left[\frac{\rho_l' \rho_g' (u_g - u_l)^2}{2\sigma \left(\rho_l' + \rho_g' \right)} \right]^2 + \frac{(\rho_l - \rho_g) g \cos(\phi)}{\sigma} \right\}^{1/2} \right]^{-1}, \qquad (2.16)$$

where $\rho'_f = \rho_f \tanh^{-1}(\kappa H_f)$ is the modified phase density. The liquid and vapor phase velocities are calculated as

$$u_g = \frac{qx}{\rho_g \delta \left(c_{p,l} \Delta T_{sub} + \Delta h_{lg}\right)}, \tag{2.17}$$

$$u_l = \frac{u_{l,\mathrm{o}} H}{H - \delta} - \frac{qx}{\rho_l (H - \delta)(c_{p,l} \Delta T_{sub} + \Delta h_{lg})}, \tag{2.18}$$

where δ is the thickness of the vapor layer, from the separated flow model, and x is the axial location. The last term on the right of Eq. (2.15) is from the ascending vapor velocity and is related to the Helmholtz instability

$$v_{g,H} - v_{l,H} = \left(\frac{2\pi\sigma}{\lambda_H}\right)^{1/2} \left(\frac{\rho_l + \rho_g}{\rho_l \rho_g}\right)^{1/2}. \tag{2.19}$$

The continuity equation gives

$$v_{l,H} = \frac{\rho_g}{\rho_l} \left(\frac{\pi}{16 - \pi}\right) v_{g,H}. \tag{2.20}$$

The relationship between $q_{CHF,h}$ and the critical interfacial wavelength given in Eq. (2.15) for flow boiling in the interfacial lift-off model is functionally identical to Eq. (2.11), derived in [53] for pool boiling, discussed in Section 2.1. This wavelength modulation, achieved experimentally through porous metasurface with a periodic structural modulation of length λ_c supersedes the dependence only on the thermophysical properties given by the Rayleigh-Taylor wavelength, Eq. (2.3), allowing for CHF enhancement beyond the Zuber limit for plain surface [53].

The interfacial lift-off theory identifies a similar dependency of the $q_{CHF,h}$ on the interfacial wavelength, obtained from the stability analysis of the 2-D two-phase flow using the separated flow model. The forced flow $u_{l,\mathrm{o}}$ alters the characteristic wavelength λ_c, enhancing the $q_{CHF,h}$ similar to that achieved by λ_c modulation in pool boiling [53].

Both Eqs. (2.11) and (2.12) have an identical λ_c dependence as shown in Figure 2.5. In [53], a non-uniform porous coating was used with pentane as the fluid to modulate the λ_c and their experimental results (adjusted for saturated water properties at one atm) are shown in Figure 2.5, with good agreement to Eq. (2.11).
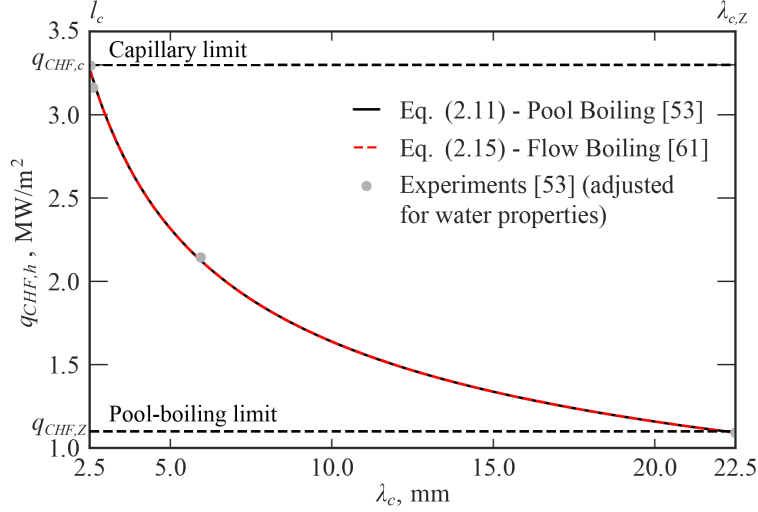
Figure 2.5: Wavelength modulation of pool and flow-boiling dryout heat flux based on the Zuber unit-cell model. The water-adjusted pool-boiling experimental results of [53] using a modulated porous coating are also shown.

While Figure 2.5 shows the flow boiling $q_{CHF,h}$ is equivalent to the surface wavelength modulation of pool boiling, we expect the anisotropic liquid inertia $u_{l,o}$ to affect the dryout crisis differently, and here we suggest a leading-edge surface liquid track instability guided by direct numerical simulation results, which are discussed in detail in Chapter 3. In Figure 2.6, this transition of the two-phase flow distribution from the pool (i) to flow boiling (ii), under a wide-channel ($W_{ch} > \lambda_c$) treatment is rendered and the fundamental forces are once again outlined. The Zuber vapor columns of pool boiling are deflected in the flow direction, while a surface liquid track is formed in the leading-edge region and meanders around the vapor columns. This surface liquid track provides the axial liquid supply to the heated surface. This contrasts with the liquid supply in the interfacial lift-off theory with the submodel based on a narrow channel, where the liquid supply is from the top at the wetting fronts, triggering a R-T instability.

The two-phase flow rendered in Figure 2.6 is hydrodynamically stable, stratified with the less dense phase on top, with the surface liquid track formed in the leading-edge region and beneath the vapor domain. As the vapor accelerates downstream, however, the interface relative velocity reaches a critical value, triggering the Kelvin-Helmholtz instability. This mechanism is dubbed the *leading-edge surface liquid track instability* and proposes the dryout is reached when the vapor

shear causes the surface liquid track to shear break with the K-H instability downstream. The wide-channel condition $W_{ch} > \lambda_c$ allows for the lateral periodic treatment and formation of the liquid track, fundamentally altering the dryout mechanism. This is guided by direct numerical simulation of flow boiling using the Zuber unit cell as the basis presented in Chapter 3, and existing experimental results.
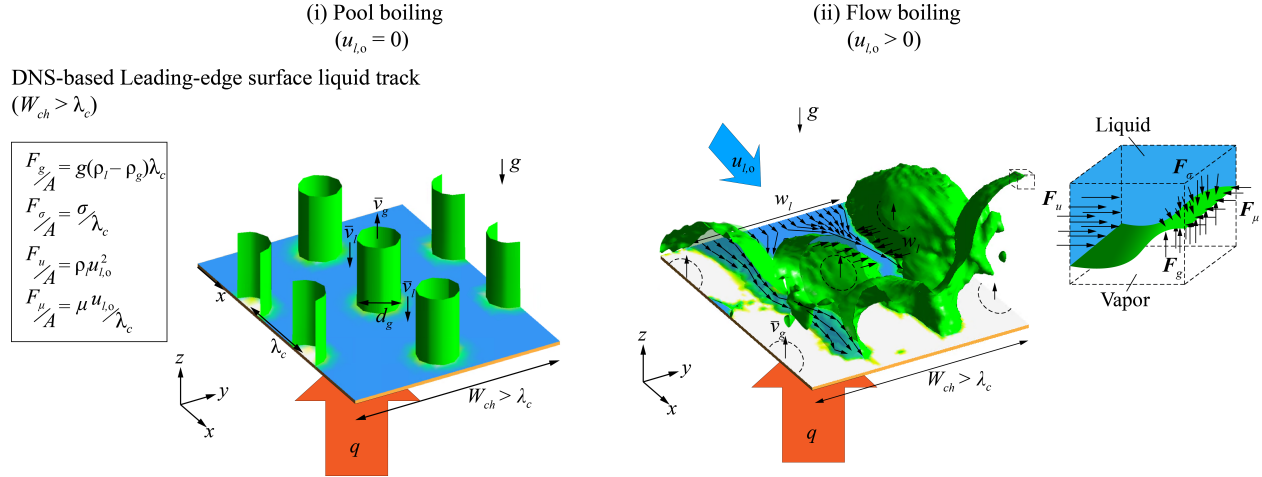
Figure 2.6: Schematic representation of the liquid- and vapor-phase flow distribution in the transition from (i) pool boiling to (ii) flow boiling for the 3-D DNS leading-edge surface liquid track model (wide channel). The models are based on the Zuber unit cell, and the dominant forces governing the CHF are the buoyancy, surface tension, inertial, and viscous.

2.3 Wavelength-Modulation Regime Based on Surface Liquid Track

As presented in Figure 2.5, the CHF enhancement achieved in flow boiling due to the forced axial flow component can also achieved through the usage of modulated capillary structures that separate the liquid and vapor flows, therefore we call the enhancement under this regime wavelength modulation regime (WMR) since the enhancement is entirely attributed to the liquid inertia ability to alter the natural wavelength scale.

This analysis assumes a fixed Zuber-type unit cell for the vapor inlets. This is a good assump-

Table 2.1: Physical properties of saturated water (one atm) [64].

ρ_l, kg/m^3	ρ_g, kg/m^3	μ_l, μPa s	μ_g, μPa s
958	0.58	279	12.3

T_{lg}, °C	Δh_{lg}, kJ/kg	σ, mN/m
100	2257	58.9

tion, as it provides a lower limit that is equal to the Zuber CHF at very low velocities, promoting a continuous transition from pool to flow boiling. Of course, the very concept of flow boiling breaks the radial symmetry assumed in the Zuber model and the ensuing phase distribution.

As discussed in Section 2.2, Eq. (2.16) from the interfacial lift-off model gives the dependency of the critical wavelength λ_c on the velocity of the liquid-phase u_l, given by Eq. (2.18). According to Eq. (2.16), buoyancy and surface tension forces are balanced to determine the critical wavelength. At high velocities, when the gravity force effect is negligible, i.e., $\frac{\rho_l' \rho_g' (u_g - u_l)^2}{2\sigma (\rho_l' + \rho_g')} >> \left[\frac{(\rho_l - \rho_g)g\cos(\phi)}{\sigma} \right]^{1/2}$, this becomes

$$\lambda_c = \frac{2\pi\sigma(\rho_l' + \rho_g')}{\rho_l' \rho_g' (u_g - u_l)^2} \approx \frac{2\pi\sigma}{\rho_g' (u_g - u_l)^2}, \tag{2.21}$$

suggesting a Weber number relationship, or dominance of the surface tension component. The value of threshold relative velocity for which Eq. (2.21) is valid for the saturated water (one atm) properties, given in Table 2.1, is $u_g - u_l \geq 6.37 \, \text{m/s}$.

In the interfacial lift-off submodel, the vapor momentum is determined by the balance between buoyancy and surface tension, Figure 2.4, i.e., the Weber number and Froude number squared (which is the Bond number). This treatment, similar to that used by Zuber for pool boiling, does not include the liquid inertia, which further prevents the vapor from displacing the liquid.

For flow boiling, the contribution of the forced axial flow cannot be neglected, as in Figure 2.6 the surface liquid supply depends on the axial flow. The forced liquid flow penetrates downstream and through the vapor columns, based on the modulated Zuber unit cell, ensuring the irrigation of the heated surface. This effect, however, is resisted by the viscous force. This modulation

is responsible for the $q_{CHF,h}$ enhancement over the $q_{CHF,Z}$ and is attributed to $u_{l,o}$, as shown in Figure 2.5.

The surface vapor columns disturb the surface liquid track and this disturbance depends on the inertia of the forced liquid flow and the inertia of the escaping vapor columns, adjacent to the surface. So, when including these inertiae, the effect of liquid viscosity, which are not included in the K-H and R-T stability analysis, needs to be considered in the surface liquid track fluid mechanics. As outlined in Figure 2.6, it is the continuous surface liquid track that irrigates the heated surface, and its interruption leads to the flow-boiling dryout.

The four fundamental forces at play must be considered. Since the Bond number accounts for the ratio of gravity and the surface tension forces, and the Reynolds number accounts for the ratio of inertial and the viscous forces, these two dimensionless groups are suited for this analysis. Both inertial and gravity forces contribute to the liquid supply by establishing the surface liquid track that is responsible for axial liquid supply, and for providing the liquid flow against the escaping vapor flow in the perpendicular make-up liquid supply. For this reason, these effects are combined by multiplying the Bond number and the Reynolds number of the liquid phase. This product is assumed to be a constant. This assumption is justified in Chapter 3 with the DNS results.

$$\frac{\text{We}_\lambda}{\text{Fr}_\lambda^2}\text{Re}_\lambda = \text{Bo}_\lambda\text{Re}_\lambda = \frac{g(\rho_l - \rho_g)\lambda_c^2}{\sigma}\frac{\rho_l u_{l,o}\lambda_c}{\mu_l} = C^2. \tag{2.22}$$

This relation between the critical wavelength and the inlet velocity is of the form $\lambda_c \approx u_{l,o}^{-1/3}$. From this relation, when the inertia is large, represented by a high inlet liquid velocity $u_{l,o}$, a smaller critical wavelength, and in turn a smaller Bond number is encountered, offsetting the high Reynolds number.

Rewriting Eq. (2.22) and replacing the wavelength from Eq. (2.11), we have

$$q_{CHF,h} = \frac{\pi}{8}\Delta h_{lg}(\sigma\rho_g)^{1/2}\left[\frac{g(\rho_l - \rho_g)\rho_l u_{l,o}}{C^2\sigma\mu_l}\right]^{1/6}. \tag{2.23}$$

Using the capillary length l_c, the dimensionless $q_{CHF,h}$ becomes

$$\frac{q_{CHF,h}}{\rho_g^{1/6}\Delta h_{lg}[\sigma g(\rho_l - \rho_g)]^{1/4}} = \frac{\pi}{8C^{1/3}}\mathrm{Re}_\lambda^{1/6}. \tag{2.24}$$

This is comparable to the dimensionless Zuber CHF, Eq. (2.9), i.e.,

$$\frac{\pi}{8C^{1/3}}\frac{u_{l,o,min}^{1/6}}{\nu_l^{1/6}}\left[\frac{\sigma}{g(\rho_l - \rho_g)}\right]^{1/12} = \frac{\frac{\pi}{24}\rho_g\Delta h_{lg}\left[\frac{\sigma(\rho_l - \rho_g)g}{\rho_g^2}\right]^{1/4}}{\rho_g^{1/6}\Delta h_{lg}[\sigma g(\rho_l - \rho_g)]^{1/4}}. \tag{2.25}$$

Solving for the liquid inlet velocity, the minimum $u_{l,o}$ giving to $q_{CHF,Z}$, we find $u_{l,o,min} = C^2\frac{\nu_l}{729 l_c}$. Similarly, comparing Eq. (2.24) to the CHF for flow boiling given by Eq. (2.11), for $\lambda_c = l_c$, i.e., $q_{CHF,c}$ we have

$$\frac{\pi}{8C^{1/3}}\frac{u_{l,o,max}^{1/6}}{\nu_l^{1/6}}\left[\frac{\sigma}{g(\rho_l - \rho_g)}\right]^{1/12} = \frac{\frac{\pi}{8}\Delta h_{lg}(\sigma\rho_g)^{1/2}\left[\frac{g(\rho_l - \rho_g)}{\sigma}\right]^{1/12}}{\rho_g^{1/6}\Delta h_{lg}[\sigma g(\rho_l - \rho_g)]^{1/4}}. \tag{2.26}$$

solving once again for liquid the inlet velocity, now the maximum $u_{l,o}$ corresponding to $q_{CHF,c}$ is $u_{l,o,max} = C^2\frac{\nu_l}{l_c}$. The verification of the proposed functional relationship for the wavelength-modulation regime requires CFD simulations to match the hydrodynamic CHF to the inlet velocity. The value for the C constant and the solution to Eqs. (2.25) and (2.26) will also be determined.

Figure 2.7 shows the variations of the $q_{CHF,h}$ and the critical wavelength with respect to the inlet velocity for the interfacial lift-off theory, Eqs. (2.12) and (2.13), and the surface liquid-track dryout models, Eqs. (2.22) and (2.23), for saturated water (one atm) with properties listed in Table 2.1. The dashed lines mark the minimum velocity limit, when the critical wavelength is the Zuber wavelength $\lambda_{c,Z}$ and corresponding to the $q_{CHF,Z}$, and the maximum velocity limit, when the critical wavelength is the capillary length l_c and corresponding to the $q_{CHF,c}$. These two velocities, $u_{l,o,min}$ and $u_{l,o,max}$, mark the wavelength-modulation regime.
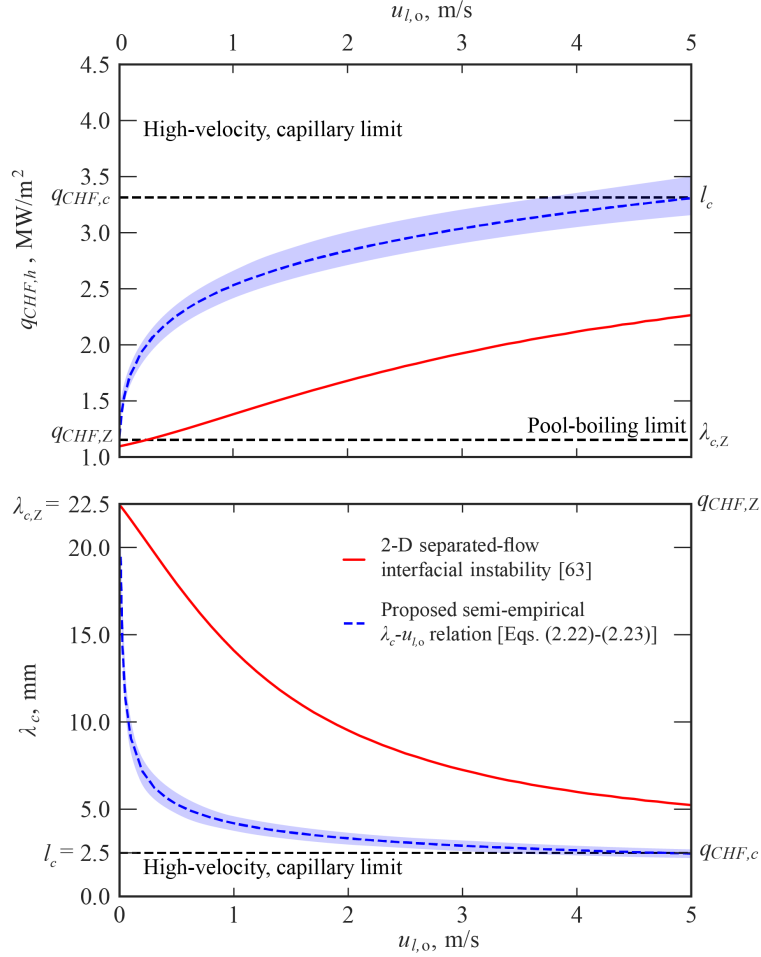
Figure 2.7: Variations of (a) hydrodynamic CHF and (b) characteristic wavelength with inlet velocity for saturated water (one atm) in the wavelength-modulation regime. Relations from the interfacial lift-off and leading-edge surface liquid track models are shown.

2.4 Summary

The flow-boiling crisis theory was presented as an extension of the pool-boiling Zuber analysis. The roles of the four fundamental forces were explained and a novel flow-boiling CHF trigger mechanism was proposed based on first principles. The key assumption of the product of the Bond (ratio of gravity and surface tension forces) and Reynolds (ratio of inertial and viscous forces) numbers being constant given in Eq. (2.22) will be expanded in Chapter 3.

CHAPTER 3

Direct Numerical Simulation of Flow Boiling Crisis based on Zuber Unit Cell: Verification of Wavelength Modulation Regime

In this chapter, the direct numerical simulation (DNS) of the flow-boiling crisis is performed in order to verify the surface-liquid track dryout CHF trigger mechanism proposed in Section 2.3 within the so-called Wavelength Modulation Regime [53, 61], where the vapor-flow shear destabilizes the leading-edge surface liquid track, causing its dryout. Here, DNS refers to the flow boiling and not what is conventionally used in the single-phase turbulent flow simulations where no modeling is used and the entire turbulence spectrum is resolved.

As shown in Figure 2.5, the wavelength modulation by inlet velocity in flow boiling and by porous metasurface in pool boiling are identical, so the critical wavelength λ_c for a given flow-boiling CHF $q_{CHF,h}$ can be found from Eq. (2.11). An inlet velocity is selected and the simulation is run until a steady-state, leading-edge surface-liquid track is reached. This velocity is reduced until dryout is observed. At this point, the prescribed velocity is determined to be corresponding to the modulated wavelength λ_c and CHF $q_{CHF,h}$.

The CFD domain is illustrated in Figure 3.1. The inlet liquid velocity $u_{l,o}$ is prescribed upstream and on the heated metasurface ($z = 0$) the vapor and liquid velocities are prescribed for a given heat flux. The lateral (x-z plane) periodicity is used, with shear-free top surface ($z = H_{ch}$) and continuous flow condition at the outlet downstream. Saturated water (one atm) is assumed. The
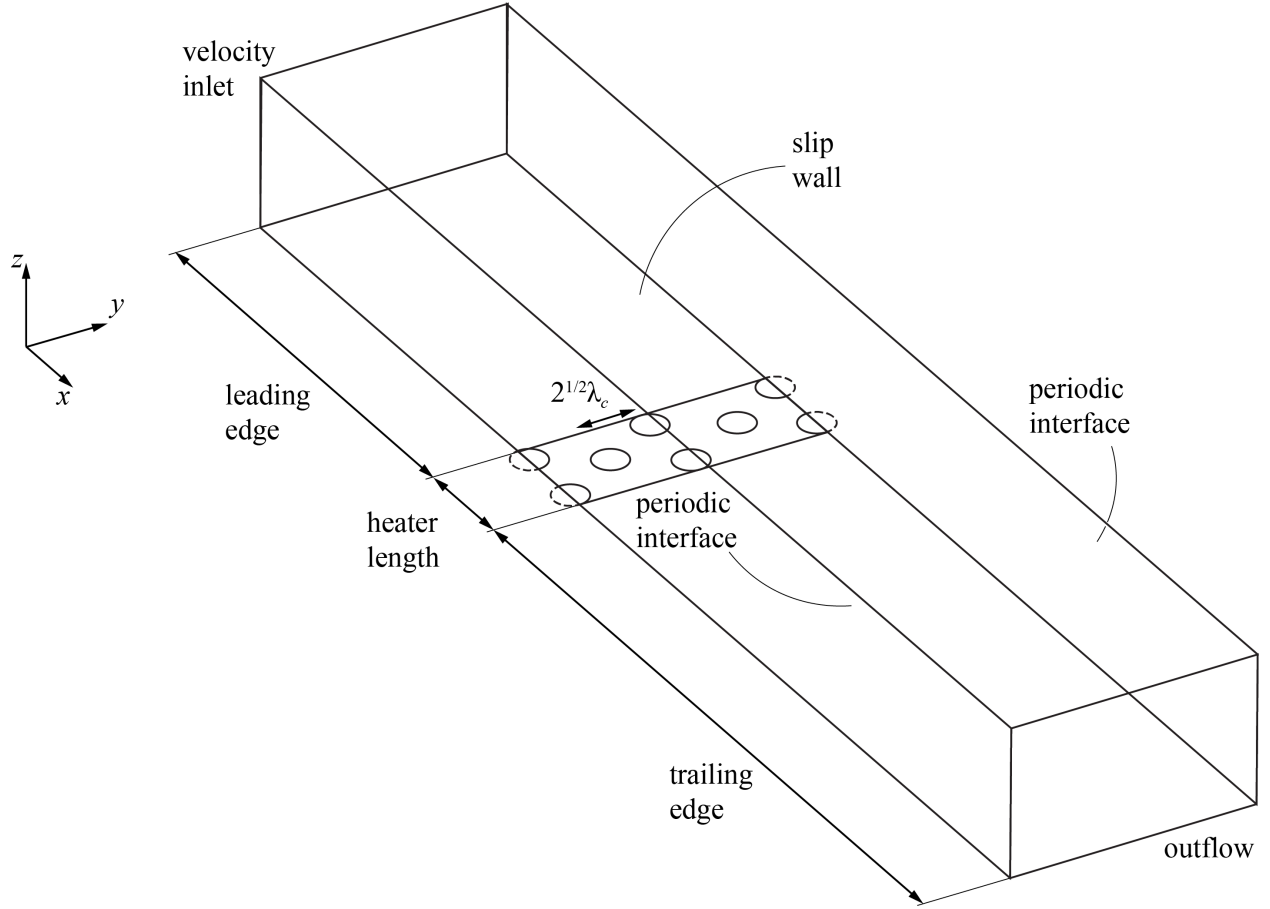
Figure 3.1: Adopted CFD domain showing the different boundary conditions.

related two-phase fluid mechanics (transient, 3-D Navier-Stokes equations) are solved numerically using the code ANSYS Fluent [65]. The treatment of turbulence is with the Large Eddy Simulations, discussed in detail in Section 3.3. As mentioned earlier, the unit-cell geometric parameters are related to heat flux according to Eq. (2.11), which has been used for the pool boiling, however, the forced liquid flow $u_{l,o}$ can also modulate the critical wavelength. The computational domain contains two axial and two lateral unit cells, with lateral periodicity. A leading and a trailing-edge region are added for more realistic upstream and downstream flow conditions. The vapor-column velocity and the countering liquid flow are related to heat flux through

$$v_{g,o} = \frac{qA}{\rho_g \Delta h_{lg} A_g}, \ v_{l,o} = \frac{qA}{\rho_g \Delta h_{lg} (A - A_g)}, \tag{3.1}$$

25

where A is the unit-cell heated surface area and A_g the vapor column area. As an example, for saturated water at one atm (properties in Table 2.1) and $q = 1.75\,\text{MW/m}^2$, give $v_{g,\text{o}} = 8.84\,\text{m/s}$ and $v_{l,\text{o}} = 0.95\,\text{mm/s}$. As expected, the vapor velocity is about four orders-of-magnitude larger than the liquid.

An important distinction is that, in the channel, it is assumed that the two-phase flow is under saturated liquid-vapor condition (no evaporation or condensation), and the predicted results are compared with the saturated water boiling experiments. No phase change is included in the two-phase flow simulations, therefore the empirical models for evaporation and condensation are not used. Again, for the case of the plain surface, the evaporation and the return of liquid to the surface are based on the Zuber unit cell model/theory as surface boundary conditions under saturated liquid-vapor condition.

3.1   Dimensionless numbers

The liquid and vapor inertial forces are scaled with their respective viscosities in the Reynolds number for the liquid, given in Eq. (2.13), and vapor phases. As mentioned earlier, the role of the liquid-vapor interfacial tension is presented by the Weber number using the liquid inertia. For the role of gravity (buoyancy), the Froude number using the liquid inertia is used in Eq. (2.4). The compressibility limit of the vapor is addressed with the Mach number using the vapor speed of sound u_a (for Mach number smaller than 0.3, the compressibility effects are neglected). The Zuber unit-cell size presented by wavelength λ_c is used for the length scale. In addition to Eqs. (2.4) and (2.13), the vapor Reynolds number and Mach number [66] are defined as

$$\text{Re}_g = \frac{\rho_g v_{g,o} \lambda_c}{\mu_g}, \ \text{Ma}_{g,per} = \frac{v_{g,per}}{u_a}. \tag{3.2}$$

The range of these dimensionless numbers are summarized in Table 3.1 for the range of liquid velocity $u_{l,\text{o}}$, critical heat flux, and the Zuber unit-cell characteristic wavelength λ_c.

For the high velocity regime, using the values from Table 3.1, the constant C from Eq. (2.22)

Table 3.1: CFD condition and dimensionless numbers for different velocity regimes in the wavelength modulation regime.

Velocity regime	q, MW/m^2	$u_{l,o}$, m/s	λ_c, mm
Low	1.35	0.05–0.25	17.7
Moderate	1.75	0.25–1	9.4
High	3	1–3	2.98

Velocity regime	Re_l	Re_g	Ma_g
Low	3×10^3–15×10^3	5.7×10^3	0.015
Moderate	7.9×10^3–32×10^3	3.9×10^3	0.02
High	10×10^3–30×10^3	2.1×10^3	0.03

Velocity regime	Fr_λ	We_λ	Bo_λ
Low	0.1–0.6	0.7–18	50
Moderate	0.8–3.3	9.6–153	14
High	5.8–17.5	49439	1.4

is found to be $C \approx 200$. With this value, the limits of the wavelength modulation regime can be calculated: the minimum velocity is $u_{l,o,min} = C^2 \frac{\nu_l}{729 l_c} = 6 \, \mathrm{mm/s}$ and the maximum velocity is $u_{l,o,max} = C^2 \frac{\nu_l}{l_c} = 5 \, \mathrm{m/s}$.

3.2 Treatment of Liquid-Vapor Interface: Volume of Fluid (VOF) Method

In the finite-volume method, the domain is discretized in the form of small volumes for which the conservation laws are solved [67]. The relevant physical quantities such as temperature, velocity, and pressure are stored in the nodes located at the center of each volume. In two-phase flow modeling, correctly identifying the region of the domain occupied by each phase and accurately capturing the interface is a key requirement. Interface tracking methods introduce an additional variable that differentiates between the phases and is advected by the flow through the general equation

$$\frac{\partial}{\partial t}(f) + \nabla \cdot (f \tilde{\mathbf{u}}_g) = 0. \tag{3.3}$$

where f is the variable containing information about the phase. In the level-set method [68], the interface is defined as the zero level set of a distance function $f = \varphi(x, t)$ from that interface. It can be expressed as

$$\varphi(x,t) = \begin{cases} d, & \text{primary phase} \\ 0, & \text{interface} \\ -d, & \text{secondary phase} \end{cases} . \tag{3.4}$$

where d is the distance from the interface. The level-set equation is then

$$\frac{\partial}{\partial t}(\varphi) + \nabla \cdot (\varphi \tilde{\mathbf{u}}_g) = 0. \tag{3.5}$$

Another widely employed method is the volume of fluid (VOF) method [69], which tracks the fraction α_i occupied by the primary phase in the finite volume, attributing a value of $\alpha_i = 1$ when the volume is completely filled by the primary phase, $\alpha_i = 0$ when it is completely absent, and the corresponding volume fraction $\alpha_i = V_i/V$ when both the primary and secondary phases are present. It can be expressed as

$$\alpha_i(x,t) = \begin{cases} 1, & \text{primary phase} \\ V_i/V, & \text{interface} \\ 0, & \text{secondary phase} \end{cases} , \tag{3.6}$$

an additional constraint is imposed to ensure conservation

$$\sum_{i=1}^{n} \alpha_i = 1, \tag{3.7}$$

where $i = l, g$ is an index representing the phase.

Due to its mass conservation characteristics, the VOF method is preferred over the level-set method, although authors have employed a combination of both [70]. In the VOF treatment for

two-phase flow, single continuity and momentum conservation equations are used with an additional equation for the phase identifier α

$$\frac{\partial}{\partial t}(\alpha\rho_g) + \nabla \cdot (\alpha\rho_g\tilde{\mathbf{u}}_g) = 0. \tag{3.8}$$

The phasic physical properties are interpolated according to the volume fraction, for example the fluid density and viscosity are calculated as follows

$$\rho_f = \alpha\rho_g + (1-\alpha)\rho_l, \tag{3.9}$$

$$\mu_f = \alpha\mu_g + (1-\alpha)\mu_l. \tag{3.10}$$

Near the interface, special interpolation functions are used to improve the accuracy of the captured interface. The geometric reconstruction scheme uses a piecewise-linear approach (piecewise-linear interface calculation, PLIC) [71, 72], assuming a linear slope for the interface between the two phases.

3.3 Large Eddy Simulation (LES)

For a more accurate calculation of the two-phase flow turbulence, especially the flow adjacent to the heated metasurface and the state of the surface liquid track, the CFD simulations were conducted using the LES [73]. In the LES, the large turbulent eddies are resolved directly, while the small (i.e., subgrid) eddies are modeled. The momentum and mass are transported mostly by the large eddies which are significantly affected by the geometry and boundary conditions, while the small eddies tend to be more isotropic, and the conventional turbulent models are more suited for their prediction.

A filter is applied to the Navier-Stokes equations, effectively cutting off eddies smaller than the grid size

$$\tilde{\phi}(\mathbf{x}) = \int_{\Delta V} \phi(\mathbf{x}')G(\mathbf{x}, \mathbf{x}')d\mathbf{x}', \tag{3.11}$$

where ΔV is the fluid domain and G the filter function that determines the scale of the resolved eddies. In ANSYS Fluent [65], the finite-volume discretization provides the filtering operation for the LES as

$$\tilde{\phi}(\mathbf{x}) = \frac{1}{v} \int_V \phi(\mathbf{x}')G(\mathbf{x}, \mathbf{x}')d\mathbf{x}', \tag{3.12}$$

where V is the computational cell volume. The filter function is then

$$G(\mathbf{x}, \mathbf{x}') = \begin{cases} \frac{1}{V}, \mathbf{x}' \in v \\ 0, \text{otherwise} \end{cases}. \tag{3.13}$$

These filtered Navier-Stokes equations are

$$\frac{\partial \rho_f}{\partial t} + \frac{\partial}{\partial x_i}(\rho_f \tilde{u}_{f,i}) = 0, \tag{3.14}$$

$$\frac{\partial}{\partial t}(\rho_f \tilde{u}_{f,i}) + \frac{\partial}{\partial x_j}(\rho_f \tilde{u}_{f,i}\tilde{u}_{f,j}) = \frac{\partial \sigma_{ij}}{\partial x_j} - \frac{\partial \tilde{p}}{\partial x_j} - \frac{\partial \tau_{ij}}{\partial x_j}, \tag{3.15}$$

where σ_{ij} is the viscosity stress tensor component and τ_{ij} is the subgrid-scale stress component. The viscosity stress and the subgrid-scale stress tensors are given as

$$\sigma_{ij} = \left[\mu_f \left(\frac{\partial \tilde{u}_{f,i}}{\partial x_j} + \frac{\partial \tilde{u}_{f,j}}{\partial x_i} \right) \right] - \frac{2}{3}\mu_f \frac{\partial \tilde{u}_{f,l}}{\partial x_l}\delta_{ij}, \tag{3.16}$$

$$\tau_{ij} = \rho_f \overline{u_{f,i}u_{f,j}} - \rho_f \bar{u}_{f,i}\bar{u}_{f,j}. \tag{3.17}$$

The subgrid-scale resulting from the filtering operation requires modeling. As in Reynolds-averaged Navier-Stokes (RANS) equations, the Boussinesq hypothesis is employed [74]

$$\tau_{ij} - \frac{1}{3}\tau_{kk}\delta_{ij} = -2\mu_{f,t}\bar{S}_{ij}. \tag{3.18}$$

To generate a time-independent inlet condition, a random 2-D vortex is considered. With this approach, a perturbation is added on a specified mean velocity profile via a fluctuating vorticity field (i.e., two-dimensional in the plane normal to the streamwise direction).

The strain tensor is defined as

$$\bar{S}_{ij} = \frac{1}{2} \left(\frac{\partial \bar{u}_{f,i}}{\partial x_j} + \frac{\partial \bar{u}_{f,j}}{\partial x_i} \right). \tag{3.19}$$

In the Wall-Adapting Local Eddy-Viscosity (WALE) [75] the eddy viscosity is modeled by

$$\mu_{f,t} = \rho_f L_s^2 \frac{\left(S_{ij}^d S_{ij}^d \right)^{3/2}}{\left(S_{ij} S_{ij} \right)^{5/2} + \left(S_{ij}^d S_{ij}^d \right)^{5/4}}, \tag{3.20}$$

where L_s is the mixing length for the subgrid scale

$$L_s = \min \left(\kappa_{\mathrm{vK}} \Delta z, C_w V^{1/3} \right), \tag{3.21}$$

where κ_{vK} is the von Karman constant, $C_w = 0.325$, $V^{1/3}$ is the local grid scale and

$$S_{ij}^d = \frac{1}{2} \left[\left(\frac{\partial \bar{u}_{f,i}}{\partial x_j} \right)^2 + \left(\frac{\partial \bar{u}_{f,j}}{\partial x_i} \right)^2 \right] - \frac{1}{3} \delta_{ij} \left(\frac{\partial \bar{u}_{f,k}}{\partial x_k} \right)^2. \tag{3.22}$$

The interfacial force term in the momentum conservation equation is given by the continuum surface force (CSF) model as

$$\mathbf{f}_s = \sigma \frac{\rho_f \kappa_g \nabla \alpha}{\frac{1}{2} \left(\rho_l + \rho_g \right)}, \tag{3.23}$$

where $\kappa_g = \nabla \cdot \left(\frac{\nabla \alpha}{\alpha} \right)$ is the interface normal defined as the gradient of the volume fraction.

In order to compute turbulent quantities, a decomposition is required and the velocity resolved by the grid can be decomposed into mean and fluctuation quantities [74]

$$\bar{u}_f = \tilde{u}_f - u_f', \tag{3.24}$$

where $\tilde{u}_f$ is the filtered velocity field, $\bar{u}_f$ is the mean velocity field averaged over a period of time Δt and u'_f is the fluctuation velocity field. The turbulence kinetic energy resolved by the grid is calculated as

$$\bar{E}_{f,t} = \frac{1}{2}\left(\bar{u}_f'^2 + \bar{v}_f'^2 + \bar{w}_f'^2\right). \tag{3.25}$$

The unresolved portion of the turbulent kinetic energy is the subgrid component, in the WALE model [75], this portion of the turbulent kinetic energy is calculated as

$$\bar{E}_{f,t,sgs} = \left(\frac{\mu_{f,t}}{C_w \rho_f L_s}\right)^2. \tag{3.26}$$

The total kinetic energy is, then

$$\bar{E}_{f,t,total} = \bar{E}_{f,t} + \bar{E}_{f,t,sgs}. \tag{3.27}$$

When $\frac{\bar{E}_{f,t}}{\bar{E}_{f,t,total}} \geq 0.8$, the mesh is well suited for the problem. For Figure 3.2 and similar results, the ratio is 0.96.

Figure 3.2 shows the dimensionless turbulence spectra for $q = 1.75\,\mathrm{MW/m^2}$ on plain surface. The Kolmogorov $-5/3$ power is shown as a blue dashed line in the inertial subrange. The subgrid turbulence kinetic energy decay is highlighted in gray. In the subgrid modeling range, for wavenumbers larger than the filter length, i.e., in the dissipation subrange, the spectrum follows the -3 power of the dissipation scale observed experimentally for bubbly flows [76, 77]. This is reasonable since the overall observation is that turbulence originates from eddies formed at the liquid-vapor interface and the smallest eddies would be encountered in the small vapor inclusions that detach from the escaping vapor stream. The highest wavenumber which can be resolved by the simulation corresponds to twice the grid size and is denoted as

$$\kappa_{f,\Delta x} = \frac{2\pi}{2L_s}. \tag{3.28}$$
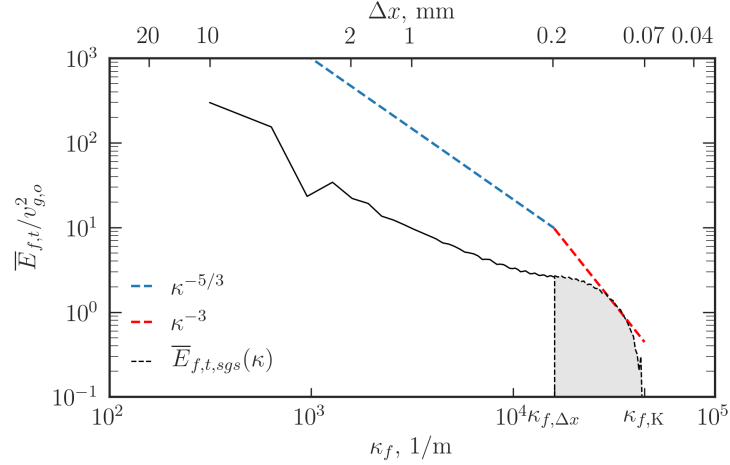
Figure 3.2: Turbulence kinetic energy spectra in the axial midplane for (a) plain surface $q = 1.75\,\mathrm{MW/m^2}$ and $u_{l,\mathrm{o}} = 0.5\,\mathrm{m/s}$. The Kolmogorov inertial subrange $-5/3$ [74] and the empirical dissipation range -3 [76, 77] scales are shown. The subgrid turbulence kinetic energy is highlighted in gray shade.

The maximum wavenumber is related to the Kolmogorov length scale, given as [74]

$$\lambda_{f,K} = \left(\frac{\nu_g^3}{\varepsilon_{f,t}}\right)^{1/4}. \tag{3.29}$$

These are also marked in Figure 3.2. These and the power-law comparisons in Figure 3.2 support that the numerically predicted turbulent quantities have the expected theoretical behavior.

A similar trend is encountered with the components of the Reynolds stress tensor, as shows Figure 3.3. Results were averaged over a similar time frame. Turbulence intensity is expected to be more pronounced near the channel walls and the liquid-vapor interface. Figure 3.3 shows that the most intense stresses occur in the vapor phase, indicating the production of turbulence is more pronounced in the gas phase due to the large inertial force and interfacial shearing.

Alongside the void-fraction, the Q-criterion, a vortex identification method, also shows that vortices are limited to the vapor phase. The vorticity is

$$\omega = \nabla \times \mathbf{u}_f, \tag{3.30}$$
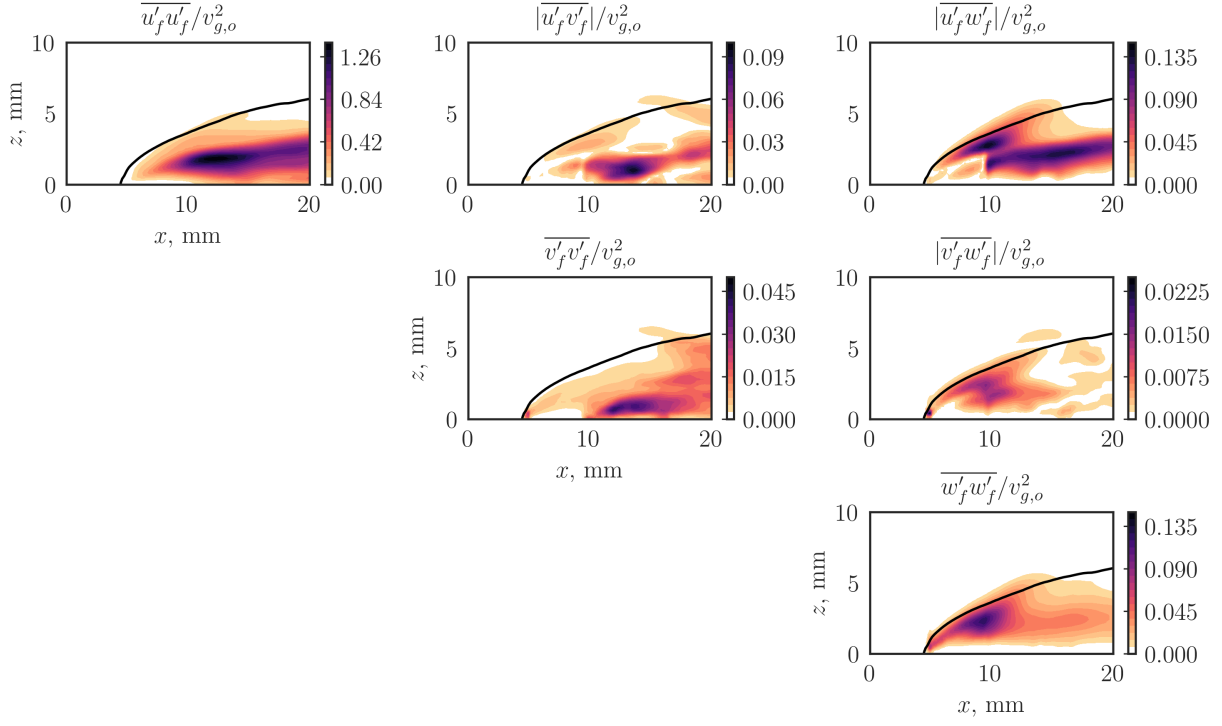
Figure 3.3: The distributions of the Reynolds stress tensor components in the axial midplane for $q = 1.75 \, \mathrm{MW/m^2}$ and $u_{l,o} = 0.5 \, \mathrm{m/s}$ for saturated water (1 atm). The interface is shown with the curved solid line.

and its presentation requires the velocity gradient tensor invariants, P, Q, and R. These invariants are the coefficients of the cubic characteristic polynomial $\det(\nabla \mathbf{u}_f - \lambda \mathbf{I})$, i.e.,

$$\lambda^3 + P\lambda^2 + Q\lambda + R = 0, \tag{3.31}$$

where $P = -S_{ii}$, $Q = \frac{P^2 - S_{ij}S_{ji} + \Omega_{ij}\Omega_{ji}}{2}$, and $R = \frac{-P^3 + 3PQ - S_{ij}S_{jk}S_{ki} - 3\Omega_{ij}\Omega_{jk}\Omega_{ki}}{2}$. For incompressible flows, the first invariant is $P = 0$ (since $\nabla \cdot \mathbf{u}_f = 0$), so the so-called Q-criterion is derived based on the second invariant [78], and is

$$Q = \frac{1}{2} \left(\|\mathbf{\Omega}\|^2 - \|\mathbf{S}\|^2 \right), \tag{3.32}$$

where $\mathbf{S}$ is the symmetric part of the strain rate tensor and $\mathbf{\Omega}$ is its antisymmetric part (vorticity tensor). The Q-criterion states that $Q > 0$ represents a vortex. There are other methods for vortex

identification available [79], however in this work, Eq. (3.32) is used.

(a)

(c)

(b)

(d)
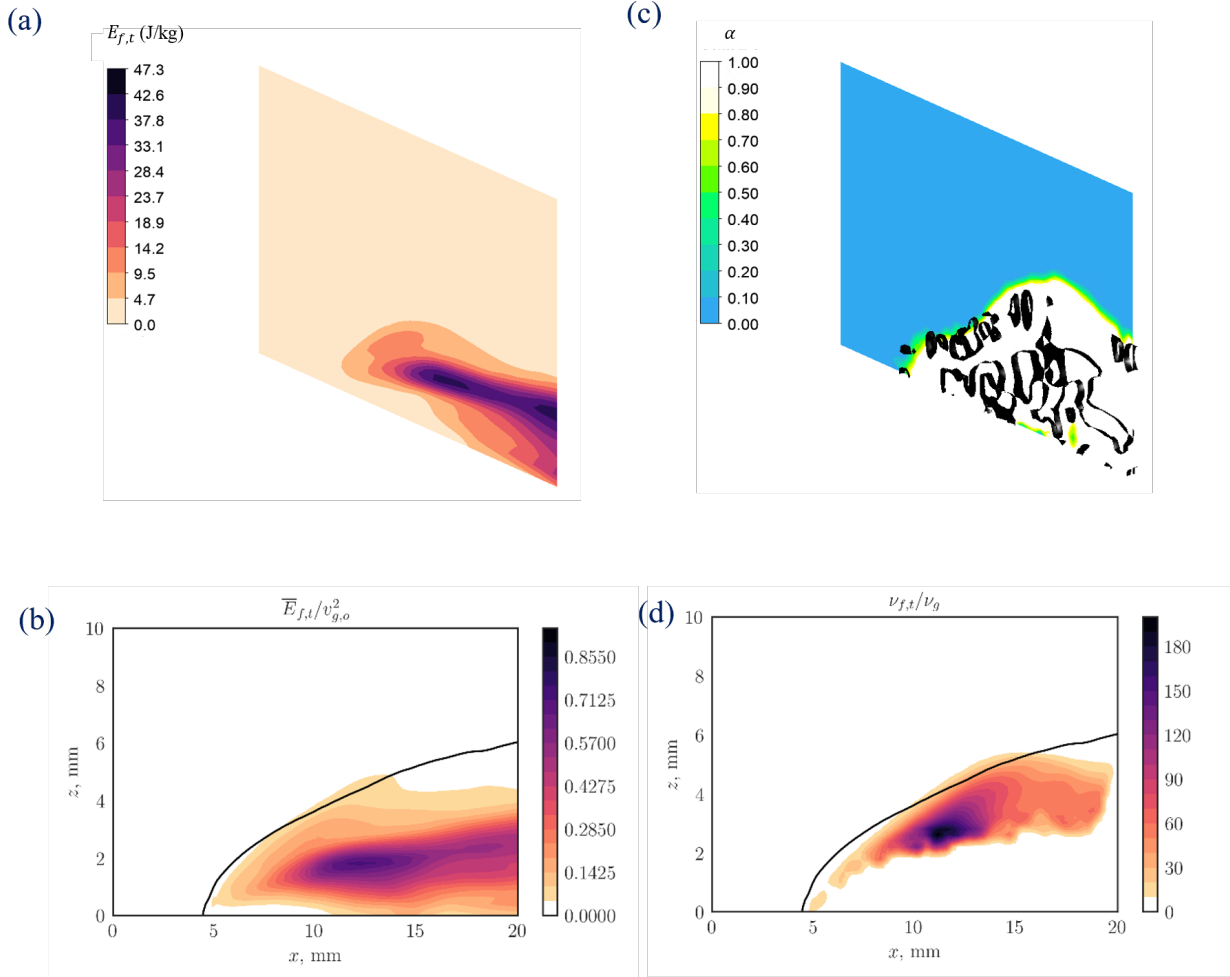
Figure 3.4: (a) Predicted distribution of the instantaneous, constant interfacial shear-flow turbulent kinetic energy $\bar{E}_{f,t}$ contours in the axial midplane for plain surface for $q = 1.75\,\mathrm{MW/m^2}$, $u_{l,o} = 0.5\,\mathrm{m/s}$. (b) Contour of constant time-averaged turbulence kinetic energy $\bar{E}_{f,t}$. Instantaneous contours of constant (c) invariant $Q = 1\,1/\mathrm{s^2}$, and (d) eddy viscosity $\mu_{f,t}$. The results are for saturated water at one atm, and $y = 0$.

Figures 3.4(a) to (d) show the distributions in the axial midplane ($y = 0$) of the turbulence quantities for $q = 1.75\,\mathrm{MW/m^2}$ and $u_{l,o} = 0.5\,\mathrm{m/s}$. The black line denotes the liquid-vapor interface. Figures 3.4(a) and (b) show that the turbulence is generated at the liquid-vapor interface and it is noticeably more intense in the vapor phase, this is in agreement with recent studies of two-phase LES that show the occurrence of interface-generated turbulent eddies [76, 80, 81]. The peak in the turbulent kinetic energy $\bar{E}_{f,t}$ is in the vapor phase in the leading-edge region, where

the incoming liquid flow is severely deflected and broken by the vapor columns. In this region, the vapor inertia overcomes the surface tension to enter the liquid channel flow. Near the liquid inlet, the relative liquid-vapor velocity is the largest, because the liquid has not yet accelerated and the vapor velocity has not changed from its large magnitude prescribed by the heat flux boundary condition, four-order-of magnitude larger than the liquid.

Figure 3.4(c) shows isosurface of the Q-criterion for $Q = 1\,1/\text{s}^2$ superposed on the void fraction distribution in the axial midplane. All the vortical structures identified by the Q-criterion remain within the vapor phase. Vortical structures dissipate turbulent kinetic energy [76]. Similarly, the eddy viscosity distribution is shown in Figure 3.4(d). It is calculated using Eq. (3.18), is proportional to the Reynolds stresses normalized by the mean strain rate. Its peak is observed just beneath the interface and is compatible with the distribution of the vortices (and the large gradient components) occurring mainly within the vapor phase. These analyses of the turbulent quantities were repeated for all CFD runs with similar trends found regarding the turbulent vortical structure and distribution.

3.4   Dryout Limit from the DNS

The direct simulations are used to verify the CHF wavelength-modulation regime for the plain surface, while varying the liquid velocity $u_{l,\text{o}}$. We begin by choosing a CHF and finding λ_c according to Eq. (2.11). Several iterations are required to determine the relation between $u_{l,\text{o}}$ and $q_{CHF,h}$. In these iterations, either $u_{l,\text{o}}$ is varied while q is kept constant or vice-versa (and consequentially unit-cell is changed). The outcome is the $u_{l,\text{o}}$ corresponding to $q_{CHF,h}$ calculated using Eq. (2.11), which depends on the thermophysical properties and the Zuber unit cell, presented by the wavelength λ_c. So, the inlet velocity affects the λ_c, thus altering $q_{CHF,h}$.

So, for a given q, the λ_c is determined from Eq. (2.11) and for a plain surface geometry, simulations are conducted with this wavelength and progressively smaller $u_{l,\text{o}}$ to find the $u_{l,\text{o}}$ corresponding to the identified surface dryout (within the sensitivity of the practical $u_{l,\text{o}}$ or q steps in the

simulation).

To determine dryout, the width of liquid track $\langle w_l \rangle$ in the simulated unit-cell based domain of the heated surface is used. Instantaneous as well as running-time average values are used. The phase distribution in the x-y plane at elevation $z = 0.25\,\mathrm{mm}$ is used to detect the liquid phase and a phase marker is used to measure this width. The liquid-phase volume with $\alpha < 0.5$ has a marker value of 1, while the vapor-phase is marked with a value of 0. The liquid track width is determined as the summation of the marked pixels, and presence of vapor reduces $\langle w_l \rangle$. The summation is done over a rectangular domain $(\Delta x \Delta y)$ and is then normalized by the integral length of the liquid track which is $\Delta y = \lambda_c(3^{1/2} - 1/2)$ $(\Delta x = \Delta y/10)$, as shown in Figure 3.5(a), i.e.,

$$\langle w_l^* \rangle = \frac{1}{\Delta x} \sum_i^{\Delta x} \left(\frac{1}{\lambda_c(3^{1/2} - 1/2)} \sum_i^{\Delta y} f \right), \quad \begin{cases} f = 0, & \alpha \geq 0.5 \\ f = 1, & \alpha < 0.5 \end{cases}. \tag{3.33}$$

Figure 3.5(b) to (d) show the time variations of the instantaneous and running-time averaged dimensionless liquid track width. In order to account for the different velocities and wavelengths, a dimensionless time, normalized by the fluid transit time is used, i.e.,

$$t^* = \frac{t u_{l,o}}{\lambda_c}. \tag{3.34}$$

The dashed lines denote the running-time average which is averaging over elapsed time t of n steps

$$\langle \overline{w_l^*} \rangle = \frac{1}{t} \sum_n \langle w_l^* \rangle. \tag{3.35}$$

When the liquid supply was interrupted for a time period long enough to trigger the rapid rise in the surface superheat observed in the boiling crisis, dryout occurs. Here, this criterion for the dryout is when $\langle \overline{w_l^*} \rangle < 0.1$. These are marked in Figure 3.5(b) to (d).

Figure 3.5(a) defines the downstream location in the computational domain where the liquid track is evaluated for dryout or lack of it. Figures 3.5(b) to (d) show the dimensionless-time
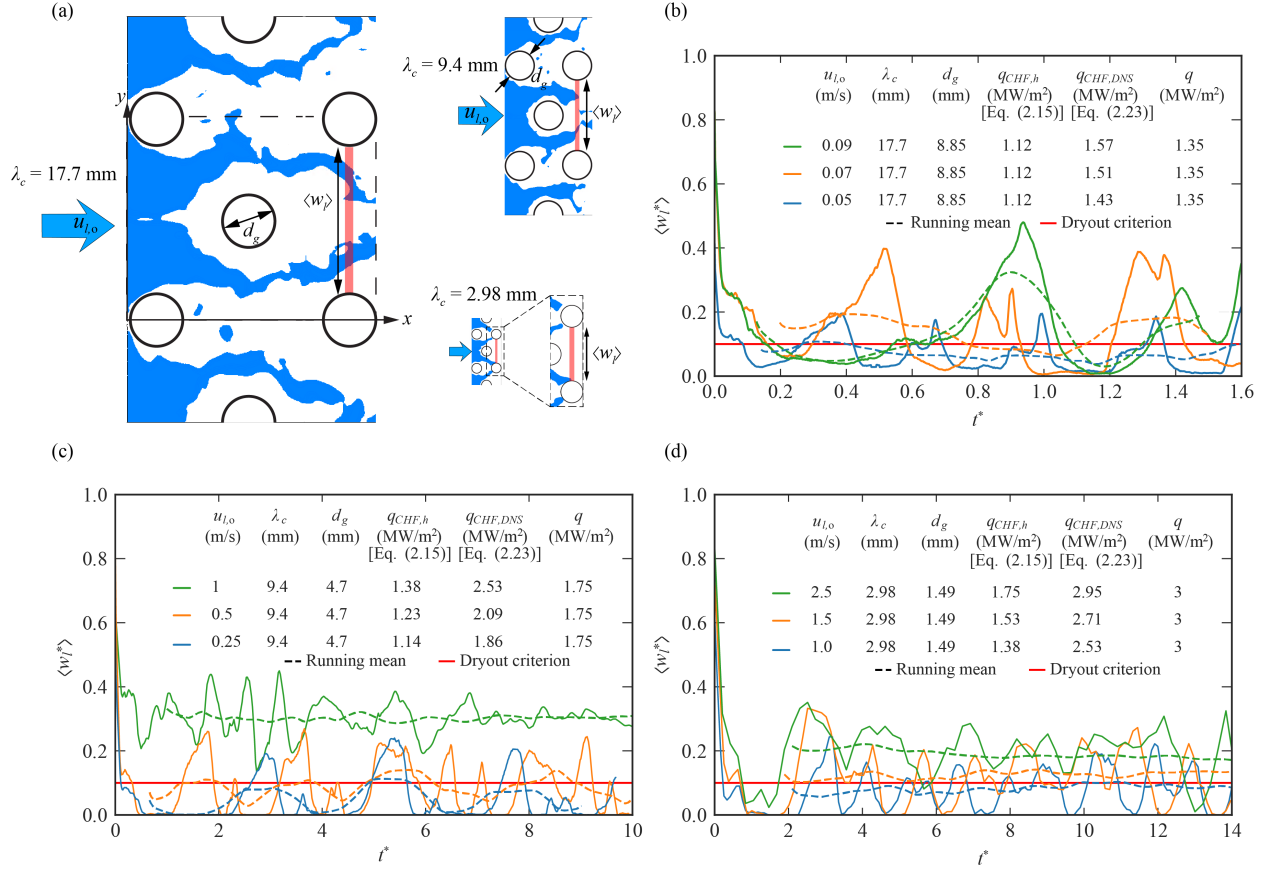
Figure 3.5: (a) Snapshots showing the liquid track width $\langle w_l \rangle$ at the location marked by the red strip. Time variations of the normalized liquid track width for (b) $q = 1.35\,\mathrm{MW/m^2}$ and $u_{l,o} = 0.05$, 0.07 and $0.09\,\mathrm{m/s}$, (c) $q = 1.75\,\mathrm{MW/m^2}$ and $u_{l,o} = 0.25$, 0.5 and $1.0\,\mathrm{m/s}$, and (d) $q = 3\,\mathrm{MW/m^2}$ and $u_{l,o} = 1$, 1.5 and $2.5\,\mathrm{m/s}$, respectively. The results are for saturated water at one atm.

variations of the dimensionless liquid track width $\langle w_l^* \rangle$, for different heat fluxes with progressively smaller inlet liquid velocities. In Figure 3.5(b), the heat flux is $q = 1.35\,\mathrm{MW/m^2}$, corresponding to $\lambda_c = 17.7\,\mathrm{mm}$ [Eq. (2.11)], and $u_{l,o} = 0.05$, 0.07 and $0.09\,\mathrm{m/s}$. The running-time average from Eq. (3.35) is shown with broken lines. The surface dryout criterion of $\langle w_l^* \rangle \leq 0.1$, marked by the red horizontal line, appears to present the breakup/interruption of the liquid track. Based on this, the dryout is marked for $u_{l,o} = 0.05\,\mathrm{m/s}$, since the running mean is consistently below this dryout criterion. Figure 3.5(c) is for $q = 1.75\,\mathrm{MW/m^2}$, corresponding to $\lambda_c = 9.4\,\mathrm{mm}$, and $u_{l,o} = 0.25$, 0.5 and $1.0\,\mathrm{m/s}$. Again, dryout is observed for the lowest velocity, i.e., $0.25\,\mathrm{m/s}$. Figure 3.5(d) shows the liquid track width variations for $q = 3\,\mathrm{MW/m^2}$, corresponding to $\lambda_c = 2.98\,\mathrm{mm}$, and

38

$u_{l,\mathrm{o}} = 1$, 1.5 and 2.5 m/s. Dryout is identified to occur when the liquid velocity is $u_{l,\mathrm{o}} = 1$ m/s.

The DNS allows for using Zuber pool-boiling surface unit-cell assumption and then adding the forced flow $u_{l,\mathrm{o}}$. The case of $u_{l,\mathrm{o}} = 0$ is not realized, but liquid velocities as small as 5 cm/s can be simulated without major computational time challenges. We will further discuss this in the next section.

Figure 3.6 shows the snapshots of the phase distributions for the nine flow-boiling conditions shown in Figure 3.5(b) to (d). The liquid-vapor interface is green and the surface liquid track is blue.
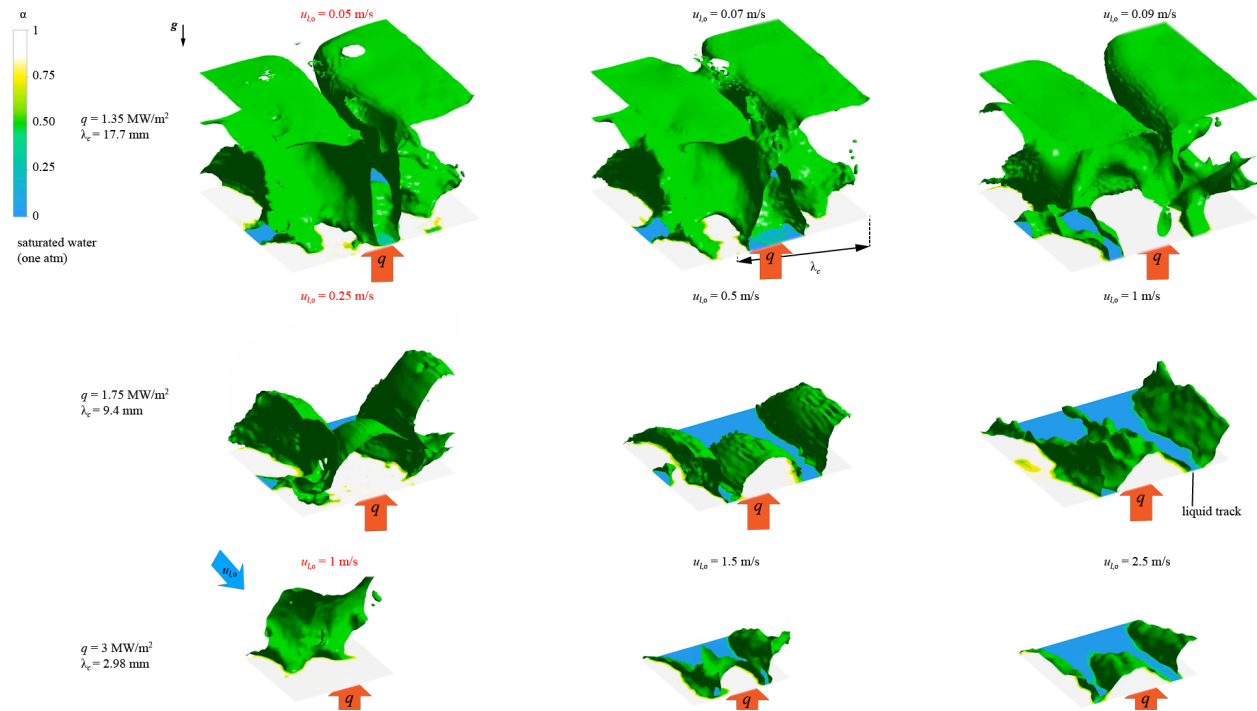
Figure 3.6: Snapshots of phase distribution and the liquid track for the nine DNS conditions, namely: $q = 1.35\,\mathrm{MW/m^2}$ and $u_{l,\mathrm{o}} = 0.05$, 0.07 and 0.09 m/s, $q = 1.75\,\mathrm{MW/m^2}$ and $u_{l,\mathrm{o}} = 0.25$, 0.5 and 1.0 m/s, and $q = 3\,\mathrm{MW/m^2}$ and $u_{l,\mathrm{o}} = 1$, 1.5 and 2.5 m/s, respectively. Velocities marked in red indicate cases for which dryout was observed. The results are for saturated water at one atm. The full video is available in the supplementary materials.

3.5 Temporal and spatial resolution convergence

The finest grid size investigated was $\Delta x_i = 0.15\,\text{mm}$. Increasingly coarser grid sizes were evaluated and the value of $\Delta x_i = 0.25\,\text{mm}$ was selected since it presented an error of $1.9\,\%$ at a reasonable computational cost. Although at a reduced computational cost, coarser grid sizes ($\Delta x_i = 0.40$ and $0.50\,\text{mm}$) resulted in inaccurate measurements (error too high). The adopted mesh with non-uniform grid size is shown in Figure 3.7. The aforementioned grid size corresponds to the region of the domain surrounding the heater.
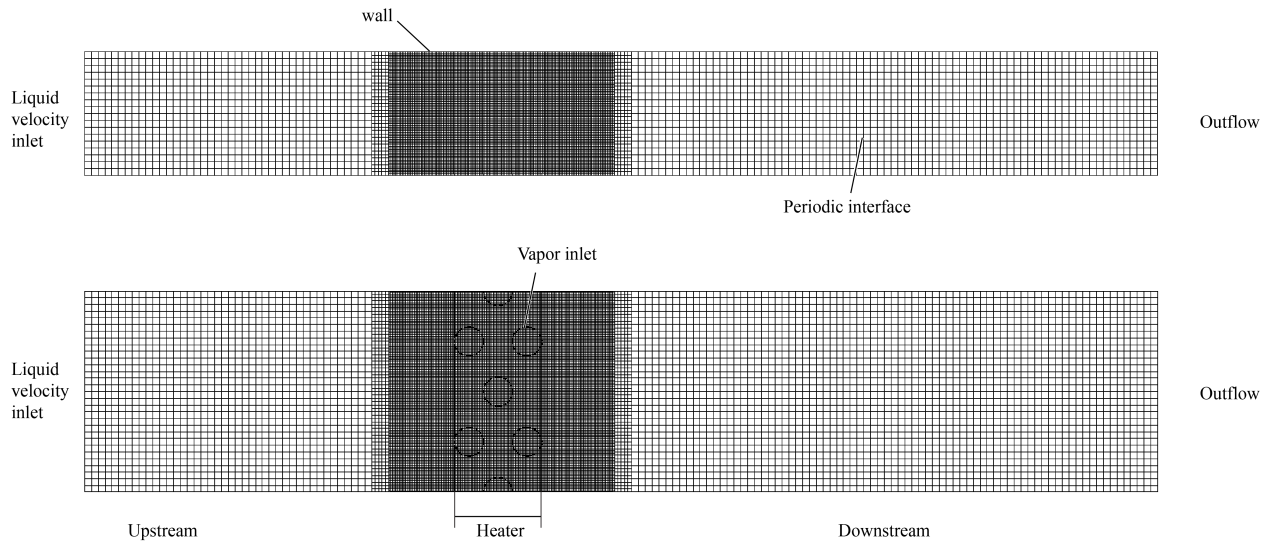
Figure 3.7: Side and top views of the CFD domain and the non-uniform squared grid. Boundary conditions are labeled.

As an example, Table 3.2 summarizes the variations of the running-time averaged liquid track $\langle \bar{w}_l^* \rangle$, defined by Eq. (3.35), with respect to progressively coarser grid size, for $q = 1.75\,\text{MW/m}^2$ and $u_{l,\text{o}} = 1\,\text{m/s}$ for saturated water at one atm. The mesh convergence is further discussed in [82].

The simulation time step restriction is based on the convection term, namely the Courant-Friedrichs-Lewy (CFL) condition [83], which states that the Courant number should be less than $\text{Co}_{max} = 0.25$

$$\text{Co} = \Delta t \left(\frac{\tilde{u}_f}{\Delta x} + \frac{\tilde{v}_f}{\Delta y} + \frac{\tilde{w}_f}{\Delta z} \right) \leq \text{Co}_{max}. \tag{3.36}$$

Table 3.2: Variation of running-time averaged dimensionless liquid track for $q = 1.75\,\mathrm{MW/m^2}$ and $u_{l,\mathrm{o}} = 1\,\mathrm{m/s}$.

Δx_i (mm)	$\langle \bar{w}_l^* \rangle$	$\frac{|\langle \bar{w}_l^* \rangle - \langle \bar{w}_l^* \rangle (\Delta x_i = 0.15)|}{\langle \bar{w}_l^* \rangle (\Delta x_i = 0.15)}$ (%)
0.15	0.303	0.0
0.25	0.309	1.9
0.40	0.343	13.2
0.50	0.376	24.1

The time step was selected to satisfy the CFL condition which, combined with the grid size, should result in $\mathrm{Co} \leq 0.25$. The adopted time step is $\Delta t = 0.25\,\mathrm{\mu s}$.

3.6 Summary

The CFD and the modeling used in the DNS of the flow boiling crisis within the wavelength modulation regime was presented. Relevant dimensionless numbers which represent the scaling of the four fundamental forces (inertial, viscous, gravity, and surface tension) and their ranges were listed and used to determine the constant adopted in the leading-edge surface liquid track crisis model. The velocity corresponding to the hydrodynamic CHF $q_{CHF,h}$, where the vapor-flow shear destabilizes the leading-edge surface liquid track and causes dryout, was encountered from the DNS for low, medium, and high velocities.

Proposed Porous Metasurface for Enhanced Flow-Boiling Critical Heat Flux and Thermal Conductance: Flow Boiling Canopy Wick

In this chapter, the use of porous metasurfaces for the boiling CHF and thermal conductance enhancement is described. A brief overview of the history of its usage for both pool- and flow-boiling applications is presented, culminating in the latest porous metasurface, the flow-boiling canopy wick, proposed in this work.

4.1   Evolution of Porous Metasurfaces for CHF Enhancement

Metasurfaces are unit-cell based, generally 3-D surface structures designed and fabricated for a targeted function. For example, in electromagnetic and sound wave applications they have sub-wavelength features capable of modulating the surface transmission, absorption and refection from phenomenon of interest [84, 85, 86].

The capillary, porous metasurfaces are employed in phase-change systems to provide continuous liquid supply to the heated surface, preventing dryout, while simultaneously removing the competition between liquid and vapor flows, known to trigger the hydrodynamic limit in the boiling crisis. Furthermore, due to capillary action a curved liquid meniscus is formed in the porous wick, leading to meniscus evaporation in place of ebullition. This meniscus evaporation requires

42
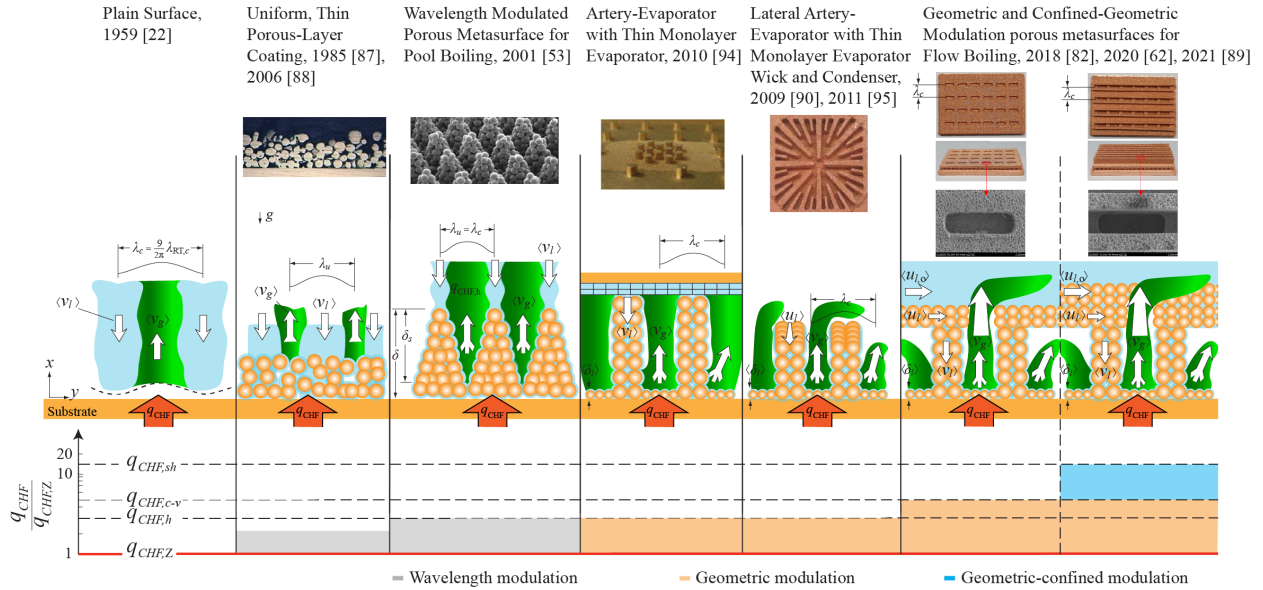
Figure 4.1: An evolution of porous metasurfaces for enhanced CHF [43], updated with the flow-boiling canopy wick metasurface [62, 89]. The porous coatings are made of sintered copper particles. The corresponding q_{CHF} in the three enhancement regimes, wavelength-modulation, geometric modulation, and confined-geometric modulation, are also shown.

smaller superheat due to the high-conductivity solid particles, reducing the phase-change thermal resistance [43].

The evolution of boiling porous metasurfaces for enhancing the CHF is shown in Figure 4.1, employing capillary evaporator wicks. The baseline of comparison is the pool-boiling CHF theory by [22]. As summarized in Section 2.1, at the CHF, the rising vapor jets arranged in a square array would prevent the liquid supply to the heated surface, initiating the boiling crisis. Initial attempts employed uniform porous coatings to increase the CHF over the plain surface [87]. The liquid imbibition of the wick close to the wall ensured a delayed dryout condition, allowing for higher hydrodynamic CHF to be reached. The hydrodynamic aspects were also investigated in [88]. The authors attributed the 2-fold CHF enhancement over the plain surface to the changes in the critical R-T wavelength. The surface superheat reduction was also observed in [88], thinner wicks, using sintered particles with smaller diameter, resulted in a lower superheat, indicating the dominance of conduction across the layer, based on an effective thermal conductivity and an average coating thickness.

The first porous metasurface sub-wavelength modulation of the interfacial pool boiling critical wavelength was suggested and tested in [53], reducing the superheat and enhancing the CHF using sintered copper particles in the form of modulated conical structures designed to drive liquid towards the heated surface while allowing for escaping vapor to rise through otherwise empty spaces. In [90], it was shown that the wavelength modulation is the main cause for CHF enhancement, with the wick parameters (porosity, permeability) having little effect. The manufacturing process of the modulated porous coating (compaction pressure, sintering temperature) was also investigated in [91]. As discussed in Sections 2.1 and 2.2, the CHF enhancement over the plain surface (up to 3-fold for n-pentane) was due to the modulation of the critical wavelength achieved by the spacing between the sintered conical structures.

In the studies [87, 53, 88], boiling was still the dominant phase-change mechanism. With the aim of promoting meniscus evaporation, the 3-D capillary structures for phase separation using columnar and lateral arteries have been designed for irrigation and evaporative cooling of concentrated heat sources for round heat pipes [92] and vapor chambers [93]. In [94], the authors used a thin (single-layer) evaporator wick to reduce the thermal resistance, in accordance to the observations from [88]. This thin evaporator wick allowed for the formation of the liquid meniscus at a low enough hydraulic resistance. The liquid supply was handled by columnar arteries that collected the condensate and directed it to the heated surface at minimal viscous pressure drop. The reduction in thermal resistance was attributed to meniscus recession: at higher heat fluxes, the liquid consumption increases, increasing the filtration velocity and pressure drop in the wick. The meniscus recedes to accommodate the needed capillary pressure, reducing also the path from the heater to the liquid-vapor interface where meniscus evaporation takes place [94]. This physical mechanism will be further discussed in Section 5.2.

In [95, 96], the concept of hybrid wicks is further extended with the use of lateral arteries for the liquid transport. Optimal liquid supply and heat transfer have different requirements that cannot be easily met simultaneously. Thick transport wicks require high permeabilities and use large particles (low hydraulic resistance), while thin evaporating wicks require smaller particles

(low thermal resistance) with high pressure drop. The solution was to separate the liquid supply and heat transfer functions. The liquid supply structure is located on top of the liquid spreading layer to continuously deliver liquid to multiple spots, thus preventing dryout at high heat flux. The generated vapor escapes through the spacing in between transport structures.

Figure 4.1 shows the schematic of metasurfaces and their physical images, as well as the CHF enhancement compared to the Zuber $q_{CHF,Z}$. Also shown in Figure 4.1, is the recent work on raising $q_{CHF,h}$ by preventing the onset of Kelvin-Helmholtz instabilities with the flow-boiling canopy wick (FBCW), a 3-D (and multiscale) porous metasurface that modulates vapor-escape sites (vapor perforations) [82, 62]. The shaded areas at the bottom correspond to the measured enhancement achieved in the wavelength modulation discussed Chapter 3, and geometric modulation and geometric-confined modulation regimes discussed in Chapters 7 and 8.

4.2   Flow-Boiling Canopy Wick

In flow boiling, the incoming liquid flow is disturbed by the generated vapor, which hinders the axial liquid supply. The vapor-flow shear destabilizes the leading-edge surface liquid track, causing the dryout. The Flow-Boiling Canopy Wick (FBCW) builds upon the groundwork laid by its predecessors illustrated in Figure 4.1 and the core concepts of these porous metasurfaces for the CHF enhancement are combined in this 3-D, multiscale wick. The capillary wick separates the liquid and vapor phases and directs the liquid from the liquid channel to the thin evaporator wick with high capillary pressure capability and this reduces the thermal resistance. It allows for a vapor space in between the liquid transport arteries over the evaporator for achieving large thermal conductance and vapor escape sites (perforations) directing the vapor into the liquid channel. Its three main components are the evaporator, posts, and perforated canopy. They are illustrated in Figure 4.2.

All three porous components, canopy wick, posts, and thin evaporator wick, coordinately direct the liquid towards the heated surface. Liquid is assumed to be saturated in the channel and canopy

45

and post wicks. The thin wick evaporator is responsible for spreading and evaporating the liquid with low resistance (thermal and hydraulic), generating saturated vapor. The posts separate the evaporator and the canopy and form the vapor space. They are the columnar arteries responsible for supplying liquid to the thin evaporator wick at a reduced hydraulic resistance. The axial and lateral post spacing play a major role in the viscous pressure drops in the thin evaporator wick, since the average distance between the liquid supply points controls the characteristic length travelled by the fluid particle in the evaporator wick.

The perforated canopy is where the vapor wavelength modulation occurs, since it separates the phases and controls the vapor sites entering the liquid channel at regularly spaced perforations. It also separates the liquid stream from the vapor space and promotes the capillary suction of the liquid track into the wicking system. The vapor escaping through the perforations mixes with the liquid above the canopy, what creates a two-phase hydrodynamic-stability controlled CHF above the canopy. The primary instability is related to the leading-edge liquid track which supplies the liquid to canopy which directs it to the evaporator (monolayer) through the posts. At high heat flux, the accumulated vapor flowing above this liquid track causes a shear instability. Below the canopy, the capillary-viscous controlled CHF governs the liquid permeation, evaporation and vapor venting. The addition of levees to the side of the perforations further stabilizes the liquid track through its geometric-confinement. This directs the vapor over the liquid track and into the channel flow, away from the canopy where the surface liquid track initiates the liquid supply.

The high velocity of the liquid being wicked across the canopy and posts leads to high Péclet number, resulting in negligible upstream thermal conduction [53]. At the thin wick evaporator, the sintered particles contribute to an increased effective thermal conductivity, reducing the thermal resistance [63]. The thin wick evaporator has an optimal permeability and capillary pressure and spreads the liquid supplied through the posts. The aim is to create and maintain a vapor space for steady and uniform film evaporation over the heated surface, while allowing for uninterrupted liquid supply represented by the leading-edge liquid track. In the channel, vapor-shear will eventually destabilize the surface-liquid track and trigger the CHF, however, the design of the optimized

46

perforation arrangement (geometry and pitch) in the FBCW allows for an additional modulation regime, the Geometric Modulation Regime (GMR), discussed in Chapter 7, far more effective than the WMR discussed in Section 2.3.
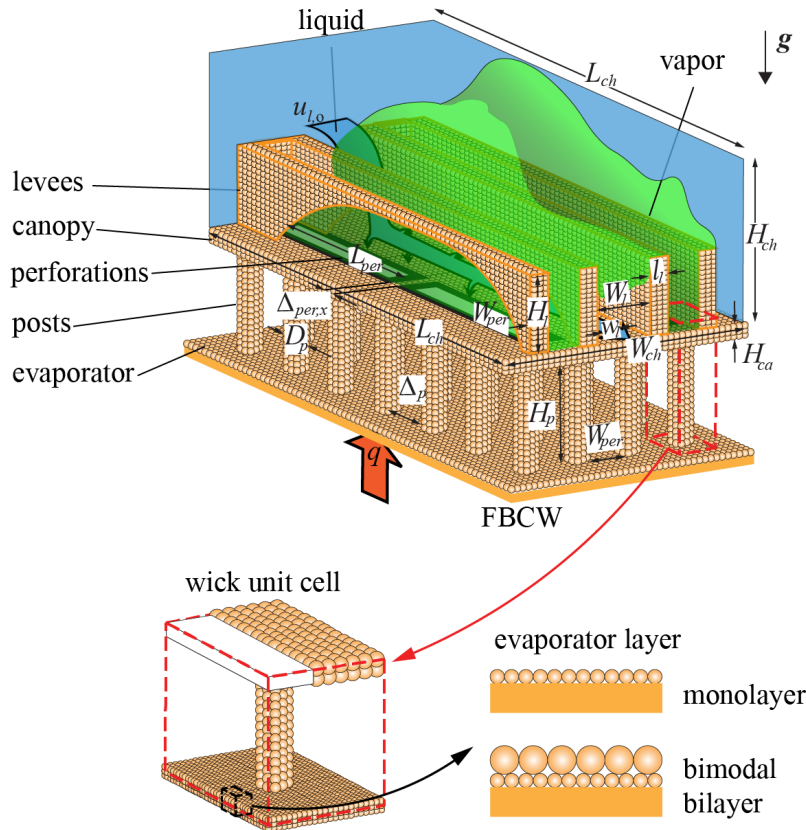
Figure 4.2: Schematic illustration of the flow-boiling canopy wick.

As mentioned earlier, levees are introduced around the perforations to protect the leading-edge liquid track (and increase the dryout limit) from the axial vapor acceleration which combined with the liquid permeation toward the evaporator lead to thinning of the liquid track and its instability. The modulation due to this confinement effect is called Confined-Geometric Modulation Regime (C-GMR), and is discussed in Chapters 7 and 8.

By eliminating the competition between the phases close to the heated surface and allowing for a continuous supply of the liquid through its capillary structure, the FBCW aims to control and enhance the CHF and the thermal conductance. The liquid flow path from the channel to the heated surface goes through the canopy, posts, and evaporator layer, and each component has

its associated pressure drop. Furthermore, the vapor escape through the perforations causes an additional pressure drop that must also be accounted for by the capillary wick. The combined pressure drops cannot exceed the maximum capillary pressure $p_{c,max}$, i.e.,

$$\sum \Delta p_i = \Delta p_e + \Delta p_{po} + \Delta p_{ca} + \Delta p_{per,g} \leq p_{c,max}, \tag{4.1}$$

The maximum total pressure drop allowed corresponds to the capillary-viscous heat flux limit $q_{CHF,c-v}$ (CHF controlled by the evaporator maximum capillary pressure). These pressure drops are illustrated in Figure 4.3.

Figure 4.3: Schematic representation of viscous and inertial pressure drop components along the liquid and vapor paths in the wick side.

The modeling for each pressure drop component and the maximum capillary pressure is presented in Chapter 5 for different evaporator layer wick configurations.

4.3 FBCW Unit Cell

As discussed in Section 4.2, the capillary-viscous limit is the heat flux for which Eq. (4.1) is satisfied. It depends on the maximum capillary pressure which occurs in the thin evaporator wick, and the summation of liquid and vapor pressure drops in the 3-D canopy wick. The FBCW unit

cell is illustrated in Figure 4.4.

Figure 4.4: The FBCW unit cell showing the geometric parameters of the channel and the wick.

The FBCW is the ensemble of three wicks:

Perforated canopy wick: perforated porous layer which separates the inertia-dominated two-phase flow above it from the capillary-dominated, separated liquid and gas flows. The periodic perforation slots allow for the vapor venting and formation of the leading-edge liquid track. Perforation width W_{per} and length L_{per}, as well as the number of perforations A_{per} are designed to minimize the escaping vapor pressure drop $\Delta p_{per,g}$.

Post wicks: arranged as anisotropic unit cell and between the perforations, with their lateral spacing limited by the perforation width. The parameters are the post diameter D_p, post spacing $\Delta_{p,x}$ and $\Delta_{p,y}$, the number of posts along the perforation $N_{p,x}$ and perpendicular to the flow $N_{p,y}$, and the perforation width W_{per}. The perforation width is limited by the capillary length, given by Eq. (2.5). The perforation length accounts for two posts along the perforation and an additional post between each perforation, resulting in

$$L_{per} = N_{p,x}\Delta_{p,x} + (N_{p,x} - 1)D_p. \tag{4.2}$$

49

Table 4.1: The FBCW geometric parameters written in terms of the post diameter D_p, post spacing $\Delta_{p,x}$, the number of posts along the perforation $N_{p,x}$, and the perforation width W_{per}.

$W_c = 2(W_{per} + D_p)$	$A_{base} = W_c L_c$
$L_c = L_{per} + D_p$	$A_{per} = W_{per} L_{per}$
$l_w = (L'_p - D_p)/3$	$A_{ca} = A_{base} - A_{per}$
$W_l = 2D_p + W_{per}$	$A_{po} = N_{p,x}\pi D_p^2/4$
$l_{per} = D_p$	

Thin evaporator wick: ideally a single layer of close-packed, sintered spherical diameter particles covering the heated surface and allowing for evaporation. It has an effective conductivity that along with the wick small thickness results in large thermal conductance. The evaporator wick unit cell is centered around the post with an equivalent diameter

$$L'_p = \left[\frac{4}{\pi}\left(W_{per} + D_p\right)\left(\Delta_p + D_p\right)\right]^{1/2}. \tag{4.3}$$

Table 4.1 brings a summary of relevant FBCW unit cell geometric parameters.

4.4 Summary

The FBCW was introduced and its mechanisms for the control of liquid and vapor flows, for preventing the boiling crisis, as well as enhancing the thermal conductance, were explained. A brief overview of the evolution of the use of porous metasurfaces for the CHF enhancement was presented, highlighting relevant physical parameters and mechanisms that allow for greater enhancement.

CHAPTER 5

The Porous-Metasurface Capillary-Viscous Critical Heat Flux and Thermal Conductance

In this chapter, the limitations associated with the FBCW are discussed. The flow-boiling crisis mechanism changes under the FBCW are discussed. The theory of capillary-viscous critical heat flux $q_{CHF,c-v}$ is derived based on the volume-averaged wick processes and properties.

5.1 CHF Limits

Regarding the boiling crisis, coatings reduce the surface superheat $T_s - T_{lg}$ by either assisting in increasing the nucleation sites or in creating film evaporation across thin, permeable coatings. They also enhance the capillary-viscous CHF, $q_{CHF,c-v}$, governed by the liquid-vapor hydrodynamic instability or by the capillary-viscous limit of liquid flow through porous bodies. The 3-D wick separates the liquid and vapor phases, therefore, reducing the liquid-vapor counter-flow resistance adjacent to the surface. Both the hydrodynamic and capillary limits can cause liquid choking and lead to CHF. The liquid-choking limit is predicted to occur first (the lower of the two limits), with increasing surface heat flux q. The vapor escape paths are more readily accommodated. The departing bubbles and imbibing liquid compete at the heated surface, leading the dryout at high heat flux, such as the hydrodynamic CHF $q_{CHF,h}$.

In saturated flow boiling, after a threshold in liquid velocity, this $q_{CHF,h}$ becomes greater than the corresponding pool-boiling limit. This is because the axial liquid inertia can more effectively

counter the deflected departing bubbles (or vapor columns in the boiling crisis hydrodynamic sta-bility theory). It is given by Eq. (2.23) according to the leading-edge surface liquid track dryout model discussed in Section 2.3

Other than the hydrodynamic and capillary-viscous CHF, other events can limit heat transfer, they are:

Vapor kinetic theory limit, q_{max}: the theoretical upper limit of the vapor mass flux (one-dimensional molecular or thermal flow) due to evaporation. The maximum theoretical heat flux is defined as [97]

$$q_{max} = \rho_g \Delta h_{lg} \left(\frac{k_B T_{lg}}{2\pi M} \right)^{1/2}, \tag{5.1}$$

where k_B is the Boltzmann constant and M is the molar mass.

Vapor choking limit, $q_{CHF,ch}$: the vapor from the monolayer wick surface flows through the vapor space and to the perforations, and this reduction in flow cross-section area increases the velocity from $v_{g,m}$ to $v_{g,per}$ and can reach the sonic limit. The choking limit is [98]

$$q_{CHF,ch} = c_d \frac{A_{per}}{A_m} \Delta h_{lg} \left[\gamma \rho_g p_g \left(\frac{2}{\gamma+1} \right)^{(\gamma+1)/(\gamma-1)} \right]^{1/2}, \tag{5.2}$$

where c_d is the discharge coefficient, γ the heat capacity ratio, and p_g the vapor pressure in the evaporator wick.

Vapor compressibility limit, $q_{CHF,Ma}$: our analysis assumes incompressible flows, so the vapor Mach number $Ma_{g,per}$ is kept below 0.3 [99]. So, we use the vapor compressibility limit which is more restrictive compared to the vapor choking limit. The compressibility limit is calculated as

$$q_{CHF,Ma} = \rho_g \Delta h_{lg} \frac{A_{per}}{A_e} u_a Ma_{g,per}, \tag{5.3}$$

where u_a is the vapor speed of sound.

Liquid superheat limit, $q_{CHF,sh}$: the liquid inside the monolayer wick is superheated (ΔT_{sh}) and when this superheat exceeds a maximum $\Delta T_{sh,max}$, then bubbles are formed in the wick and hin-

der the liquid flow and cause dryout. The superheating limit is calculated with volume-averaged evaporator wick properties as follows

$$q_{CHF,sh} = \frac{\langle k \rangle_e}{\langle \delta \rangle_e} \Delta T_{sh,max} = \frac{G}{A} \Delta T_{sh,max},$$ (5.4)

where the maximum critical superheat $\Delta T_{sh,max}$ is determined by the critical nucleation site radius as

$$\Delta T_{sh,max} = \frac{T_{lg}}{\Delta h_{lg} \rho_g} \left(\frac{2\sigma}{r_c} - p_{c,max} \right).$$ (5.5)

For a single layer evaporator wick, with copper particles oxidized for improved wetting, the adopted r_c is in order of $100\,\text{nm}$ [95].

The capillary-viscous limit and the hydrodynamic limit are the most relevant. The former will be discussed in the sequence, and the latter was presented in Chapters 2 and 3. The other limits were first discussed in previous works [100, 82, 63].

5.2 Capillary-Viscous Critical Heat Flux

5.2.1 Wick Pressure Drop Components

Each wick pressure drop presented in Eq. (4.1) was calculated by employing the Darcy law [101]

$$\Delta p_i = \frac{\mu_l \langle u_{l,i} \rangle L_i}{K_i},$$ (5.6)

where $\langle u_l \rangle$ is the filtration velocity, L the path length, $i = e, p, ca$, and K the permeability. For low particle Reynolds numbers, $\text{Re}_{d,p} = \rho_l \langle u_l \rangle d_p / [\mu_l (1 - \epsilon)] < 1$, the viscous forces dominate and the Darcy law can be used. At higher particle Reynolds number $\text{Re}_{d,p}$, departure from the Darcean regime is observed due to the contributions from inertial forces in the Forchheimer regime [101, 102, 103]. The pressure drop across the wick is given as

$$\Delta p_i = \frac{\mu_l \langle u_{l,i} \rangle L_i}{K_i} + C \frac{\rho_l \langle u_{l,i} \rangle^2 L_i}{K_i^{1/2}}. \tag{5.7}$$

For heat flux up to $q = 20\,\mathrm{MW/m^2}$, it was shown that the inertial forces are negligible [82]. Nonetheless, as will be discussed in Chapter 6, the inertial effects were considered in the numerical solvers.

For the post and canopy, the average wick permeability is estimated by employing the Carman-Kozeny relation [101]

$$K_i = \frac{d_i^2 \epsilon^3}{180 \left(1 - \epsilon_i\right)^2}, \tag{5.8}$$

where ϵ is the wick porosity. The calculation of the permeability for the evaporator wick depends on the wick configuration (particle arrangement) and the meniscus topology since the cross-section area available for the liquid to flow through grows thinner away from the posts due to evaporation. This is illustrated in Figure 5.1.
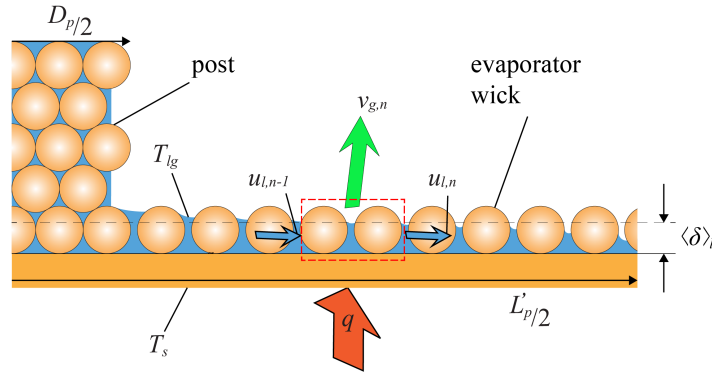
Figure 5.1: Schematic representation of the radial variations of the liquid film thickness in the evaporator wick due to the meniscus evaporation. Due to symmetry, half of the post-monolayer unit cell is shown.

The permeability of the evaporation layer is then

$$K_e = \frac{\mu_l \langle u_l \rangle}{-\frac{dp}{dx}}, \tag{5.9}$$

where the pressure gradient $\frac{dp}{dx}$ is found from numerical simulations, discussed in Chapter 6. The

average pressure drop in the evaporator layer is found by integrating Eq. (5.9) using an area-averaged permeability $\langle K_e \rangle$, according to Figure 5.1

$$\Delta p_e = \frac{\mu_l \langle u_{l,e} \rangle l_w}{\langle K_e \rangle}, \tag{5.10}$$

where l_w is the average wicking length. The local velocity distribution can be found from the continuity equation and it will be discussed in Chapter 6. The average wick velocity is found from the heat of evaporation and the heat flux

$$\langle u_{l,e} \rangle = \frac{q A_e}{\rho_l \Delta h_{lg} A_{flow}}, \tag{5.11}$$

where $A_e = \pi(L_p'^2 - D_p^2)/4$ and $A_{flow} = \pi \langle \delta_l \rangle \left(L_p' + D_p \right)/2$. Combining Eqs. (5.10) and (5.11), we find

$$\Delta p_e = \frac{\mu_l}{\rho_l \Delta h_{lg}} \left[\frac{l_w}{\langle K_e \rangle} \frac{4(L_p'^2 - D_p^2)}{\langle \delta_l \rangle \left(L_p' + D_p \right)/2} \right] q_{CHF,c-v}, \tag{5.12}$$

where $l_w = (L_p' - D_p)/3$ is the wicking length, validated with numerical simulations and experimental results discussed in Chapters 6 and 9.

The vapor pressure drop across the perforation experienced inertial dominance

$$\Delta p_{per,g} = \frac{C \rho_g v_g^2}{2}, \tag{5.13}$$

where v_g is the vapor velocity before the perforation, and C the inertial coefficient [104].

5.2.2 Wick Maximum Capillary Pressure

The capillary pressure is the pressure jump across the liquid-vapor interface [101]

$$p_c = p_l - p_g = \frac{2\sigma \cos \theta_c}{r_c}, \tag{5.14}$$

where θ_c is the contact angle and r_c the radius of curvature of the liquid meniscus.

From Eq. (5.14), it can be seen that in a capillary wick, the radius of curvature of the meniscus is adjusted to compensate for the existing pressure drops in the wicking path. The liquid anchors to the solid particles and the meniscus surface is curved to provide increased capillary pressure. The meniscus topology is determined according to the contact angle and the minimum surface energy principles. The upper limit of this adjustment corresponds to the maximum capillary pressure $p_{c,max}$, after which the wick can no longer support continued capillary action. At this critical radius of curvature, a meniscus jump occurs indicating no solution or reaching the maximum capillary pressure. This corresponds to dryout.

In order to verify the meniscus topology, the Surface Evolver (SE) solver is used [105]. The solver uses the principle of energy minimization to iteratively determine the meniscus topology. The following energy equation is minimized using the conjugate gradient method

$$E = \int F_e dl + \iint \sigma dA + \iiint (p + \rho g z) dV, \qquad (5.15)$$

where F_e is the tension in the contact line, σ is the surface tension between liquid and vapor, and p is the pressure. The last term represents the pressure work realized on the fluid by the combination of the pressure boundary condition and the fluid column. The meniscus curvature is found from the prescribed pressure boundary condition subject to the surface tension constraint, since the mean curvature is related to pressure according to Eq. (5.14). Due to the small particle diameters (order of 10-100 μm), the Bond number is small and the effect of the gravity is negligible. The mesh creation process for the solid particle and liquid volume, as well as the convergence methods utilized, are discussed in further detail in [106, 100, 63].

The SE employs dimensionless parameters and variables [105], so the dimensionless capillary pressure p_c^* is prescribed in the code as a boundary condition. After a convergence is achieved by employing the surface energy minimization algorithm, a new liquid meniscus topology is realized for the given p_c^*. By scanning the p_c^*, a direct relationship between the liquid thickness and p_c^* can be established. The maximum capillary pressure corresponds the prescribed $p_{c,max}^*$, where the last stable meniscus was realized. Near the maximum capillary pressure, convergence becomes

56

challenging and simulations can become lengthy, depending on the mesh refinement level. The dimensional $p_{c,max}$ corresponding to the prescribed $p^*_{c,max}$, when the critical radius of curvature is reached before the meniscus jump, is found according to [106]

$$p_{c,max} = -\frac{p^*_{c,max}\sigma\cos\theta_c}{d_p}, \tag{5.16}$$

where d_p is the particle diameter. The expression from Eq. (5.16) utilizes the particle diameter as the length scale. It is similar to the Leverett function [107], a scaled capillary pressure,

$$p_{c,max} = J(s=0)\frac{\sigma\cos\theta_c Z(\theta_c)}{(K/\epsilon)^{1/2}} = C_J\frac{\sigma}{(K/\epsilon)^{1/2}}, \tag{5.17}$$

where $J(s)$ is the Leverett function, $Z(\theta_c)$ is the Melrose function, $(K/\epsilon)^{1/2}$ is the length scale, and $C_J = J(s=0)\cos\theta_c Z(\theta_c) = 0.53$ is a constant [53].

The variations of the meniscus topology for an ideal one-layer thick evaporator (monolayer) with the hexagonal packing with the dimensionless capillary pressure, p^*_c, is shown in Figure 5.2. For higher dimensionless capillary pressures, Figure 5.2 shows a smaller curvature radius, until the critical radius at the maximum capillary pressure, according to Eq. (5.16). The volume-averaged liquid thickness $\langle\delta_l\rangle$ is also shown, it corresponds to the liquid thickness if the meniscus topology was flat at a given p^*_c.

5.2.3 Capillary-Viscous Limit

The capillary-viscous limit $q_{CHF,c-v}$ is found by solving Eq. (4.1). Similar to Eq. (5.12), all pressure drop components can be related to the heat flux q. The canopy and post liquid filtration velocities are, respectively

$$\langle v_{l,ca}\rangle = \frac{q}{\rho_l\Delta h_{lg}}\frac{A_{base}}{A_{ca}}, \tag{5.18}$$

$$\langle v_{l,po}\rangle = \frac{q}{\rho_g\Delta h_{lg}}\frac{A_{base}}{A_{po}}. \tag{5.19}$$
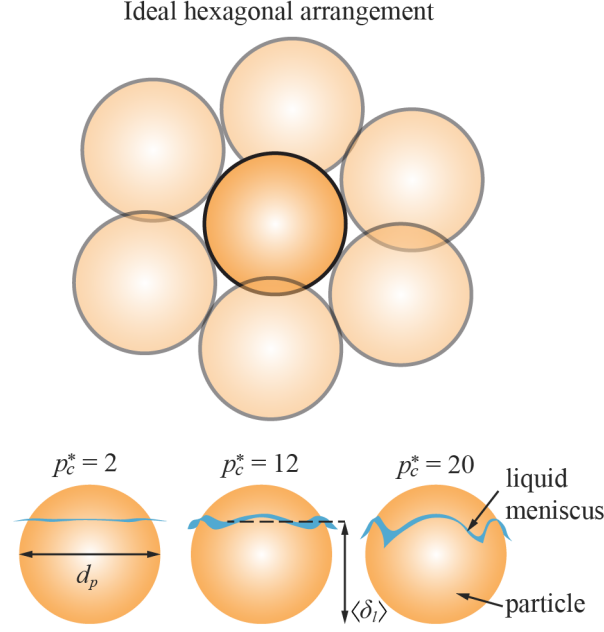
Figure 5.2: Illustration of the liquid meniscus topology with different p_c^* for saturated water (one atm) and copper particles in ideal monolayer packing (hexagonal arrangement, $d_p = 50$ μm). Perspective and side views are shown.

The same can be done for the vapor velocity before the perforation

$$\langle v_{g,o} \rangle = \frac{q}{\rho_l \Delta h_{lg}}. \tag{5.20}$$

The expression from Eq. (4.1) can then be rewritten as

$$\frac{\mu_l}{\rho_l \Delta h_{lg}} \left[\frac{l_w}{\langle K_e \rangle} \frac{4(L_p'^2 - D_p^2)}{\langle \delta_l \rangle \left(L_p' + D_p \right)/2} \right] q_{CHF,c-v} + \frac{\mu_l H_p}{K_p} \frac{q_{CHF,c-v}}{\rho_l \Delta h_{lg}} \frac{A_{base}}{A_{po}} + $$
$$\frac{\mu_l H_{ca}}{K_p} \frac{q_{CHF,c-v}}{\rho_l \Delta h_{lg}} \frac{A_{base}}{A_{ca}} + \frac{C\rho_g}{2} \frac{q_{CHF,c-v}^2}{\rho_g^2 \Delta h_{lg}^2} = p_{c,max}, \tag{5.21}$$

the canopy pressure drop term can be neglected since numerical results show it is orders of magnitude smaller than the others Chapter 6. Rearranging Eq. (5.21), we find a quadratic expression for the capillary-viscous limit

$$\frac{C}{2\rho_g \Delta h_{lg}^2} q_{CHF,c-v}^2 + \frac{\mu_l}{\rho_l \Delta h_{lg}} \left[\frac{l_w}{\langle K_e \rangle} \frac{4(L_p'^2 - D_p^2)}{\langle \delta_l \rangle \left(L_p' + D_p \right)/2} + \frac{H_p}{K_p D_p^2} \right] q_{CHF,c-v} = p_{c,max}. \quad (5.22)$$

The final expression from Eq. (5.22) is solved numerically and analytically in Chapter 6 and the results are compared to experimental results in Chapter 10.

5.2.4 FBCW Thermal Conductance

As observed in [94], the thermal conductance of thin evaporator wicks depends on the wick effective thermal conductivity $\langle k \rangle_e$ and the meniscus liquid height $\langle \delta_l \rangle_e$, i.e.,

$$\frac{G}{A} = \frac{\langle k \rangle_e}{\langle \delta_l \rangle_e} = \frac{q}{T_s - T_{lg}}. \quad (5.23)$$

The heat is conducted through the thin evaporator wick with its pores occupied by liquid. The meniscus adjusts its topology according to the capillary pressure. At high heat flux, additional liquid supply is required due to the increased evaporation rate. The filtration velocity in the transport arteries and the corresponding viscous pressure drop are also increased, leading to a higher capillary pressure requirement, according to Eq. (4.1). The meniscus then recedes to provide the increased capillary pressure, leading to a reduction in the heat path from the heater to the meniscus evaporation, effectively reducing the thermal resistance. Additionally, due to meniscus evaporation, the liquid film thickness is thinner away from the posts, which also reduces the conduction path and the thermal resistance. Figure 5.1 illustrates the meniscus recession and the film thinning due to evaporation. The effective thermal conductivity calculation is discussed in Chapter 6.

5.3 Summary

The FBCW porous metasurface was discussed in detail. The wick-controlled capillary-viscous critical heat flux $q_{CHF,c-v}$ was derived based on the pressure drop from the 3-D multiscale wick

and its unit-cell geometry. The mechanism for thermal conductance enhancement was discussed. The other critical heat flux limits occurring in flow boiling were also presented.

CHAPTER 6

Direct Numerical Simulation of Capillary-Viscous Flow and Heat Transfer in Flow-boiling Canopy Wick

In this chapter, the DNS and modeling of the FBCW are presented. Both the 3-D CFD and 1-D network transport models are used for the prediction of the liquid and vapor flows. The wick properties (volume-averaged properties such as the permeability, capillary pressure, and effective thermal conductivity) are found from the bulk relationships or from direct (pointwise) numerical simulation. The capillary pressure and wick permeability are related to the capillary-viscous limit and the effective thermal conductivity is related to both the superheat limit and the wick thermal conductance.

6.1   Wick Effective Properties

As discussed in Section 5.2, the calculation of pressure drop and thermal resistance in the evaporator wick requires knowledge of the wick effective (volume-averaged) properties, namely the permeability, capillary pressure, and thermal conductivity. The properties in the liquid spreading wick deviate from the bulk porous media values such as the Carman-Kozeny relation for permeability [101] and the Hadley correlation for thermal conductivity [108], due to the changes in the liquid content.

6.1.1 Maximum Capillary Pressure

The ideal FBCW sintered, spherical particle evaporator wick, uses a single layer of unit-cell hexagonal packing on top of the heated surface, as depicted in Figure 5.2, for a particle of diameter d_e. The close packing of the monolayer without heterogeneity is rather impossible. The simplest heterogeneity model has a particle vacancy at the center of the unit cell, as illustrated in the SEM micrograph of Figure 6.1 for a typical sintered monolayer wick ($d_e = 50\,\mu m$).
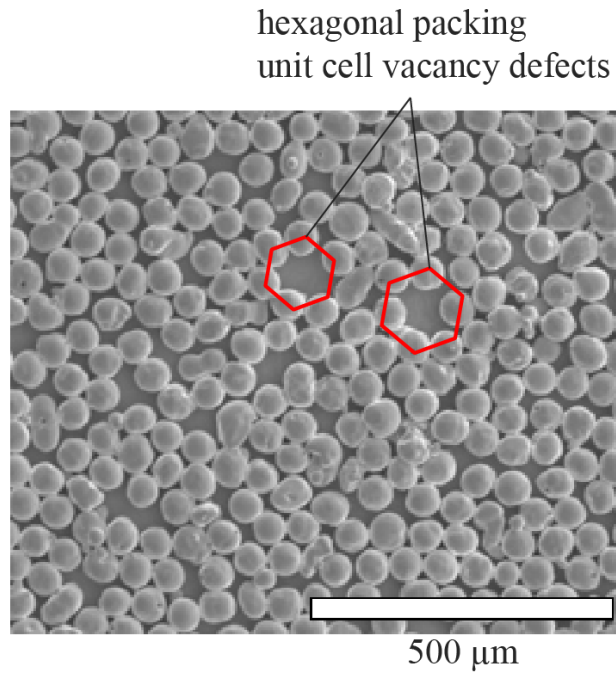
Figure 6.1: SEM image of the sintered monolayer wick indicating vacancy defects (heterogeneities). The idealized hexagonal packing arrangement with a vacancy is highlighted.

The maximum capillary pressure $p_{c,max}$ for a given evaporation layer packing is calculated using the SE solver. As discussed in Section 5.2.2, a dimensionless capillary pressure p_c is prescribed as the boundary condition and then Eq. (5.15) is minimized using the conjugate gradient method by changing the meniscus curvature. The maximum capillary pressure for the ideally-packed monolayer wick with $d_e = 50\,\mu m$ is found to be $p_{c,max} = 16.2\,kPa$. This high value is desirable since it allows for very high $q_{CHF,c\text{-}v}$, but could not be achieved in experiments due to the presence of heterogeneities such as the ones illustrated in Figure 6.1. The vacancy defects significantly reduced

the maximum capillary pressure compared to the ideal packing, because the liquid meniscus is stretched over a large length between the anchoring contact line points, reducing the principal radii of curvature. For the modeled monolayer with the same particle size and with a vacancy defect, the computed maximum capillary pressure is $p_{c,max} = 2.32\,\text{kPa}$, which is significantly lower than that for the ideal wick.

As a solution, the use of a bimodal bilayer evaporator with larger particles ($d_e = 100\,\mu\text{m}$) in the second layer is proposed. The larger particles from secondary layer can occupy the vacancy defect spacings, providing a new anchoring point for the liquid meniscus. For the ideal bimodal bilayer wick, three meniscus-anchoring regimes exist, namely (i) liquid above the first layer, with the meniscus anchored only to the large particles; (ii) liquid receding and transitioning from the second to the first layer, anchoring to both large and small particles; (iii) liquid below the second layer, with the meniscus anchored only to the small particles. The regime (i) occurs in the flooded wicks and leads to a low capillary pressure, whereas regime (iii) leads to the maximum capillary pressure in the bimodal bilayer wick. Regime (ii) corresponds to the meniscus jump, a discontinuity in the capillary pressure curve observed in [100, 95].

The SE simulations are repeated for the bimodal bilayer wick with the larger particles occupying the vacancies. The predicted $p_{c,max} = 2.92\,\text{kPa}$ shows the bilayer wick slightly compensates for the defect capillary pressure reduction. In the case of vacancies in the second layer, its functionality is nullified: if the vacancies in the first and second layers align, the same $p_{c,max} = 2.32\,\text{kPa}$ is observed; if the vacancies do not align, regime (iii) is observed and the $p_{c,max} = 2.92\,\text{kPa}$ is encountered elsewhere in the meniscus, where the first layer vacancy is located.

Figure 6.2 shows the SE snapshots for different evaporator layer wick configurations described above. The variations of the capillary pressure with the average liquid thickness scaled with the wick particle diameter $\langle \delta_l \rangle / d_e$ are shown graphically. The blue curves show the monolayer wick results and the orange curves show the bimodal bilayer wick. Square symbols show results for the ideal wick and the circle symbols show the results for the first-layer vacancy defect. The maximum capillary pressures for all cases are highlighted. The critical radius of curvature is reached at around

$\langle \delta_l \rangle / d_e = 0.45$ for the ideal monolayer wick and $\langle \delta_l \rangle / d_e = 0.5$ for the other wicks.
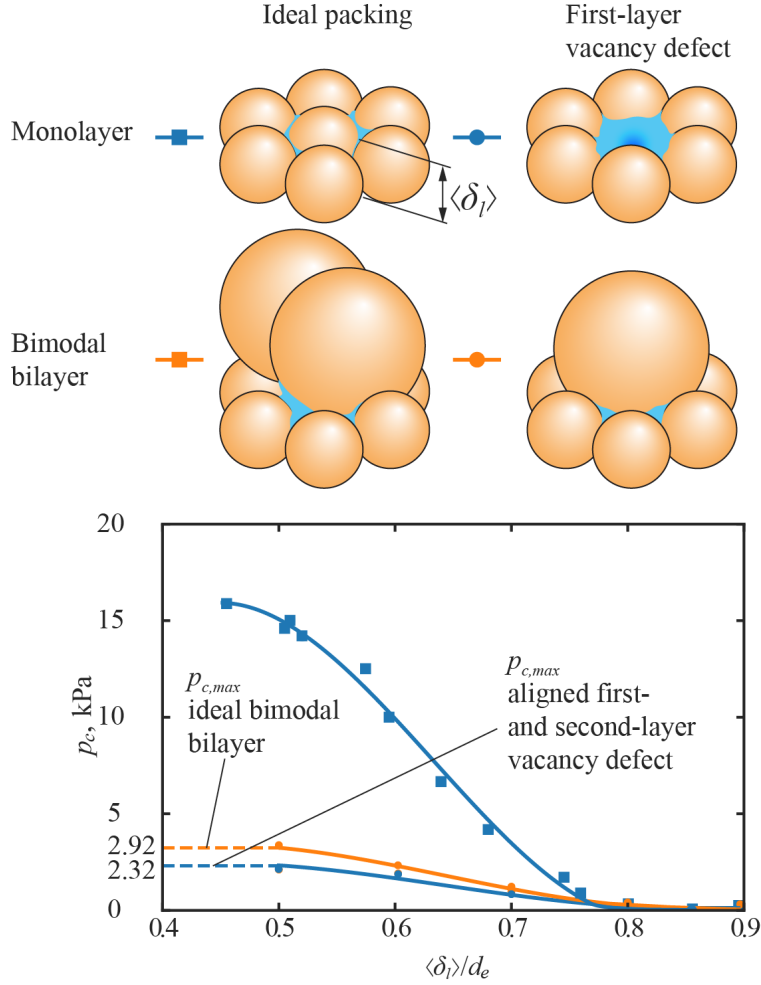
Figure 6.2: Snapshots of different evaporator layer wicks from SE. Variations of maximum capillary pressure $p_{c,max}$ with the average liquid thickness $\langle \delta_l \rangle$ scaled with the particle diameter d_e.

6.1.2 Permeability

The meniscus topology predicted by the SE simulation is exported for each capillary pressure p_c and the corresponding average liquid meniscus thickness $\langle \delta_l \rangle$. The meniscus topology files are loaded into Ansys Fluent [109] and the volume mesh of the liquid meniscus is created. The evaporator wick effective permeability is calculated from Eq. (5.9). The pressure gradient dp/dx is prescribed and the 3-D continuity and momentum conservation equations are solved and the average velocity is calculated to find the effective permeability. The no-slip boundary condition

is used at the interface between the liquid and the copper substrate and the liquid and the copper particles. A free shear condition is used at the liquid meniscus.

Figure 6.3 shows the variations of the evaporator wick effective permeability K_e in unit of Darcy (μm^2) with respect to the average liquid thickness scaled with the wick smaller particle diameter $\langle \delta_l \rangle / d_e$. The snapshots of the CFD mesh showing the liquid meniscus domain and the copper particles are also shown. The blue curves show the monolayer wick results and the orange curves are for the bimodal bilayer wick. The square symbols show results for the ideal packing wick and the circle symbols show the results for the first-layer vacancy defect. The numerical results show the monolayer wick with vacancy defect has the highest average permeability of $K_e = 4.7\,\mu m^2$, followed by the bimodal bilayer wick with first-layer vacancy having $K_e = 4.5\,\mu m^2$. Although the two effective permeabilities are comparable, the bimodal bilayer wick larger maximum capillary pressure overcompensates the discrepancy, making it the option capable of reaching a higher $q_{CHF,c\text{-}v}$.
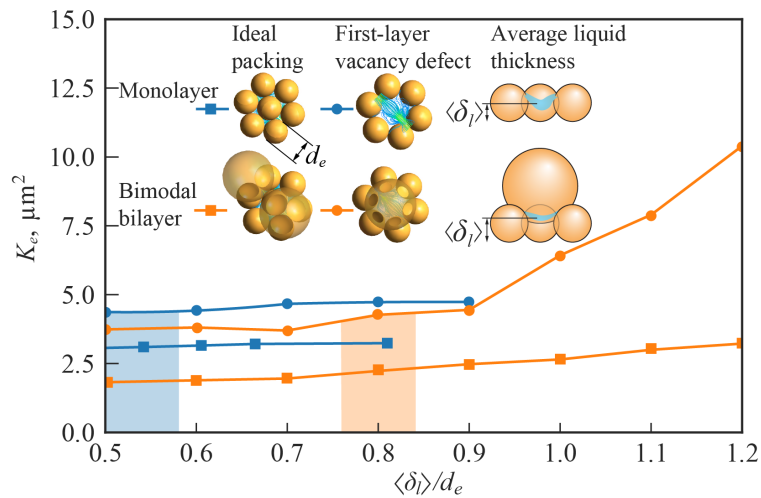
Figure 6.3: Variations of permeability with scaled (using the smaller particle diameter $d_e = 50\,\mu m$) averaged liquid thickness for the monolayer and bimodal bilayer with ideal packing and vacancy defect in the first layer. The bilayer allows for larger liquid thickness and larger permeability.

6.1.3 Thermal Conductivity

The mechanism for effective thermal conductivity and reduced conduction path is presented in Section 5.2.4. Here, the SE liquid meniscus topology is once again exported. It is then loaded into the Star-CCM+ [110] code using symmetry (1/12th geometry) with mesh size of $0.02d_e$. The boundary conditions are prescribed temperature T_s at the base of the particle and the liquid, prescribed temperature T_{lg} on the meniscus, and adiabatic surface elsewhere. The solid-liquid interfacial coupling uses the conjugate heat transfer. The bulk effective thermal conductivity from the correlation in [108] is also shown. The effective thermal conductivity is higher at lower capillary pressures (larger average meniscus thickness), and the heat flows mainly within the particle. The monolayer effective thermal conductivity is about ten folds larger than that of liquid water, greatly increasing the thermal conductance to $0.25\,\mathrm{kW/m^2}$-K. Thermal conductance based on the experimental results from the flow-boiling tests described in Chapter 9 are discussed in Chapter 10.
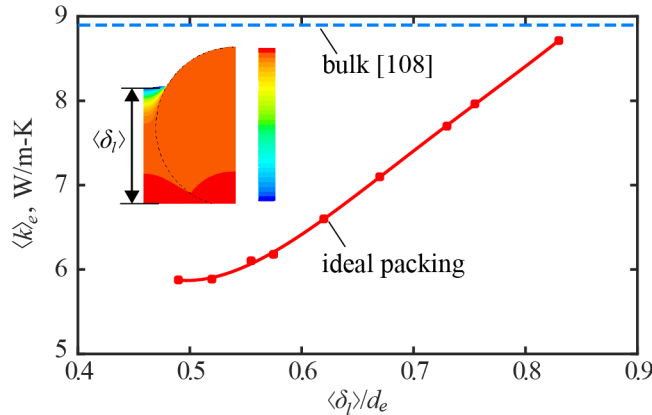
Figure 6.4: Variations of the effective thermal conductivity with the average meniscus thickness scaled by the particle diameter $d_e = 50$ μm. Snapshot of temperature distribution in the particle and liquid are shown in the detail with the copper-water interface marked with a dashed line.

6.2 Capillary Network Model

In the FBCW, the liquid supply to the evaporator wick passes through the posts. These liquid transport arteries are regularly spaced to minimize the distance travelled by the fluid particle in

the evaporator wick, minimizing the viscous pressure drop. For that reason, the evaporator wick unit cell is centered around the post with dimensions $(D_p + \Delta_{p,x}) \times (D_p + W_{per})$, as illustrated in Figure 6.5. The equivalent radial unit cell with equivalent diameter L'_p given by Eq. (4.3) is also shown. This transformation reduces the problem geometry from 2-D rectangular to 1-D radial.
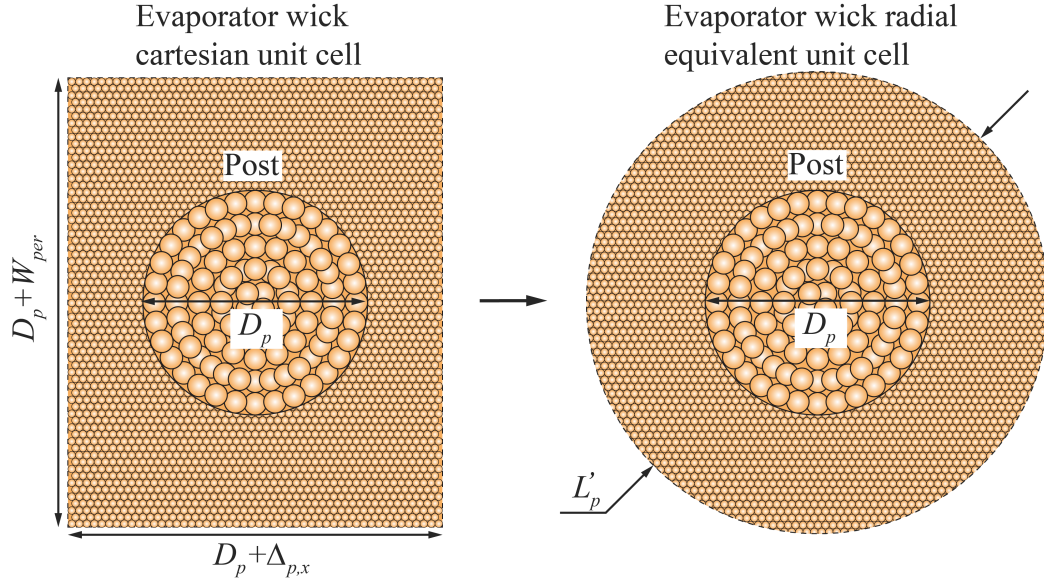
Figure 6.5: Evaporator wick rectangular unit cell centered around the post with diameter D_p shown on the left. The equivalent radial unit cell with diameter L'_p is shown on the right.

In order to calculate the pressure drop in the evaporator wick, a 1-D capillary network transport model is used. The nodal velocity distribution in the evaporator wick can be found by performing a mass flow rate balance around the node

$$\dot{M}_{l,i+1} - \dot{M}_{l,i} = \dot{M}_{lg}, \tag{6.1}$$

where i is the node index ranging from $i = 0$ at $r = L'_p/2$ to $i = N$ at $r = D_p/2$, and the source term is due to the meniscus evaporation, written as

$$\dot{M}_{lg} = \frac{q A_{\Delta r}}{\Delta h_{lg}}, \tag{6.2}$$

where q is the heat flux, assumed to be uniform, and $A_{\Delta r} = \pi(r_i^2 - r_{i+1}^2)$ is the annular area. The

mass flow rate term can be written as

$$\dot{M}_{l,i} = \rho_l u_{l,i} A_{r,i} = \rho_l u_{l,i} 2\pi r_i \langle \delta_l \rangle_i, \tag{6.3}$$

where $A_{r,i} = 2\pi r_i \langle \delta_l \rangle_i$ is the flow cross-section area at face i. Using the definition from Eqs. (6.2) and (6.3), Eq. (6.1) can be rewritten as

$$\rho_l u_{l,i+1} 2\pi r_{i+1} \langle \delta_l \rangle_{i+1} - \rho_l u_{l,i} 2\pi r_i \langle \delta_l \rangle_i = \frac{q}{\Delta h_{lg}} \pi (r_i^2 - r_{i+1}^2), \tag{6.4}$$

rearranging the terms, the velocity at face $i + 1$ can be found as

$$u_{l,i+1} = \frac{q}{\rho_l \Delta h_{lg}} \frac{(r_i^2 - r_{i+1}^2)}{2 r_{i+1} \langle \delta_l \rangle_{i+1}} + \frac{r_i \langle \delta_l \rangle_i}{r_{i+1} \langle \delta_l \rangle_{i+1}} u_{l,i}. \tag{6.5}$$

The velocity boundary condition at $i = 0$ is $u_{l,i} = 0$ since $r_i = L'_p/2$ is the edge of the unit cell. The pressure reference is placed at $r_i = L'_p/2$, $p_{l,i} = 0$. Figure 6.6 schematically illustrates the nodal network model, spanning the region from $D_p/2$ to $L'_p/2$.
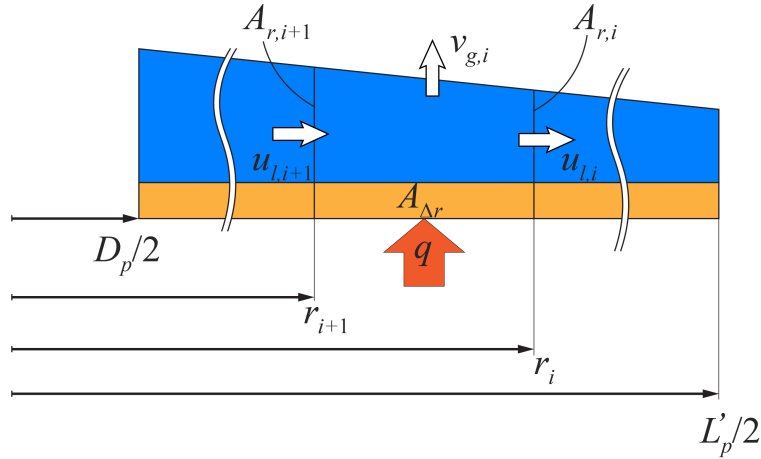
Figure 6.6: Schematic representation of the evaporator wick transport network model. The network model considers the radial equivalent unit cell. The orange region marks the copper substrate and the blue region is the liquid.

The nodal pressure distribution is found from Eq. (5.6),

$$p_{i+1} = p_i + \frac{\mu_l \langle u_{l,i} \rangle (r_i - r_{i+1})}{K_{e,i}}, \tag{6.6}$$

where the node velocity is $\langle u_{l,i} \rangle = (u_{l,i} + u_{l,i+1})/2$. The meniscus thickness $\langle \delta_l \rangle_i$ is related to the capillary pressure, and it can be found by performing a data regression on the SE simulation data shown in Figure 6.2. Similarly, the evaporator wick local permeability and thermal conductivity are found after performing the data regression on the SE simulation meniscus topology data shown in Figures 6.3 and 6.4. The overall pressure drop in the evaporator wick is then

$$\Delta p_e = p_{i=N} - p_{i=0}. \tag{6.7}$$

Both the canopy and the post viscous pressure drops are calculated and included into the network model with Eq. (5.6). The respective filtration velocities are calculated using Eqs. (5.18) and (5.19). The escaping vapor inertial pressure drop is also included using Eqs. (5.13) and (5.20). All pressure drops are combined and compared to the maximum capillary pressure, Eq. (4.1), to calculate the numerical capillary-viscous limit $q_{CHF,c\text{-}v}$.

The network model pressure drop results are compared with 3-D CFD results for the unit cell, for heat flux $q = 5\,\mathrm{MW/m^2}$. In Ansys Fluent [109], the mass and momentum conservation equations are solved. The porous media is represented in each component by the source term

$$S_i = - \left(\frac{\mu}{K} u_i + C \frac{\rho |u|}{2} u_i \right), \tag{6.8}$$

where the $C = 1.8(1 - \epsilon)/(\epsilon^3 d_p)$ is the inertial resistance coefficient. This source term includes the inertial contribution in the Forchheimer regime, Eq. (5.7).

The simulations require an exceptionally fine mesh in the evaporator due to its small thickness (order of $100\,\mu\mathrm{m}$). The pressure distribution is shown in Figure 6.7, with a snapshot indicating the pressure and velocity distributions and streamlines, for a unit cell centered around the post. The CFD wick unit cell is 1/6th of the FBCW perforation unit cell $[(D_p + \Delta_{p,x}) \times (D_p + W_{per}) = 2 \times 3$ mm^2, $H_{ca} = 0.75\,\mathrm{mm}$ thick canopy and $H_p = 1.3\,\mathrm{mm}$ long post with $D_p = 1.5\,\mathrm{mm}$]. The CFD

pressure drop results agree well with the resistance network model results. The evaporator pressure drop component dominates (attributable to the lower permeability and liquid flow cross-section area) with $\Delta p_e = 1619\,\mathrm{Pa}$, followed by the post, $\Delta p_p = 263\,\mathrm{Pa}$, and canopy, $\Delta p_{ca} = 95\,\mathrm{Pa}$.
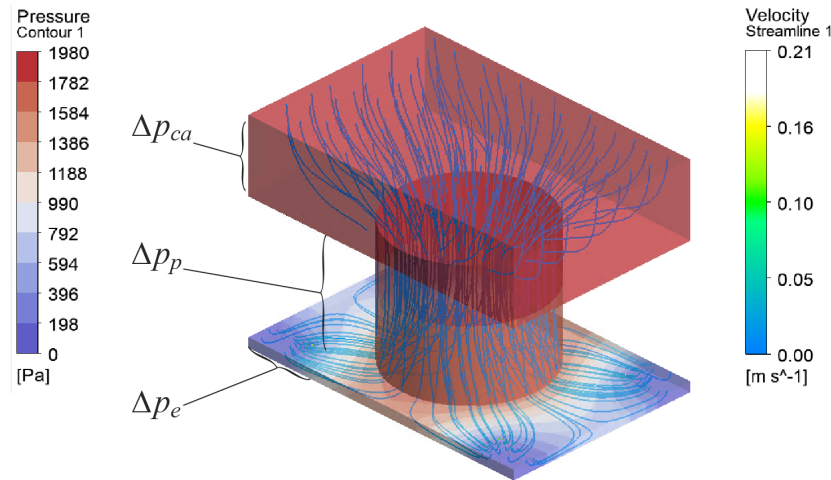
Figure 6.7: Snapshot of wick unit cell computational fluid dynamics simulation indicating pressure contour and velocity streamlines inside the wick unit cell for $q = 5\,\mathrm{MW/m^2}$. Canopy, posts, and evaporator wick pressure drop components are highlighted.
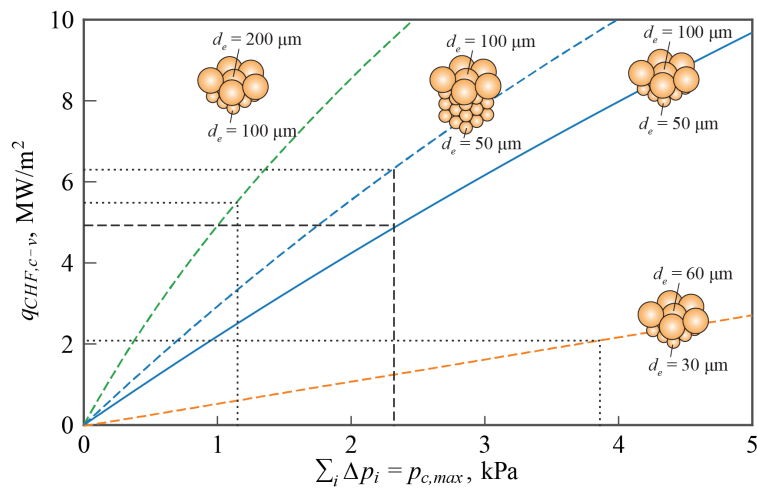
Figure 6.8: Variations of the capillary-viscous CHF with the total pressure drop, for four different evaporator wick designs which affect the maximum capillary pressure. Results for saturated water at one atm.

Figure 6.8 shows the variations of the capillary-viscous CHF with the overall pressure drop (maximum capillary pressure) for different multilayer wick designs. Results for the blue curve have

been experimentally verified in [89] for a bimodal bilayer wick with particles sized $d_e = 50$ and $100\,\mu$m with a $p_{c,max} = 2.32$ kPa and the current capillary-viscous CHF is $q_{CHF,c\text{-}v} = 4.6$ MW/m². The orange and green lines are design variations corresponding to $d_e = 30$ and $60\,\mu$m and $d_e = 100$ and $200\,\mu$m. The wick with smaller particles ($p_{c,max} = 3.86$ kPa) results in a CHF reduction to $q_{CHF,c\text{-}v} = 2.1$ MW/m², while the large particles wick provides an enhancement despite the lower $p_{c,max}$, i.e., $q_{CHF,c\text{-}v} = 5.5$ MW/m² ($p_{c,max} = 1.15$ kPa). A large enhancement is obtained when using a thicker evaporator layer (3 layers $d_e = 50\,\mu$m and one layer $d_e = 100\,\mu$m): $q_{CHF,c\text{-}v} = 6.3$ MW/m², however, this will decrease the thermal conductance.

Under low heat flux, the meniscus is nearly planar and liquid nearly fill the evaporator wick. So, the average meniscus thickness is larger for the the thick evaporator wick, design 4, which is made of 3 small-particle layers ($d_p = 50\,\mu$m) and a single-layer secondary wick ($d_p = 100\,\mu$m). Using the average superheat found from the network model, the thermal conductance at the capillary-viscous limit are calculated. The best CHF and thermal conductance enhancement can be found by defining a dimensionless figure of merit Z_m which compares the CHF enhancement over the plain surface and the thermal conductance with a pure copper substrate

$$Z_m = \frac{q_{CHF,c\text{-}v}}{q_{CHF,Z}} \frac{(G/A)_{FBCW}}{(G/A)_{Cu}}, \tag{6.9}$$

where $q_{CHF,c\text{-}v}$ is the capillary-viscous limit, $q_{CHF,Z} = 1.1$ MW/m² (saturated water at one atm) is the Zuber limit for plain-surface pool boiling, $(G/A)_{FBCW}$ is the thermal conductance for each of the four proposed bimodal multilayer evaporator wick designs, and $(G/A)_{Cu} = k_{Cu}/l_{Cu} = 0.4$ MW/m²-K is the thermal conductance for a $l_{Cu} = 1$ mm thick copper wall. Design 1 presents the best figure of merit $Z_{m,1} = 2.84$, followed by design 2 with $Z_{m,2} = 2$ and design 3 with $Z_{m,3} = 1.88$. Design 4 is the worst with $Z_{m,4} = 1.14$.

The corresponding pressure drops from the network model for the different bimodal multilayer evaporator wick designs shown in Figure 6.8 are listed in Table 6.1. Further details are available in [89].

Table 6.1: Pressure drop components for the different evaporator wick designs. The corresponding $q_{CHF,c\text{-}v}$ and G/A are also listed.

Design	d_e, μm	$q_{CHF,c\text{-}v}$, MW/m²	G/A, MW/m²-K
1	50,100	5.0	0.25
2	30,60	2.1	0.42
3	100,200	5.5	0.15
4	50(3),100	6.3	0.08

Design	Δp_e, kPa	Δp_p, kPa	Δp_{ca}, kPa
1	1.93	0.15	0.04
2	3.67	0.08	0.03
3	0.58	0.22	0.05
4	1.63	0.29	0.06

Design	$\Delta p_{per,g}$, kPa	$\sum \Delta p_i$, kPa	$p_{c,max}$, kPa
1	0.20	2.32	2.32
2	0.08	3.86	3.86
3	0.28	1.14	1.14
4	0.34	2.32	2.32

6.3 Summary

The predicted wick effective properties were presented as a function of the average meniscus thickness in the evaporator wick. Different evaporator wick designs, namely a monolayer evaporator and a bimodal bilayer evaporator, were presented for the ideal and defective wick cases. The wick liquid flow transport network model for predicting the nodal pressure and velocity distributions in the evaporator wick was derived and used to determine the overall evaporator wick viscous pressure drop and capillary-viscous critical heat flux $q_{CHF,c\text{-}v}$. The 1-D liquid flow network model results were compared with the 3-D CFD fluid flow results and good agreement was found.

CHAPTER 7

Beyond the Wavelength Modulation Regime:

Proposed Geometric Modulation Regime

In this chapter, a novel regime of CHF modulation is proposed based on the geometry and spatial arrangement of vapor sites. Further CHF enhancements achieved through geometric-confinement stabilizing of the surface liquid track is also discussed.

7.1 Vapor-Site Geometric-Modulation Regime

In the Wavelength Modulation Regime, Section 2.3, the effects of the liquid velocity on the postponement of the boiling crisis and enhancing the hydrodynamic CHF $q_{CHF,h}$ were discussed. The leading-edge surface liquid track dryout model expands on the Zuber unit-cell theory for the pool-boiling CHF [22] by including the effects of inertial and viscous forces on the axial liquid supply to the surface. This modulation is limited to the range of velocities given by Eqs. (2.25) and (2.26) $u_{l,o,min} = 6\,\mathrm{mm/s} \leq u_{l,o} \leq u_{l,o,max} = 5\,\mathrm{m/s}$, corresponding to the Zuber pool-boiling limit and the capillary limit ($\lambda_c = l_c$) for saturated water (one atm), and the CHF enhancement is limited to $q_{CHF,h} = 3.3\,\mathrm{MW/m^2}$ at $u_{l,o,max}$, as shows Figure 2.7.

Here, the effects of the geometry and spatial arrangement of the vapor columns emanating from the surface on the CHF enhancement are considered. In the Zuber theory [22], these vapor sites are assumed to be circular and in a periodic square, staggered arrangement, as shown in Figure 2.3. In flow boiling, the surface liquid track meanders around these vapor sites, which can break its

streamwise continuous surface coverage. As discussed in Chapters 2 and 3, the liquid supply may be exclusively from this axial flow in flow boiling, so the alignment of these vapor sites can be extremely relevant. The staggered configuration shown in Figure 7.1(a) leads to a reduced path $w_{l,o}$ between vapor sites for the surface liquid track $w_{l,o} = (2^{1/2} - 1)\lambda_c/2$. By aligning the vapor sites, as in Figure 7.1(b), the liquid path increases to $w_{l,o} = \lambda_c/2$. This alignment of the liquid flow path and the arrangement of vapor sites is expected to prevent dryout, i.e., requiring additional vapor-flow shear to fully destabilize the leading-edge surface liquid track.

(a) Circular Vapor Inlets Staggered Arrangement

(b) Circular Vapor Inlets Inline Arrangement

(c) Rectangular Vapor Inlets Inline Arrangement
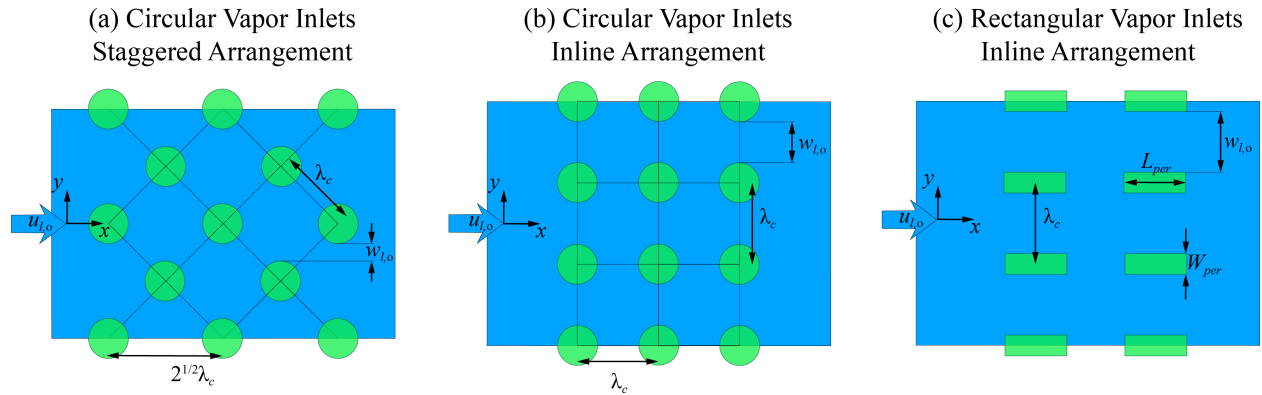
Figure 7.1: Schematic representation of vapor site arrangements: circular vapor inlets with staggered and inline arrangements, and rectangular vapor inlets with inline arrangements (perforated canopy). Liquid flow path for the different arrangements is also shown.

The circular vapor sites geometry can also be modified. Figure 7.1(c) proposes rectangular perforations with an aspect ratio L_{per}:W_{per}, the liquid track available is $w_{l,o} = \lambda_c - W_{per}$. The high aspect ratio helps direct the vapor downstream, preventing its lateral expansion and limiting vapor shearing of the liquid track.

In order to verify these, the CFD simulations described in Chapter 3 is repeated for the different vapor site configurations (geometry and arrangement) for $q = 1.75\,\mathrm{MW/m^2}$ and $u_{l,o} = 0.25\,\mathrm{m/s}$, a condition for which dryout was observed for the circular, staggered arrangement.

Figure 7.2(a) renders CFD snapshots of these vapor escape sites (also referred to as surface perforations), following the Zuber unit-cell model, arranged in staggered and inline packing. Figure 7.2(b) shows the time variations of the dimensionless surface liquid track width $\langle w_l^* \rangle$, Eq. (3.33), for up to four times the fluid transit time $t_o = u_{l,o}/\lambda_c$, Eq. (3.34). Dryout is clearly

observed for the staggered arrangement. The inline arrangement presents an increase in CHF over the staggered, but less so than the inline rectangular vapor sites. Although the inline circular vapor site arrangement does initially establish a clear path for the liquid flow, this path encounters the hindering lateral expansion of vapor, which counters any possible CHF enhancements at this velocity.

The rectangular vapor site geometry (will be referred to perforation in the porous metasurface discussions) was originally proposed in [62, 63, 89]. With this geometry, the neighboring vapor slots do not coalesce immediately close to the surface ($z = 0$), due to prevention of the lateral expansion of emerging vapor streams. This rectangular perforation geometry is preferred over square-aligned circular perforations because it allows for the formation of a continuous liquid track in the region between perforations.
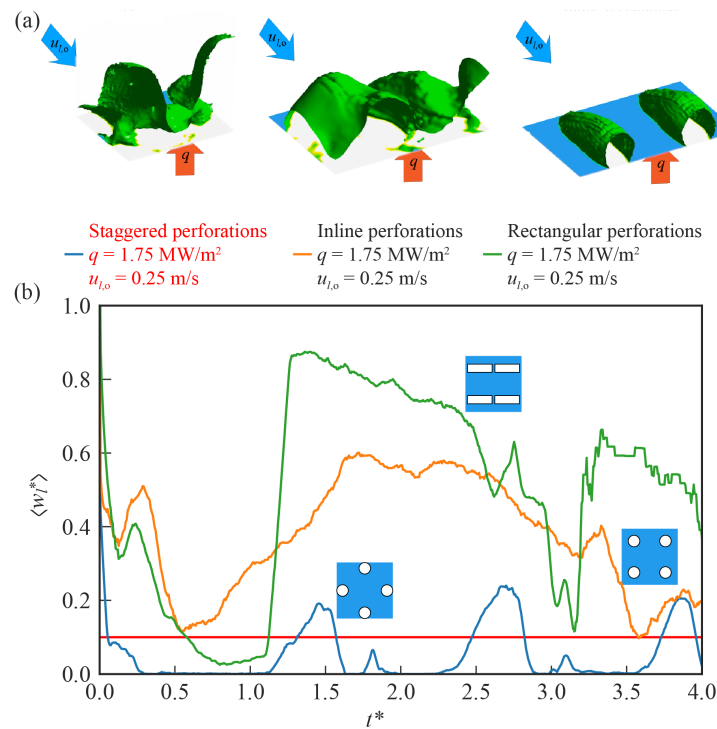
Figure 7.2: (a) Schematic representation of vapor sites and surface liquid track snapshots in hexagonal arrangement, aligned with the inlet flow direction, and with rectangular perforations. Red label indicates dryout. The full video is available in the supplementary materials. (b) Time variations of liquid track width at different axial locations for $q = 1.75 \, \mathrm{MW/m^2}$, $u_{l,o} = 0.25 \, \mathrm{m/s}$ for saturated water (one atm).

75

7.2   Vapor Shearing of Liquid Track

For the conditions of Figure 7.2, in the case of inline rectangular vapor inlet arrangement, no dryout is observed and the leading-edge surface liquid track, represented by the dimensionless liquid track width $\langle w_l^* \rangle$. Further downstream, the surface liquid track continues underneath the flowing vapor. This flow configuration can be approximated by the case of two uniform streams in relative horizontal motion separated by a horizontal interface [49], as illustrates Figure 7.3(a). This is the Kelvin-Helmholtz interfacial instability problem.
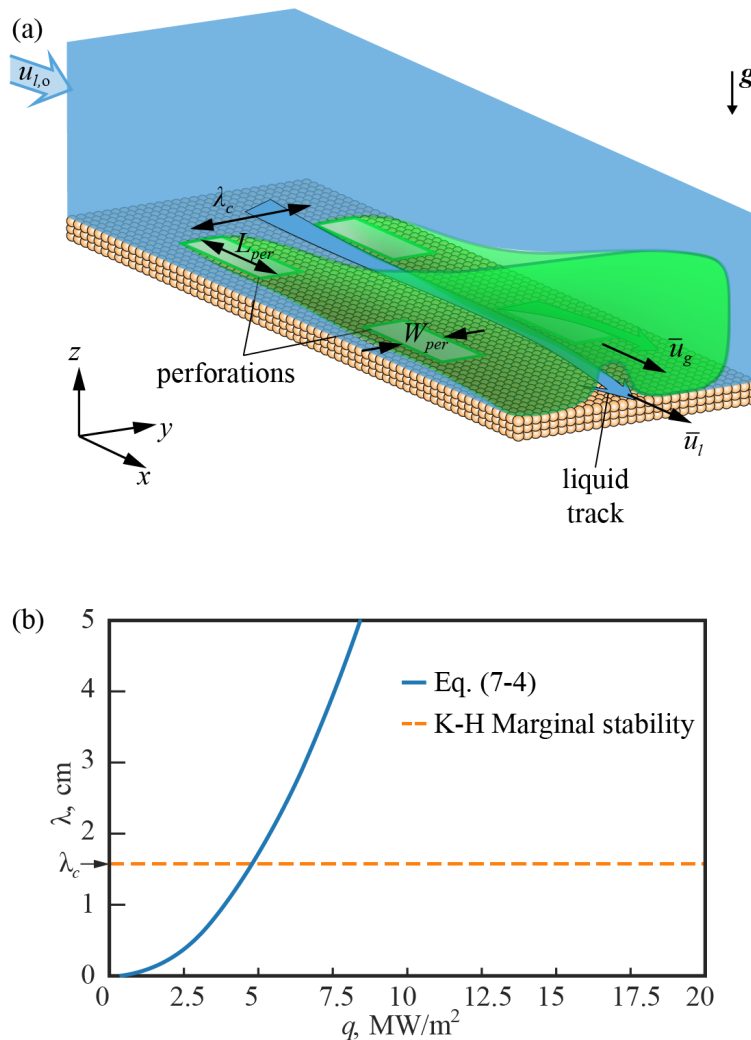
Figure 7.3: (a) Rectangular vapor slots aligned with the flow direction. (b) Variations of interfacial vapor wavelength with Kelvin-Helmholtz CHF for $\lambda_c = 4.5\,\mathrm{mm}$. The axial K-H marginal stability is highlighted.

Since the lighter fluid is on top, this condition is stable, but a critical relative velocity is found for this flow configuration. It can be calculated according to [49]

$$|u_g - u_l| = \left\{ \frac{2}{\rho_g^* \rho_l^*} \left[\frac{\sigma g (\rho_l^* - \rho_g^*)}{\rho_l^* + \rho_g^*} \right]^{1/2} \right\}^{1/2}, \tag{7.1}$$

where $\rho_f^* = \rho_f/(\rho_l + \rho_g)$ and for saturated water (one atm) with properties in Table 2.1 $u_g - u_l = 9\,\mathrm{m/s}$. From Eq. (7.1), we can infer the acceleration of vapor will eventually trigger the K-H instability. The axial interfacial wavelength corresponding to the critical relative velocity is found as [49]

$$\lambda_{KH} = \frac{\pi (u_g - u_l)^2}{g} \frac{\rho_l^* \rho_g^*}{(\rho_l - \rho_g)}. \tag{7.2}$$

For the liquid-vapor saturated water (one atm) interfaces, using the critical velocity from Eq. (7.1), we find $\lambda_{KH} = 15.7\,\mathrm{mm}$. The relative velocity depends on the heat flux, so a functional relationship of type $q_{CHF,h} \approx \lambda_{KH}^{1/2}$ is found by rewriting the vapor velocity as a function of the heat flux

$$u_g = \frac{q A_{evap}}{\rho_g \Delta h_{lg} \lambda_c^2}, \tag{7.3}$$

where λ_c is the perforation characteristic wavelength. At the critical relative velocity given in Eq. (7.1), the heat flux corresponds to the hydrodynamic CHF limit $q_{CHF,h}$. Combining and rearranging Eqs. (7.1) to (7.3), we find

$$q_{CHF,h} = \left\{ \left[\frac{\lambda_{KH}}{\pi} \frac{(\rho_l^* - \rho_g^*)}{\rho_g^* \rho_l^*} g \right]^{1/2} + u_l \right\} \frac{\rho_g \Delta h_{lg}}{A_{evap}} \lambda_c^2. \tag{7.4}$$

For the given $\lambda_x = 15.7\,\mathrm{mm}$, the maximum heat flux for marginal stability is $q = 5\,\mathrm{MW/m^2}$. The relationship from Eq. (7.4) is graphically shown in Figure 7.3(b) for constant $\lambda_c = 4.5\,\mathrm{mm}$ (used in the FBCW).

7.3 Geometric-Confined Liquid Track: Confined-Geometric Modulation Regime

At high heat flux, the rectangular perforation geometry and the liquid inertia may not be enough to prevent the vapor lateral expansion destabilizing the liquid track. One natural idea is to further enhance the geometric confinement effects described in Section 7.2 by further delaying the merging of neighboring vapor streams.

The addition of levees is schematically shown in Figure 7.4(a). Two snapshots at locations above the surface, $z = 0.25$ and 2 mm, show the vapor penetration is considerably reduced in the intralevee spacings (i.e., aqueducts), it was first proposed in [62]. The liquid track is shielded from the expanding vapor since a significantly smaller fraction of the vapor diverts towards the liquid track to disturb it. A secondary effect of the addition of levees is the liquid anchoring, due to the no-slip effect, the levees anchor the liquid, further stabilizing it and requiring additional shearing from the vapor flow to disrupt it. The CFD results show the addition of levees is capable of suppressing the onset of the K-H instability since the vapor has to penetrate further into the intralevee subchannel, thus raising the hydrodynamic CHF to over $15\,\mathrm{MW/m^2}$ [62].

Figure 7.4(b) shows the time variation of the dimensionless area of liquid in the intralevee channel (spanning $-1.25\,\mathrm{mm} \leq y \leq 1.25\,\mathrm{mm}$ by $0\,\mathrm{mm} \leq z \leq 3\,\mathrm{mm}$) at axial location $x = 16\,\mathrm{mm}$ for different heat flux ($q = 5$, 10 and $15\,\mathrm{MW/m^2}$), for $u_{lo} = 5\,\mathrm{m/s}$. The dimensionless area is calculated according to

$$\langle A_l^* \rangle = \frac{1}{\Delta x} \sum_i^{\Delta x} \frac{1}{w_l H_l} \int_0^{w_l} \int_0^{H_l} f\,dz\,dy, \quad \begin{cases} f = 0, & \alpha \geq 0.5 \\ f = 1, & \alpha < 0.5 \end{cases}. \tag{7.5}$$

No dryout is observed even though the heat flux was increased to $15\,\mathrm{MW/m^2}$ at the same inlet velocity of $u_{l,o} = 0.5\,\mathrm{m/s}$. The higher intensity turbulence is still stemming from the interface as discussed in Section 3.3, but moved further away from the liquid track, at the top portion of the channel, where the high-velocity vapor deflects the liquid. As mentioned earlier, inside the
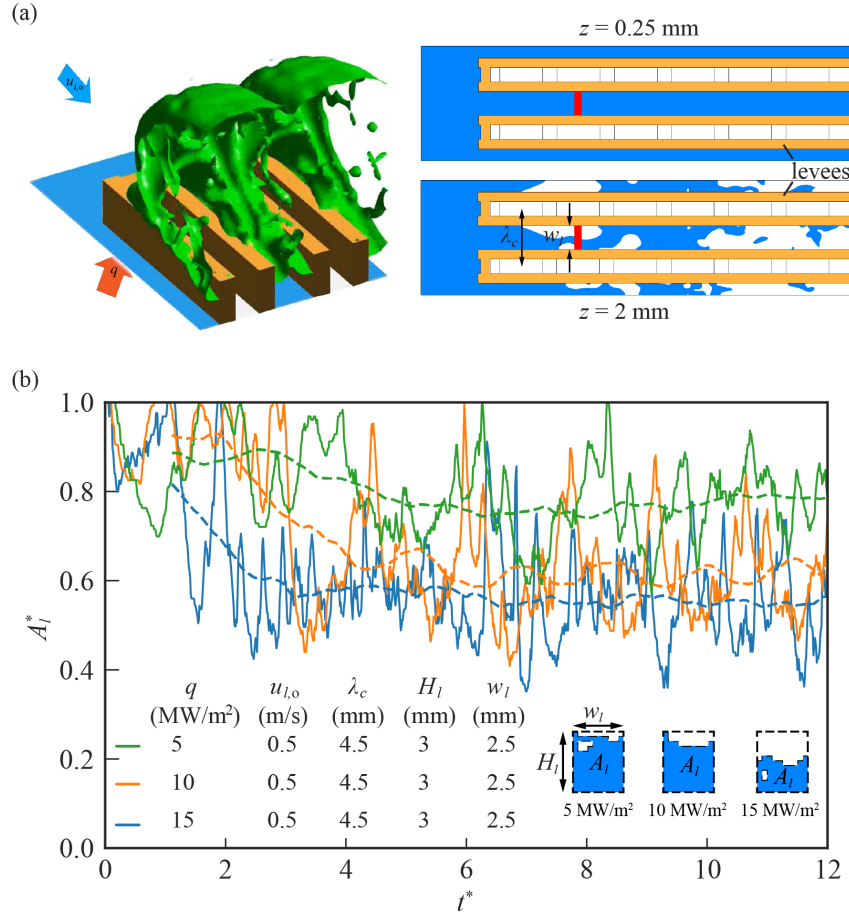
Figure 7.4: (a) Snapshot of C-GMR video and top-view of phase distribution in the axial planes at elevations $z = 0.25$ and $2\,\text{mm}$ for metasurface with levees. The full video is available in the supplementary materials. (b) Time variation of liquid phase yz area fraction at $x = 16\,\text{mm}$. $q = 5$, 10 and $15\,\text{MW/m}^2$, $u_{l,o} = 0.5\,\text{m/s}$ for saturated water (one atm).

intralevee subchannel, the vapor is at a much lower velocity, so the flow is less turbulent, and the K-H stability is preserved.

The geometric confinement has a stabilizing effect on the liquid track [111], this can be assured for a confinement number $\text{Co} = l_c/D_h < 1$, where l_c is the capillary length and D_h is the intralevee channel hydraulic diameter [112]. This is illustrated in Figure 7.5(a) and (b), with and without levees. Addition of the levees to the side of the perforations allows for the liquid confinement between them, shielding the liquid from the lateral vapor-flow shearing. The walls anchor the liquid (no velocity slip condition), requiring additional shear from the vapor flow to disturb the

79

liquid track. Both the liquid and vapor phases experience the same pressure gradient within the aqueduct, so there is a measure of local mechanical equilibrium between the phases.
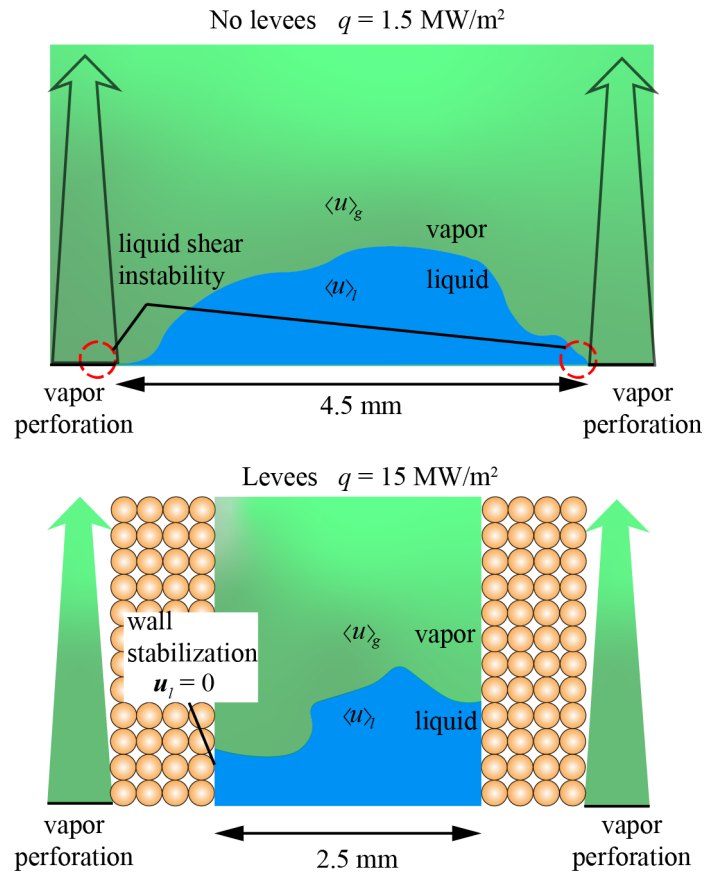
Figure 7.5: Liquid track topology and the surrounding vapor at the channel exit. (a) The case on no levees leads to smaller CHF due to lateral spreading of the vapor exiting the perforations, and here the results are for $q = 1.5\,\mathrm{MW/m^2}$. (b) With the levees, the vapor diversion and the levee wall-stabilize the liquid track. Saturated water (one atm), $u_{l,\mathrm{o}} = 0.5\,\mathrm{m/s}$.

The geometric modulation regime allows for larger CHF enhancement than the wavelength modulation regime by altering the arrangement of vapor sites. The hydrodynamic CHF enhancement is predicted to be $q_{CHF,h} = 5\,\mathrm{MW/m^2}$ as shows Figure 7.3(c) for $u_{l.\mathrm{o}} = 0.5\,\mathrm{m/s}$ and $\lambda_c = 4.5\,\mathrm{mm}$, according to Eq. (7.4). This limit can be surpassed with the addition of levees creating a new modulation regime that uses the geometry-confinement effect to anchor and protect the surface-liquid track from the vapor-flow shear destabilization. The surface-liquid track protection will be verified using CFD simulations up to $q = 15\,\mathrm{MW/m^2}$ in the confined-geometic modulation

regime in Chapter 8.

7.4   Summary

The Geometry Modulation Regime was introduced and its mechanism of CHF enhancement by rearranging the vapor sites was explained. An additional modulation regime using the geometry confinement effect was proposed to further enhance the hydrodynamic CHF through the addition of levees to the side of the vapor sites (perforations). The vapor diversion by the levees offers extra protection to the liquid track from the lateral vapor shear, where the interfacial instability is due to the relative axial phasic velocities.

CHAPTER 8

Direct Numerical Simulation of the Geometric Modulation Regime

In this chapter, the DNS of the saturated flow boiling in the Geometric Modulation Regime is performed considering the perforated canopy shown in Figure 7.1(c). The analysis is extended to the Confined-Geometric Modulation Regime, where the levees are added to the side of the perforations in the canopy wick.

The CFD analysis discussed in this chapter employs the Reynolds-Averaged Navier-Stokes (RANS) equations. Using the perforated canopy and later with the addition of levees, the formation and stabilization of the leading-edge surface liquid track is secured. So, the fate of the escaping and accumulating vapor and its interaction with the liquid track and mixing with the liquid flow becomes the main focus. These interfacial interactions leading to K-H type instabilities are treated with the widely applied two-equation closure model of turbulence [113], as reported in the literature for similar flow conditions [114, 115, 116].

Although the analyses discussed in this chapter were performed prior to the ones discussed in Section 3.3, the good agreement found between the numerical and the experimental results in Chapter 10 indicates the suitability and accuracy of this model.

8.1 Treatment of Turbulence: Two-Equation k–ε Model

In order to model flow turbulence, a Reynolds decomposition is performed [74]. The Reynolds averaging is a type of ensemble averaging suitable for flows that decay in time [117]. The velocity vector is decomposed into its mean and fluctuation components $u_f = \overline{u}_f + u'_f$, where the mean velocity $\overline{u}_f$ can vary with time. The Reynolds averaging process introduces the Reynolds stress tensor to the momentum equation, an unknown which requires modeling to fully close the problem [118]. The Reynolds-Averaged Navier-Stokes (RANS) equations are written as [119]

$$\frac{\partial \rho_f}{\partial t} + \frac{\partial}{\partial x_i} \left(\rho_f \overline{u}_{f,i} \right) = 0, \tag{8.1}$$

$$\frac{\partial}{\partial t} \left(\rho_f \overline{u}_{f,i} \right) + \frac{\partial}{\partial x_i} \left(\rho_f \overline{u}_{f,i} \overline{u}_{f,j} \right) = -\frac{\partial \overline{p}}{\partial x_i} + \frac{\partial}{\partial x_j} \left[\mu_f \left(\frac{\partial \overline{u}_{f,i}}{\partial x_j} + \frac{\partial \overline{u}_{f,j}}{\partial x_i} - \frac{2}{3} \delta_{ij} \frac{\partial \overline{u}_{f,k}}{\partial x_k} \right) \right] + \\ \frac{\partial}{\partial x_j} \left(-\rho_f \overline{u'_{f,i} u'_{f,j}} \right) + f_{s,i}, \tag{8.2}$$

where $-\rho_f \overline{u'_{f,i} u'_{f,j}}$ are the Reynolds stresses. As mentioned earlier, these stresses require additional modeling for the complete closure of the problem. Different closure models have been proposed based on different assumptions regarding the turbulence length scale [117]. The two-equation k–ε model [120] introduces two additional conservation equations for the turbulent kinetic energy $\overline{E}_{f,t}$, defined as [74]

$$\overline{E}_{f,t} = \frac{1}{2} \left(\overline{u'^2_f} + \overline{v'^2_f} + \overline{w'^2_f} \right), \tag{8.3}$$

and the turbulence dissipation rate $\varepsilon_{f,t}$ defined as [74]

$$\varepsilon_{f,t} = \nu_f \overline{\frac{\partial u'_{f,i}}{\partial x_k} \frac{\partial u'_{f,j}}{\partial x_k}}. \tag{8.4}$$

Their transport equations are given as

83

$$\frac{\partial \left(\rho_f E_{f,t} \right)}{\partial t} + \frac{\partial \left(\rho_f \overline{u}_{f,i} E_{f,t} \right)}{\partial x_i} = -\rho_f \overline{u'_{f,i} u'_{f,j}} \frac{\partial \overline{u}_{f,i}}{\partial x_j} - \rho_f \varepsilon_{f,t} + \frac{\partial}{\partial x_j} \left[\left(\mu_f + \frac{\mu_{f,t}}{\sigma_1} \right) \frac{\partial E_{f,t}}{\partial x_j} \right], \quad (8.5)$$

$$\frac{\partial \left(\rho_f \varepsilon_{f,t} \right)}{\partial t} + \frac{\partial \left(\rho_f \overline{u}_{f,i} \varepsilon_{f,t} \right)}{\partial x_i} = -\rho_f \overline{u'_{f,i} u'_{f,j}} \frac{\partial \overline{u}_{f,i}}{\partial x_j} C_{1,\varepsilon} \frac{\varepsilon_{f,t}}{E_{f,t}} - C_{2,\varepsilon} \rho_f \frac{\varepsilon_{f,t}^2}{E_{f,t}} + \frac{\partial}{\partial x_j} \left[\left(\mu_f + \frac{\mu_{f,t}}{\sigma_2} \right) \frac{\partial \varepsilon_{f,t}}{\partial x_j} \right],$$
$$(8.6)$$

where $C_{1,\varepsilon} = 1.44$, $C_{2,\varepsilon} = 1.92$, $\sigma_1 = 1.0$ and $\sigma_2 = 1.3$ are constants adjusted based on experimental data. The Reynolds stress tensor, the correlation of fluctuation velocities, is calculated as

$$\overline{u'_{f,i} u'_{f,j}} = \frac{2}{3} E_{f,t} \delta_{ij} - \nu_{f,t} \left(\frac{\partial \overline{u}_{f,i}}{\partial x_j} + \frac{\partial \overline{u}_{f,j}}{\partial x_i} \right), \quad (8.7)$$

where $\nu_{f,t}$ is the eddy viscosity, calculated in the k-ε model as

$$\nu_{f,t} = \frac{C_\mu \overline{E}_{f,t}^2}{\varepsilon_{f,t}}, \quad (8.8)$$

where the coefficient C_μ is a function of the mean strain $\mathbf{S}$ and rotation $\mathbf{\Omega}$ rates in the realizable k–ε model [114].

The k–ε closure model assumes isotropy of turbulence, that is, all normal stresses are equal

$$\overline{\left(u'_f \right)^2} = \overline{\left(v'_f \right)^2} = \overline{\left(w'_f \right)^2}. \quad (8.9)$$

The unsteady form of the RANS equations with the two-equation k–ε closure model presented above relies on modeling of the Reynolds stresses to fully resolve the turbulence across the entire spectrum of wavelengths. Different turbulence treatments such as LES, discussed in Section 3.3, resolve large scale eddies while restricting modelling to small, subgrid scale eddies only. Improved accuracy is achieved with LES, but the use of unsteady RANS with an appropriate grid can provide

comparable results [121, 122].

8.1.1 Wall Treatment

A non-uniform structured mesh is employed to facilitate convergence. Size independence on the key parameters was discussed in Section 3.5. Near the walls, a different set of turbulence models is deployed to include the turbulence decay and the presence of the laminar sublayer. The so-called wall model. The two equation k–ε model utilizes a velocity scale based on the turbulent kinetic energy in the first node from the wall $E_{f,t,p}$. It is given as [120]

$$U^* = \frac{\overline{u}_{f,p} C_\mu^{1/4} E_{f,t,p}^{1/2}}{\tau_w/\rho_f},$$ (8.10)

where $\overline{u}_{f,p}$ is the velocity in the first node from the wall, C_μ is the coefficient given by Eq. (8.8) and τ_w is the wall shear stress. The dimensionless length perpendicular to the surface is

$$y^* = \frac{\rho_f C_\mu^{1/4} E_{f,t,p}^{1/2} y_p}{\mu_f},$$ (8.11)

where y_p is the distance from the first node to the wall. The relation between Eqs. (8.10) and (8.11) is called the law-of-the-wall, and it is given as

$$U^* = \frac{1}{\kappa_{\mathrm{vK}}} \ln\left(9.793 y^*\right),$$ (8.12)

where $\kappa_{\mathrm{vK}} = 0.4187$ is the von Karman constant. The expression from Eq. (8.12) is valid for $30 < y^* < 300$. The boundary condition for the turbulent kinetic energy imposed at the wall is

$$\frac{\partial E_{f,t}}{\partial x_n} = 0,$$ (8.13)

where x_n is the direction normal to the wall. The production and dissipation rates of turbulent kinetic energy in the volume adjacent to the wall are assumed to be equal. They are calculated as

$$P_{f,t,p} = -\rho_f \overline{u'_{f,i} u'_{f,j}} \frac{\partial \overline{u}_{f,i}}{\partial x_j} = \frac{\tau_w^2}{\kappa_{\mathrm{vK}} \rho_f E_{f,t,p}^{1/2} y_p}, \tag{8.14}$$

$$\varepsilon_{f,t,p} = \frac{C_\mu^{3/4} E_{f,t,p}^{3/2}}{\kappa_{\mathrm{vK}} y_p}. \tag{8.15}$$

Near the wall, Eq. (8.6) is not solved, and the dissipation rate of turbulent kinetic energy is calculated from Eq. (8.15) instead.

In the LES model, a similar approach is used, but the adopted distance from the wall y^+ is based on the wall shear

$$y^+ = \frac{\rho_f u_\tau y}{\mu_f}, \tag{8.16}$$

where the friction velocity u_τ is

$$u_\tau = \frac{\tau_w}{\rho_f}^{1/2}. \tag{8.17}$$

The velocity in the near-wall region is scaled according to

$$u_f^+ = \frac{\overline{u}_f}{u_\tau}. \tag{8.18}$$

In the viscous sublayer, also called laminar sublayer, the region where $y^+ < 5$, the viscous stresses dominate (low-Reynolds models). The law-of-the-wall in this region gives

$$u_f^+ = y^+, \tag{8.19}$$

a linear relation. For large y^+, $y^+ > 30$, the Reynolds shear stress dominate (high-Reynolds models) and Eq. (8.12) is used. This region is called the inertial sublayer or the log-layer. The region between the laminar sublayer and the log-layer, corresponding to $5 < y^+ < 30$ is called the buffer layer is difficult to model and in general should be avoided. These regions are illustrated in

Figure 8.1.
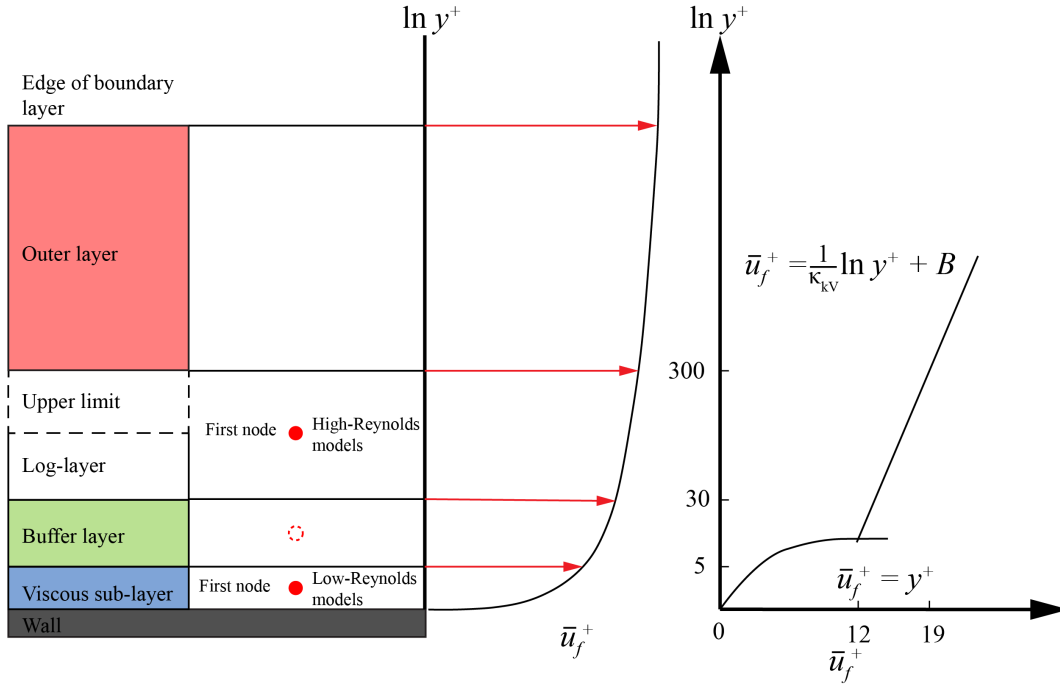
Figure 8.1: Schematic representation of the turbulent sublayers in the near wall region.

The Fluent solver [109] combines the linear and logarithmic relations to generate a solution for the buffer layer using the following expression [123]

$$u_f^+ = e^\Gamma u_{laminar}^+ + e^{1/\Gamma} u_{turbulent}^+,$$

(8.20)

where the blending function is [123]

$$\Gamma = -\frac{0.01(y^+)^4}{1 + 5y^+}.$$

(8.21)

8.2 CFD Simulation of the FBCW

While aspects of the two-phase hydrodynamics above and below the canopy are intertwined, they can be separated to introduce independent control of the CHF. The lateral vapor perforations introduces instabilities (lateral interfacial shearing) that greatly affect the leading-edge liquid track.
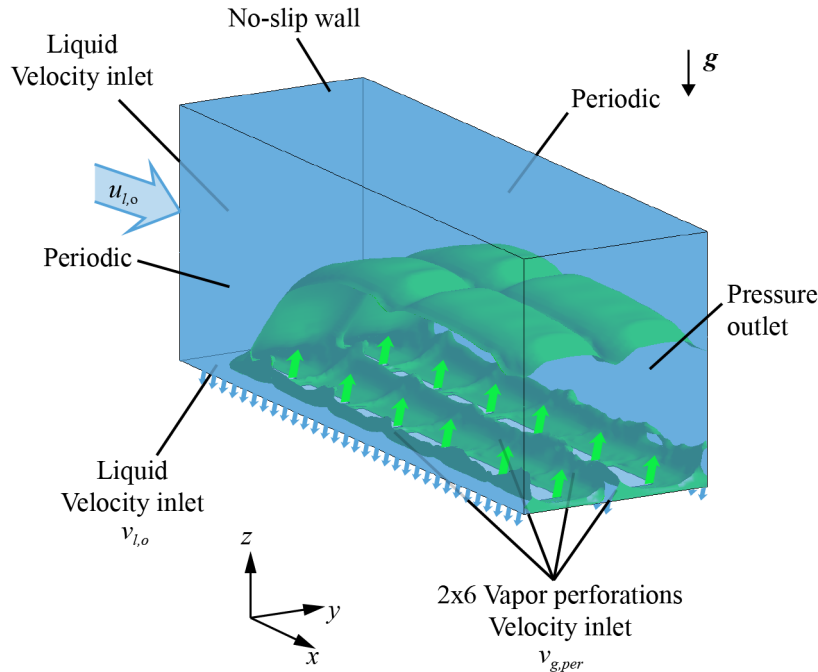
Figure 8.2: The 2x6 perforations canopy wick simulated (CFD) for the channel two-phase flow, showing the boundary conditions (irrigation of the wick and vapor escaping from the perforations).

Similarly, for longer heaters (additional axial perforations) it affects the liquid track dryout (axial interfacial shearing by progressive downstream increase of the vapor mass flow rate). To minimize the lateral size effect, two lateral perforations with lateral periodic boundary conditions are used in the CFD simulations, shown in Figure 8.2. In order to include a large enough heater length, comparable to the experiments discussed in Chapter 9, six axial perforations are used with the continuity exit condition.

The solver Ansys Fluent [109] is used with the following options: fluid-fluid; transient, incompressible, isothermal, turbulent flow (realizable k–ε model, discussed in Section 8.1), first order implicit time, explicit VOF [69] with geometric reconstruction, discussed in Section 3.2. Saturated water properties from Table 2.1 are used.

The 2x6 perforations canopy wick simulated (CFD) for both the wick liquid flow and the channel two-phase flow hydrodynamics is shown in Figure 8.3. The CFD simulations include the volume-averaged properties discussed in Section 6.1. The boundary conditions for the 3-D wick flow simulations and a typical flow traced by the streamlines, shown in Figure 8.3. The pressure
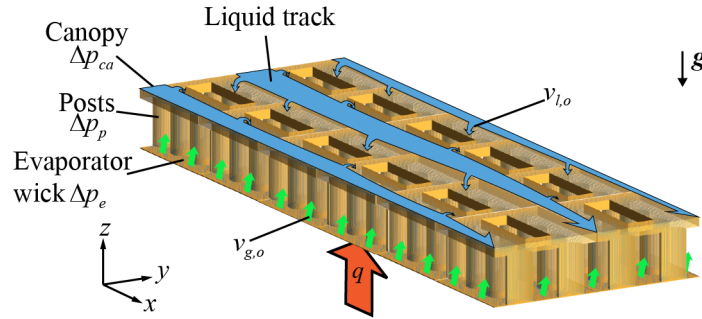
Figure 8.3: The 2x6 perforations canopy wick simulated (CFD) for the wick liquid flow, showing the boundary conditions (irrigation from the channel flow and evaporation on the evaporator wick). Typical streamlines for the liquid flow through the perforated canopy, posts, and evaporator wick are also shown.

drop from the 1-D network model is compared with these 3-D results and good agreement is found.

Since the evaporator wick properties vary locally with the meniscus thickness (which depends on heat flux), more accurate results are expected from the point-wise numerical treatment discussed in Section 6.2, where the variation of the meniscus thickness is tracked and a variable local permeability is used. However overall, the 1-D network and the 3-D CFD results suffice to predict the wick liquid flow with acceptable accuracy.

The hydrodynamics of the two-phase flow above the canopy involves the vapor escape from the perforations and subsequently merging with the liquid stream. The leading-edge liquid track, the portion of the liquid stream that flows in contact with the perforated canopy, is responsible for the axial liquid supply to the heated surface. The competition between the liquid and vapor streams increases further downstream leading to the eventual breakup of this leading-edge liquid track, which then results in dryout. This breakup of the liquid track is observed in the CFD simulations and is due to vapor-liquid interfacial shearing stability (Kelvin-Helmholtz).

The confined-geometric modulation regime discussed in Section 7.3 is also investigated under the same CFD condition. The surface of the levees are subject to the no-slip condition, and the levee height and width are $H_l = 3\,\mathrm{mm}$ and $l_l = 1\,\mathrm{mm}$, respectively. Using larger height does not alter the results. Close to the surface, the vapor stream is restricted to the intralevee channel, while the liquid is confined to the aqueduct. Phase interaction is restricted by the vapor penetration into

89

the aqueducts between the levees. Figure 8.4 shows the axial variations of the liquid track height in the aqueduct for $q = 15\,\mathrm{MW/m^2}$ and different liquid velocities. The dryout of the liquid track at the exit of the FBCW, $x = 39\,\mathrm{mm}$, is observed for the threshold velocity, $u_{l,\mathrm{o}} = 0.05\,\mathrm{m/s}$
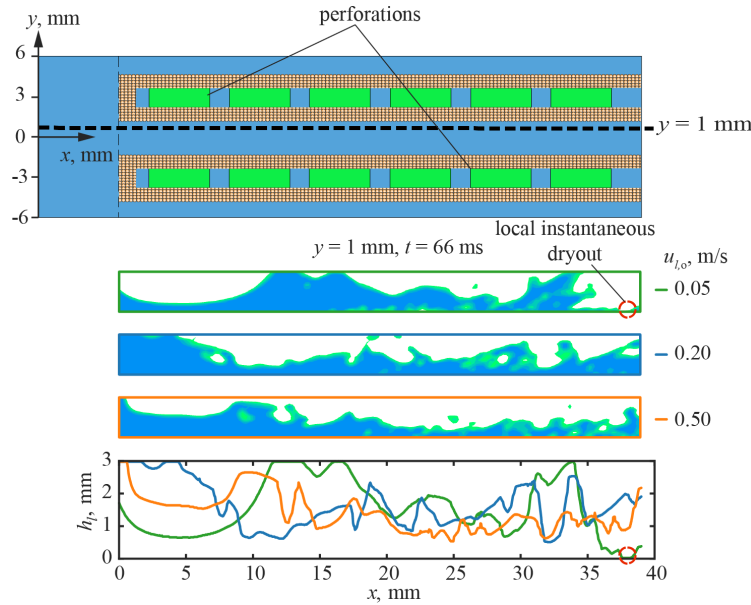
Figure 8.4: Axial variations (at $y = 1\,\mathrm{mm}$. marked with dashed line) of the liquid track height for different inlet velocities for $t = 66\,\mathrm{ms}$ and $q = 15\,\mathrm{MW/m^2}$. Local dryout occurs for the lowest velocity and also shown by snapshots of the phase distribution of the intralevee flow. Saturated water (one atm).

Figure 8.5 shows a snapshot of the phase distributions above the canopy wick from the CFD simulations with 2x6 perforations FBCW. The vapor exits the canopy wick perforation tending to destabilize the leading-edge liquid track between perforations, however, levees help stabilize the liquid track. The snapshots of the phase distributions along selected axial and lateral locations are also shown. The hydrodynamic control of the boiling crises with the FBCW capillary surface structure allows for the thermal control at high heat flux and also allows for insights into the boiling phenomena. The CFD simulation results indicate that the geometrically constrained vapor escape successfully preserves the stability of the liquid tracks while ensuring the continued axial liquid supply to wick. In Chapter 10, the results will be compared with the experimental results from the flow-boiling loop described in Chapter 9.
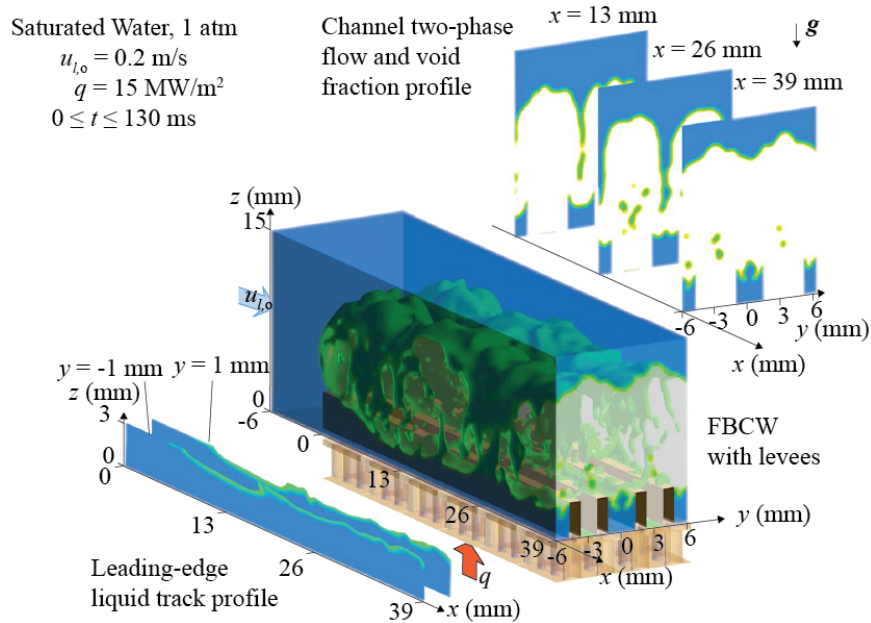
Figure 8.5: Phase distribution above and below the canopy wick for the 2x6 perforations FBCW with levees. Snapshots of phase distribution along axial and lateral locations are shown to illustrate the surface liquid track.

8.3 Summary

The DNS of the geometric modulation regime was presented using the RANS equations with the k–ε turbulence model. In the confined-geometric modulation regime, the levees stabilizing effect on the liquid track is two-fold: shielding the liquid in the intralevee aqueduct by preventing phase interaction in the region near the perforated canopy, and anchoring the liquid to the no-slip walls, requiring additional vapor-shearing to trigger K-H instability. The CFD results for the phase distributions and the liquid track will be compared with experimental results from Chapter 9 in Chapter 10.

CHAPTER 9

Saturated Water Flow-boiling Experiment with Fabricated Canopy Wick

In this chapter, the fabrication and flow-boiling testing of the FBCW are presented. The numerical results from Chapters 6 and 8 are compared and validated with the experimental results obtained in these tests. The fabrication steps (particle selection, sintering, etc.) and the experimental setup (experimental apparatus and test procedure and recording) are described. Further details are available in [89, 124].

9.1   FBCW Fabrication

Figure 9.1 shows the FBCW fabrication steps, using spherical copper particles sintered in graphite molds in a furnace [53]. Three different particle diameters were used, namely $50\,\mu\mathrm{m}$ (50–$53\,\mu\mathrm{m}$), $100\,\mu\mathrm{m}$ (100–$106\,\mu\mathrm{m}$), and $150\,\mu\mathrm{m}$ (150–$160\,\mu\mathrm{m}$). All sintering processes were completed in two hours under Ar gas at $900°\mathrm{C}$ in a tube furnace. First, the smallest particles were sintered on a polished copper plate, Figure 9.1(a) to form the first layer of the evaporator wick, Figure 9.1(b). The particles from the second layer of $100\,\mu\mathrm{m}$ particles were then sintered on top of the first to form the bimodal bilayer evaporator wick, Figure 9.1(c). Graphite molds were used to form the posts, Figure 9.1(d), and the canopy. It was subsequently sintered on top of the posts, Figure 9.1(e). The addition of levees is illustrated in Figure 9.1(f). Additional details on the fabrication are given in [124].
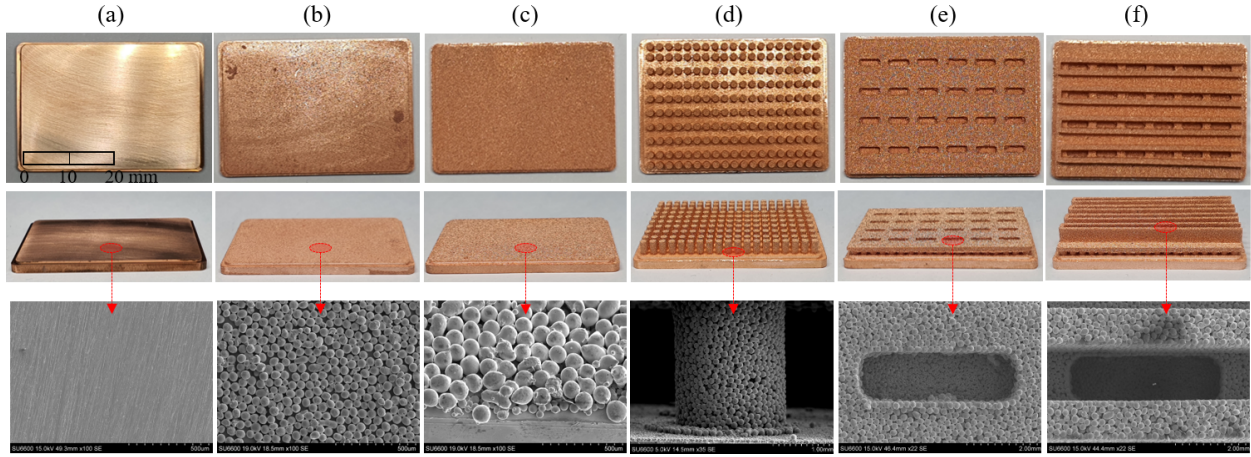
Figure 9.1: Steps in the flow-boiling canopy wick fabrication. (a) Plain copper surface sintered; (b) monolayer; (c) bimodal bilayer evaporator; (d) addition of posts; (e) canopy; (f) levees. The FBCW comprises spherical copper particles sintered in graphite. The particle size for the monolayer/bilayer evaporator, posts, and perforated canopy are progressively larger to allow capillary liquid flow toward the evaporator.

The plain surface is a copper substrate, Figure 9.1(a). It is mechanically polished using abrasive paper and the surface was cleaned with a combination of ethanol, acetone, and water. The monolayer is a single layer of $50\,\mu m$ spherical copper particles sintered on the plain surface, Figure 9.1(b). The particles are deposited by employing the Langmuir-Blodgett Film method [125]: it consists of floating the particles in a film of water, that is then drained to allow the particles to be deposited on top of the substrate in a single layer that is then sintered, Figure 9.2(a). A second $100\,\mu m$ particle layer is then deposited on top of the monolayer for the bimodal bilayer evaporator, Figure 9.1(c). The sintering process is repeated for the $100\,\mu m$ copper particles layer above the monolayer, forming the bimodal wick.

The posts are fabricated by $100\,\mu m$ or $150\,\mu m$ copper particles, Figure 9.1(d). The fabrication steps are illustrated in Figure 9.2(b): the post graphite molds are filled with the copper particles and the evaporator is placed on top of the post graphite mold, this is followed by the sintering and removal of the graphite mold. The graphite mold is machined to allow for the required number of posts ($N_{p,x}$ and $N_{p,y}$) and pitch $\Delta_{p,x}$ and $\Delta_{p,y}$). In the canopy, $150\,\mu m$ copper particles are used, Figure 9.1(e). The particles are placed in the canopy graphite mold and the posts are placed on

top of it (upside down), followed by sintering, as shown in Figure 9.2(c). For the levees, $150\,\mu m$ copper particles are used. They are sintered in a separate graphite mold and then positioned on top of the FBCW canopy, as shows Figure 9.2(d).
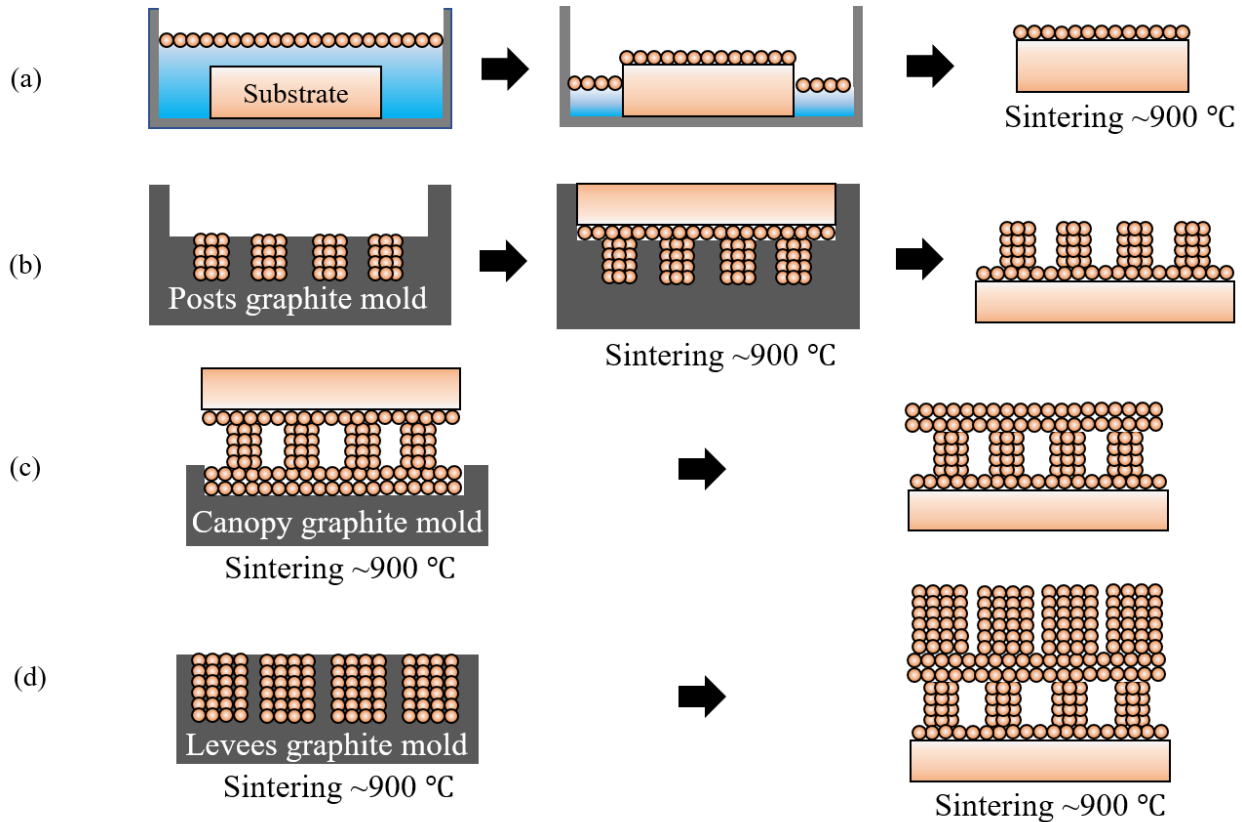
Figure 9.2: The progressive steps in the flow-boiling canopy wick fabrication. (a) Evaporator wick; (b) posts; (c) canopy; and (d) levees.

9.2 Experimental Setup

Figure 9.3 illustrates the test section setup. The test channel is made of aluminum with cross-section $A_{ch} = 20 \times 36 \mathrm{mm}^2$ and a transparent glass windows was used to visualize and record the boiling phenomenon. Cartridge heaters are inserted in the machined copper block and two thermocouples are employed for the temperature gradient measurement in the copper block, as shows Figure 9.3(a). The heat flux is calculated based on the conduction method

$$q = \frac{k_{Cu}\left(T_{Cu,1} - T_{Cu,2}\right)}{L_{12}} \tag{9.1}$$

where $T_{Cu,i}$ is the temperature measured by the thermocouple in the copper block and L_{12} is the distance between the two thermocouples.

The copper substrate is affixed to the jig made of low thermal conductivity $k = 0.25\,\mathrm{W/m\text{-}K}$ polyether ether ketone (PEEK) with epoxy. The connection part between the jig and the test channel is sealed with an O-ring. Thermal interface material (TIM, $k_{TIM} = 12\,\mathrm{W/m\text{-}K}$) is applied between the conduction heater and substrate to reduce the thermal contact resistance. The contact between the substrate and the heater block is adjusted by the z-aligner. The spring damper alleviated any thermal expansion of the conduction heater during the experiment.

Figure 9.3(b) shows the copper substrate with a surface area of 28×39 mm^2 and a thickness of $2.5\,\mathrm{mm}$. Three K-type thermocouples are inserted in holes machined in the substrate at a distance $L_s = 1.9\,\mathrm{mm}$ below the surface. The relevant dimensions of the thermocouple holes are highlighted in Figure 9.3(b). The surface temperature $T_{s,i}$ at the same three axial locations is calculated based on the thermocouple measurements $T_{o,i}$ according to

$$T_{s,i} = T_{o,i} - \frac{q}{k_{Cu}} L_s. \tag{9.2}$$

The surface superheat uses the average surface temperature

$$\Delta T_s = \langle T_s \rangle - T_{lg} = \frac{1}{3}\sum_i T_{s,i} - T_{lg}, \tag{9.3}$$

the surface superheat ΔT_s is use in the calculation of the thermal conductance G/A, given in Eq. (5.22).

The propagation of uncertainties for the relevant test quantities is presented in Appendix A. The maximum error for heat flux measurements is less than $5\,\%$ and for thermal conductance measurements it is less than $20\,\%$.

Figure 9.4 illustrates the flow-boiling loop operating with deionized water as the working fluid.

Figure 9.3: (a) Schematic of the test section with the copper block and cartridge heaters; (b) Top and side views of the substrate with dimensions. The locations of the three K-type thermocouples employed to calculate the surface temperature are also indicated. Snapshot of flow-boiling recording with the porous metasurface is also shown.

The experiments are conducted under pressure of one atm and 0–$17\,\mathrm{kpagage}$. For the majority of cases, a liquid mass flow rate of $250\,\mathrm{kg/m^2}$-s is used with small liquid inlet subcooling (3–9°C). The liquid from the reservoir passes through the flowmeter, preheater and test channel with one transparent (glass) sidewall for visualization, subsequently passing through the condenser and returning to the reservoir.

The liquid flow rate is measured with a turbine flow sensor (GMP, NURITECH) and the flow is controlled with the aid of a centrifugal pump and a needle valve for finer control. During the experiment, a preheater ($13\,\mathrm{kW}$) and a (PID) controller (TZ4ST, Autonics) control the fluid inlet temperature. A K-type thermocouple and pressure gauge (PX01C1-300GV, Omega) measure the temperature and pressure at both the channel inlet and outlet. A PI controller is used to control the power from the cartridge heaters ($12\,\mathrm{kW}$ total) in the copper block. The heat flux is determined according to Eq. (9.1). The data acquisition system (34970a, Agilent) collects the flow rate, temperature, pressure, and heat flux at $1\,\mathrm{s}$ intervals. Additional details on the flow-boiling loop components, test section, and measurement devices are given in [124].
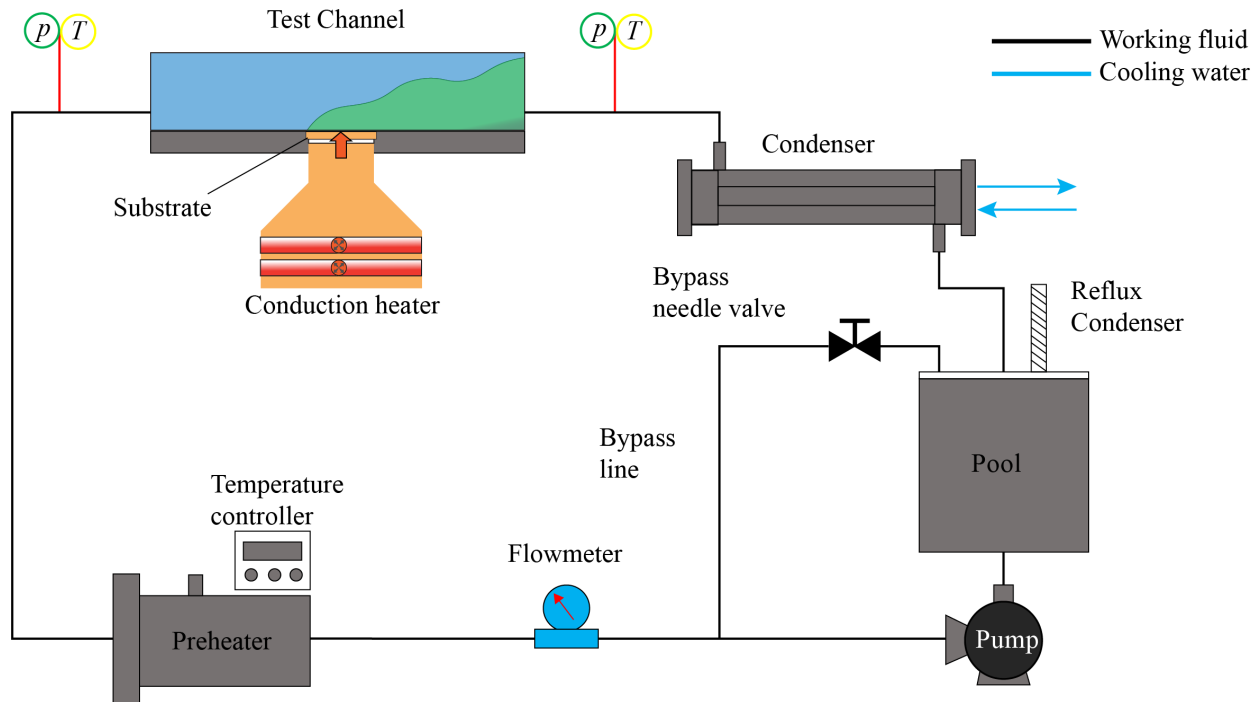
Figure 9.4: Schematic representation of the flow-boiling loop highlighting the main components.

Before the start of a test, the apparatus is operated for one hour with no load in the degassing process. After degassing, the heater is turned on and increasingly powered to the test heat flux in steps through the PID controller. The heat flux and the surface temperature are maintained under a steady-state for five minutes at each step. The data for each step is averaged over two minutes. When the temperature of the surface increases abruptly, indicating the boiling crisis is reached, the power of the heater is turned off and the test surface and the heater are separated by the z-aligner to prevent damage to the system. Additional details on the test setup are given in [124].
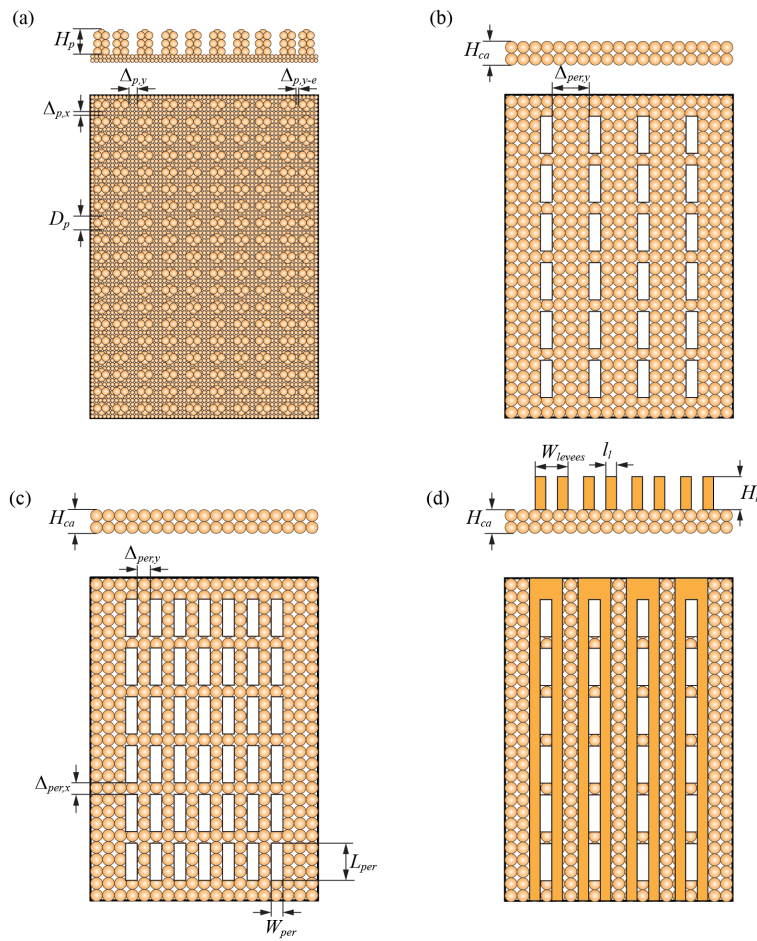
Figure 9.5: Various flow-boiling canopy wick designs (a) No canopy; (b) Low-density perforation canopy wick with 4×6 perforations; (c) High-density perforation canopy wick with 7×6 perforations; (d) Low-density perforation canopy wick with levees.

Table 9.1: Geometric parameters of the varied flow-boiling canopy wick designs. For the case with levees: $H_l = 5\,\text{mm}$ and $l_l = 1\,\text{mm}$.

Design	H_p (mm)	D_p (mm)	$\Delta_{p,x}$ (mm)	$\Delta_{p,y}$ (mm)	$\Delta_{p,y\text{-}e}$ (mm)	H_{ca} (mm)	$\Delta_{per,y}$ (mm)	W_{per} (mm)	W_{per} (mm)
No canopy	1.3	1.5	0.5	1.5	0.75	1	4.5	1.5	4.5
FBCW low-density perforation	1.3	1.5	0.5	1.5	0.75	1	4.5	1.5	4.5
FBCW high-density perforation	1.3	1.5	0.5	1.5	0.75	1	1.5	1.5	4.5
FBCW with levees	1.3	1.5	0.5	1.5	0.75	1	4.5	1.5	4.5

9.3 FBCW Designs

Figure 9.5 illustrates the FBCW design variations employed in the experiments. In the first design, no canopy was, only the sintered evaporator wick and posts on top of the copper plate [Figure 9.5(a)]. The canopy was added in the full FBCW with the 4×6 perforations [(low density), Figure 9.5(b)]. The high-density perforation comprised 7×6 perforations [Figure 9.5(c)]. Finally, the FBCW with levees is shown, using the low-density perforation configuration, since the lateral inter-perforation spacing of the high-density configuration does not allow the addition of levees [$\Delta_{per,y} < 2l_l$, Figure 9.5(d)]. The levees diverted the vapor away from the liquid track above the canopy, allowing for a higher hydrodynamic dryout limit [62].

Specification of geometric parameters listed in Figure 9.5 are given in Table 9.1 for all four designs.

9.4 Summary

The FBCW fabrication process was presented alongside the flow-loop used to test the CHF and thermal conductance enhancements achieved with the porous metasurface. The flow-loop components are listed and the test routine is described. Experimental results are presented in the sequence in Chapter 10 and compared to numerical results from Chapters 6 and 8.

CHAPTER 10

Results and Discussions

In this chapter, the experimental and numerical results for the CHF and thermal conductance in the wavelength and geometry modulation regimes (including confined-geometric regime) using the FBCW porous metasurface are presented. The phase distributions from the experiments and simulations are presented and compared. In Appendix B, these videos are described in details, including timestamps identifying events within the videos.

10.1   Liquid and Vapor Flows and Phase Distribution

The FBCW premise is to allow for orderly thin meniscus evaporation over a thin wick with ensured vapor space above the evaporator wick and lateral liquid supply through the wick. The experimental results are for saturated water (one atm) with a liquid velocity of $u_{l,\mathrm{o}} = 0.25\,\mathrm{m/s}$. From the visualization videography, the snapshot in Figure 10.1(a) indicates that this liquid flows through the porous posts to the evaporator wick, where it is evaporated. The thin evaporator wick and the vapor space above it leads to a large thermal conductance (heat transfer coefficient), allowing reaching dryout limits beyond that recorded for the plain surface. The full video is shown in Appendix B.2.1 and discussed with the relevant timestamps highlighted.

   A corresponding higher liquid supply to the posts is needed to reach these higher dryout limits. The perforated canopy allows for the separation of vapor space from the liquid, flowing through the channel while allowing the vapor to escape steadily, as shows Figure 10.1(b). By controlling the perforation spacing and preventing the escaping vapor from shear destabilizing the liquid track,

the hydrodynamic CHF is enhanced beyond the plain-surface results. The levees further facilitate this control due to the confinement of the escaping vapor, securing the liquid track in the aqueduct, as shown in Figure 10.1(c).
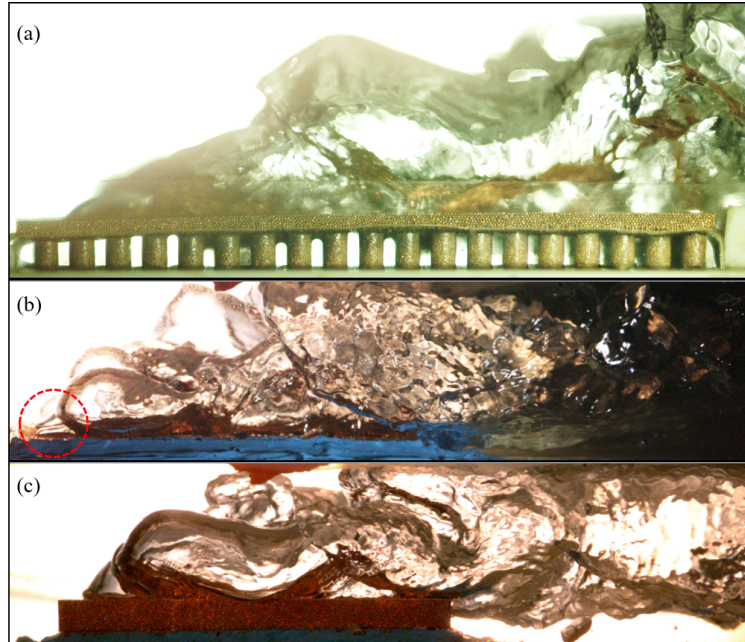
Figure 10.1: Video snapshots of the experiment indicating (a) vapor generation in the vapor space (below the canopy), and vapor escape through the perforations; (b) without levees; (c) with levees. The results are for saturated water (one atm), $q = 2.5\,\mathrm{MW/m^2}$, and $u_{l,\mathrm{o}} = 0.25\,\mathrm{m/s}$.

A direct comparison between the topology observed in the experimental results for $q = 2.2\,\mathrm{MW/m^2}$ and $u_{l,\mathrm{o}} = 0.25\,\mathrm{m/s}$ with the CFD results for $q = 2.5\,\mathrm{MW/m^2}$ and the same inlet velocity is shown in Figure 10.2. The results are for saturated water (one atm). A general agreement exists between the experiments and numerical predictions. The FBCW includes the levees. The full video is shown in Appendix B.2.2 and discussed with the relevant timestamps highlighted.

The flows above and within the FBCW are separately shown in Figure 10.2. The predicted and observed/recorded flow behaviors are in good agreement and both show the effect of geometric confinement of the canopy surface liquid tracks. In both cases, the levees successfully prevent the vapor-flow shearing destabilizing the surface liquid track, removing the otherwise hydrodynamic limit. The liquid-vapor interface in the midplane ($y = 0\,\mathrm{mm}$), represented by the constant void fraction $\alpha_g = 0.5$, is clearly shown in detail in the CFD snapshot. Under this condition, the wick-
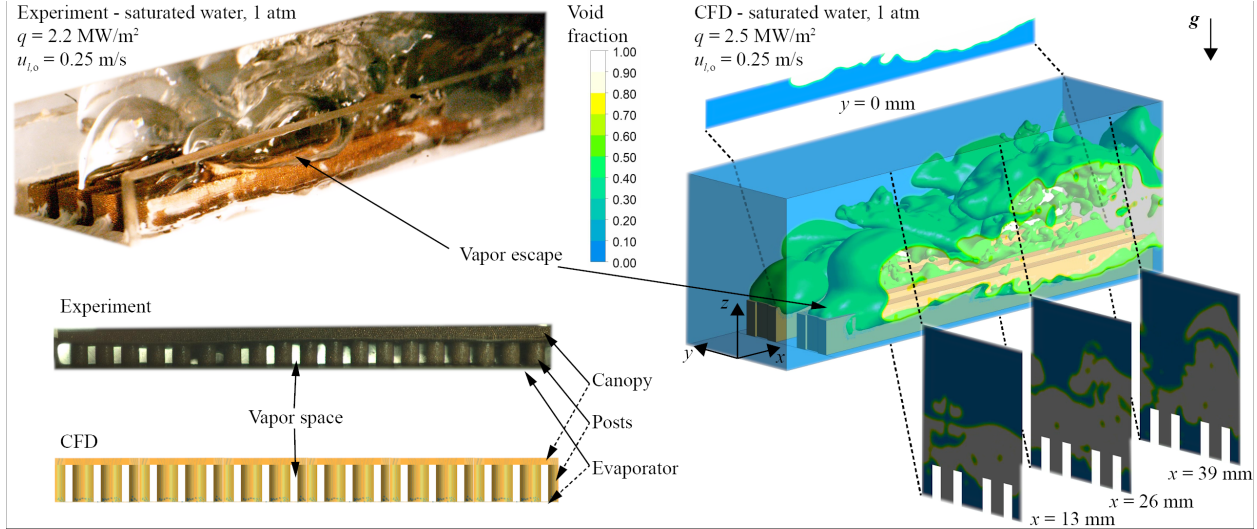
Figure 10.2: Comparison of experiments ($q = 2.2\,\mathrm{MW/m^2}$) and computational fluid dynamics simulations ($q = 2.5\,\mathrm{MW/m^2}$) snapshots of the flow-boiling canopy wick with levees. The vapor formation in the vapor space (below the canopy) and vapor escape from the canopy (through the perforation among the levees) are evident. The observed and simulated liquid flow through the wick is also presented. The results are for saturated water (one atm) with $u_{l,\mathrm{o}} = 0.25\,\mathrm{m/s}$.

imposed limit, i.e., the capillary-viscous dryout limit, is the bottleneck and controls the dryout.

10.2 Capillary-Viscous and Hydrodynamic Limits

Figure 10.3 shows the variations of the measured surface superheat $\langle T_s \rangle - T_{lg}$ (x axis) with the heat flux (y axis) from experiments, and also the variations of the predicted heat flux with the overall wick pressure drop $\sum \Delta p_i$ for different FBCW designs for saturated water (one atm).

The experimental results on the left include the plain surface results including the CHF, which is $q_{CHF,h} = 1.9\,\mathrm{MW/m^2}$, marked by the black triangle. The error bars for the heat flux and surface superheat measurements correspond to the propagated uncertainty presented in Appendix A. The blue symbols correspond to different designs of the monolayer evaporator wick. The geometric parameters of the post wick were also varied, including the post particle diameter $d_p = 100$ and $150\,\mu\mathrm{m}$ and post height $H_p = 1.3$ and $2.6\,\mathrm{mm}$. The highest measured CHF is $q_{CHF,c\text{-}v}$, recorded with the short height and large particle (reduced viscous pressure drop) post design. This is a capillary-viscous limit, controlled by the maximum monolayer capillary pressure, which is lower

than the ideal value predicted in Section 6.1.1.

To the right of Figure 10.3 are the overall pressure drop (canopy, posts, evaporator wick and vapor escape, from Eqs. (4.1) and (5.22)) and corresponding to a given capillary-viscous limit. Both upper and lower limits of $q_{CHF,c\text{-}v}$ obtained experimentally are predicted by the network model, corresponding to the lowest and highest post pressure drop configurations: post pressure drop Δp_p is given by Eq. (5.6), with the permeability found from Eq. (5.8), the short post $H_p = 1.3\,\mathrm{mm}$ with large particles $d_p = 150\,\mu\mathrm{m}$ leads to the lowest Δp_p.

The orange symbols represent a switch to the bimodal bilayer wick. A capillary-viscous CHF enhancement of $q_{CHF,c\text{-}v} = 4.6\,\mathrm{MW/m^2}$ for the short post design is observed. The increase is attributable to the larger average liquid layer thickness $\langle \delta_l \rangle$ discussed in Section 6.1.2 and shown in Figure 6.3. This limit is in a good agreement with the network model prediction of $q_{CHF,c\text{-}v} = 5.0\,\mathrm{MW/m^2}$ for the same wick, Eq. (5.22). The agreement confirms the limit is due to the maximum capillary pressure (capillary-viscous limit).

To reduce the pressure drop across the perforations, the perforation number was increased, reducing the related discharge coefficient. The four canopy designs are discussed in Section 9.3 and illustrated in Figure 9.5(c). An incremental increase in the CHF is recorded, raising the limit to $q_{CHF,c\text{-}v} = 5.1\,\mathrm{MW/m^2}$, as expected from the lower total pressure drop. This high perforation number canopy does not allow for the addition of levees, but it allows for a higher capillary-viscous limit by reducing the vapor velocity exiting the perforation, therefore, reducing the inertial pressure drop component.

The green line on the right (predictions) side of Figure 10.3 denotes another feasible improvement to the capillary-viscous limit when the posts lateral spacing $\Delta_{p,y}$ is made equal to the perforation width and narrower perforations are used with $W_{per} = 1\,\mathrm{mm}$. The further reduction of the perforation width draws the posts closer, therefore, reducing the evaporator pressure drop since the evaporator wick unit cell is centered around the post, as discussed in Section 6.2. The main drawback is the increase in the vapor escape pressure drop, Δp_g, which varies with the square of the heat flux. At lower heat flux, however, this represents less than 10% of the overall pressure
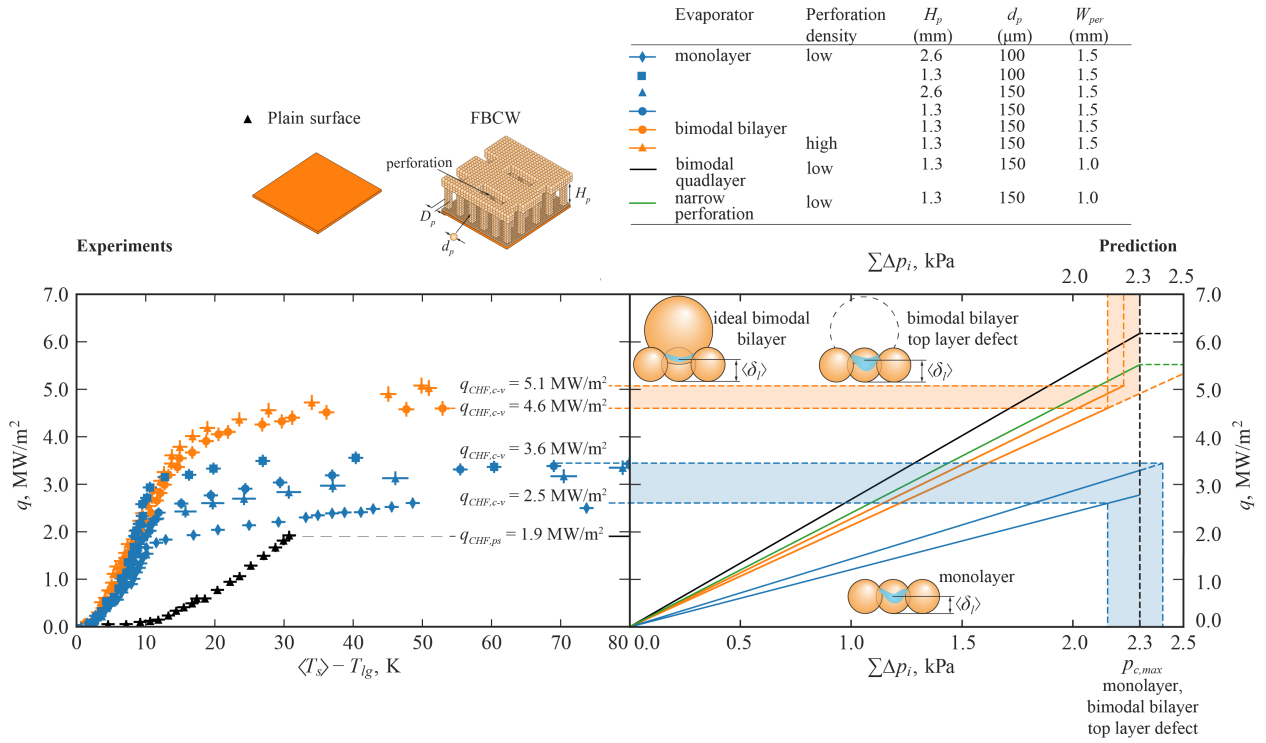
Figure 10.3: Evolution of the flow-boiling canopy wick design to enhance the heat flux limit. Left: flow-boiling curve of various FBCW wick designs. Right: variations of capillary-viscous CHF with the total pressure drop for different FBCW wick designs. The results are for saturated (one atm) water with a liquid velocity of $u_{l,\mathrm{o}} = 0.25\,\mathrm{m/s}$.

drop in the system. Reducing the perforation width from 1.5 to $1.0\,\mathrm{mm}$ increases the predicted capillary-viscous limit to $q_{CHF,c\text{-}v} = 5.5\,\mathrm{MW/m^2}$.

Further enhancement can be achieved by utilizing a thicker evaporator wick with smaller particles (for optimal liquid transport by reducing the liquid pressure drop, while increasing the thermal resistance), as illustrated in Figure 6.8 with values listed in Table 6.1. The capillary-viscous limit with a bimodal quadlayer wick is predicted to have a $q_{CHF,c\text{-}v} = 6.3\,\mathrm{MW/m^2}$. This is a noticeable increase compared with that achieved with the current wick design.

The predicted ideal second-layer packed bimodal bilayer maximum capillary pressure and permeability, presented in Figures 6.2 and 6.3, suggest that the CHF can be further increased. This is indicated with the shaded rectangle on the top right corner of Figure 10.3. The error bars correspond to a maximum of $0.2\,\mathrm{MW/m^2}$ or 4% of the heat flux, and $1.2°\mathrm{C}$ of the surface (wick) superheat. The uncertainty estimates are discussed in Appendix A.

In order to place the FBCW CHF and thermal conductance enhancements in perspective, Figure 10.4 shows the evolution of the evaporator, starting with the flow boiling on a plain surface with the previously mentioned hydrodynamic limit of $q_{CHF,h} = 1.9\,\mathrm{MW/m^2}$. The addition of the evaporator wick with posts and no canopy, similar to the modulated pool-boiling metasurface from [53], discussed in Section 4.1, provides a CHF enhancement to $q_{CHF,h} = 3.9\,\mathrm{MW/m^2}$. This is a hydrodynamic limit since it is lower than the predicted capillary-viscous limit and, in the absence of the perforated canopy, no effective phase separation is observed near the heated surface and the boiling crisis is triggered, although with a modulated wavelength λ_c. The addition of the perforated canopy changes the boiling crisis limit to the capillary-viscous limit, $q_{CHF,c\text{-}v} = 4.6\,\mathrm{MW/m^2}$. The final modification is the inclusion of the levees (using the lower perforation number design, listed in Table 9.1). The experimental results show no further CHF enhancement at this point, and even the thermal conductance, discussed in the sequence, is reduced. This is an indication of a defective fabricated wick, but the results are still much higher than the plain surface, $q_{CHF,c\text{-}v} = 4.2\,\mathrm{MW/m^2}$.

The liquid entrainment among posts without the canopy affects the thermal conductance (heat transfer coefficient) G/A. Adding the posts and the bimodal bilayer evaporator wick increases the thermal conductance to $G/A = 0.36\,\mathrm{MW/m^2\text{-}K}$. The uncertainty in G/A is derived in Appendix A, estimate around 20% (Table A.1). The presence of the canopy creates a vapor space on top of the evaporator, resulting in a significantly smaller thermal resistance [governed by the thickness of the liquid layer $\langle \delta_l \rangle$ and the effective thermal conductivity of the evaporator $\langle k_e \rangle$, Eq. (5.23)], as discussed in Section 5.2.4. This thermal conductance corresponds to an effective thermal conductivity $\langle k_e \rangle = 14\,\mathrm{W/m\text{-}K}$, with the average liquid layer thickness $\langle \delta_l \rangle = 40\,\mathrm{\mu m}$, consistent with the correlation for the bulk thermal conductivity of water-copper particles with a porosity of $\epsilon = 0.4$ [108] and slightly above the values predicted in Section 6.1.3 and shown in Figure 6.4.

On top of Figure 10.4, the schematic representation of the evaporation surfaces are shown for the plain surface, evaporator wick and posts (no canopy), FBCW, and FBCW with levees. Snapshots
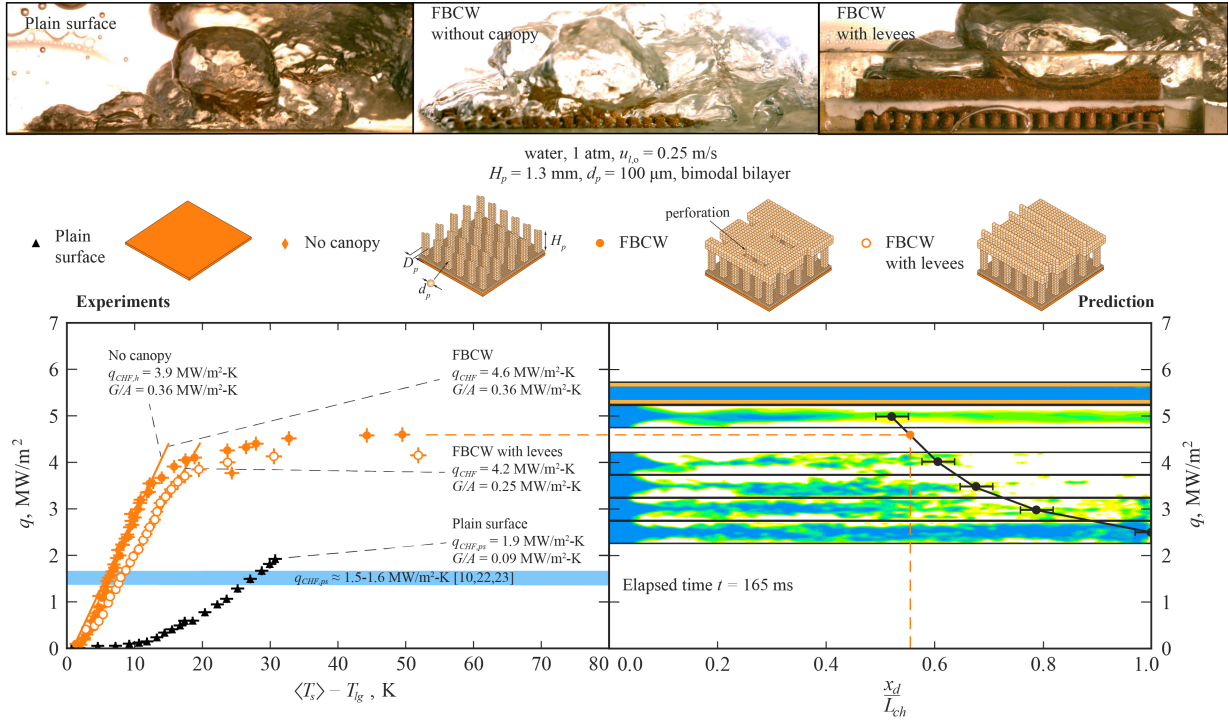
Figure 10.4: The experimental results for variations of heat flux with the superheat for the mono-layer and bimodal bilayer evaporators. Comparison of experimental results for plain surface and the enhancements obtained with evaporator layer + posts, and evaporator layer + posts + canopy (FBCW). Left: flow boiling curve. Right: CFD snapshots of axial phase distribution immediately above the canopy for FBCW. The video snapshots are also shown on top for the plain and FBCW experiments. The results are for saturated (one atm) water with liquid velocity of $u_{l,\mathrm{o}} = 0.25\,\mathrm{m/s}$.

of video recordings from experiments for the plain surface, evaporator and posts and the FBCW with levees are also shown to illustrate the phase distributions in the channel.

The right of Figure 10.4 shows the CFD snapshots of the top view of the surface liquid track in the central region of the channel (aqueduct for the FBCW with levees) at $z = 0.25\,\mathrm{mm}$. The x axis shows the normalized axial coordinate. The dryout surface fraction, or the axial location of the canopy for which dryout is observed downstream, is marked for different heat flux. The CHF of $q_{CHF,c\text{-}v} = 4.6\,\mathrm{MW/m^2}$ corresponds to a dryout surface fraction of 45%, indicating that at this location the hydrodynamic dryout has not been reached since the liquid supply in the leading-edge region is still stable.

10.3   Summary of Modulation Regimes

Figure 10.5(a) and (b) show the variations of the hydrodynamic CHF with the critical wavelength λ_c and inlet velocity $u_{l,o}$. The three CHF enhancement regimes, namely the wavelength, geometry, and geometry-confined modulation with levees, are marked, as well as their transitions (boundaries).

The wavelength-modulation CHF is given by Eqs. (2.11) and (2.23) and is primarily controlled by $u_{l,o}$ and presented with the dashed gray line. The inlet velocity reduces the critical wavelength causing higher vapor velocity and increases the heat flux required to trigger the hydrodynamic instability. This enhancement is limited by the smallest physically-limited wavelength, i.e., the capillary length, marked in Figure 10.5(a). The predicted-correlated 1/6 power-law dependency of the CHF on the inlet velocity is shown in Figure 10.5(b) and is in general agreement with the low and high-velocity experiments.

The geometry modulation, decoupling the wavelength from the inlet velocity, allows for a larger enhancement, as shown with the crosshatch regime in Figure 10.5(a). The CFD predictions [62] and experimental results [89, 126, 127, 128] are also shown. This enhancement is controlled by the vapor confinement provided by the rectangular perforations, restricting the vapor lateral expansion and preserving the surface liquid tracks. The orange region in Figure 10.5(b) is bound by the q_{CHF}-$u_{l,o}$ relation Eq. (2.23) at the bottom, and the K-H instability Eq. (7.4) on the top. The capillary-viscous metasurface-controlled limit is not shown since it depends on the characteristic wavelength of the metasurface, which is decoupled from the inlet velocity.

The current results show the limits for the K-H dominated geometry modulation $q_{CHF,h}$ and the porous metasurface $q_{CHF,c\text{-}v}$ are rather close, as confirmed by experiments [124], so no further enhancements can be obtained before further improvement to the porous metasurface, i.e., increasing the $q_{CHF,c\text{-}v}$. After that, to continue increasing the $q_{CHF,h}$, the use of levees is required, i.e., the geometric-confined modulation regime, represented by the blue color in Figure 10.5(a), creating the intralevee spacing which effectively raises CHF to $q_{CHF,h} > 10\,\mathrm{MW/m^2}$. The wick superheat limit, which marks vapor forming within the evaporation wick is reached there, and is estimated as
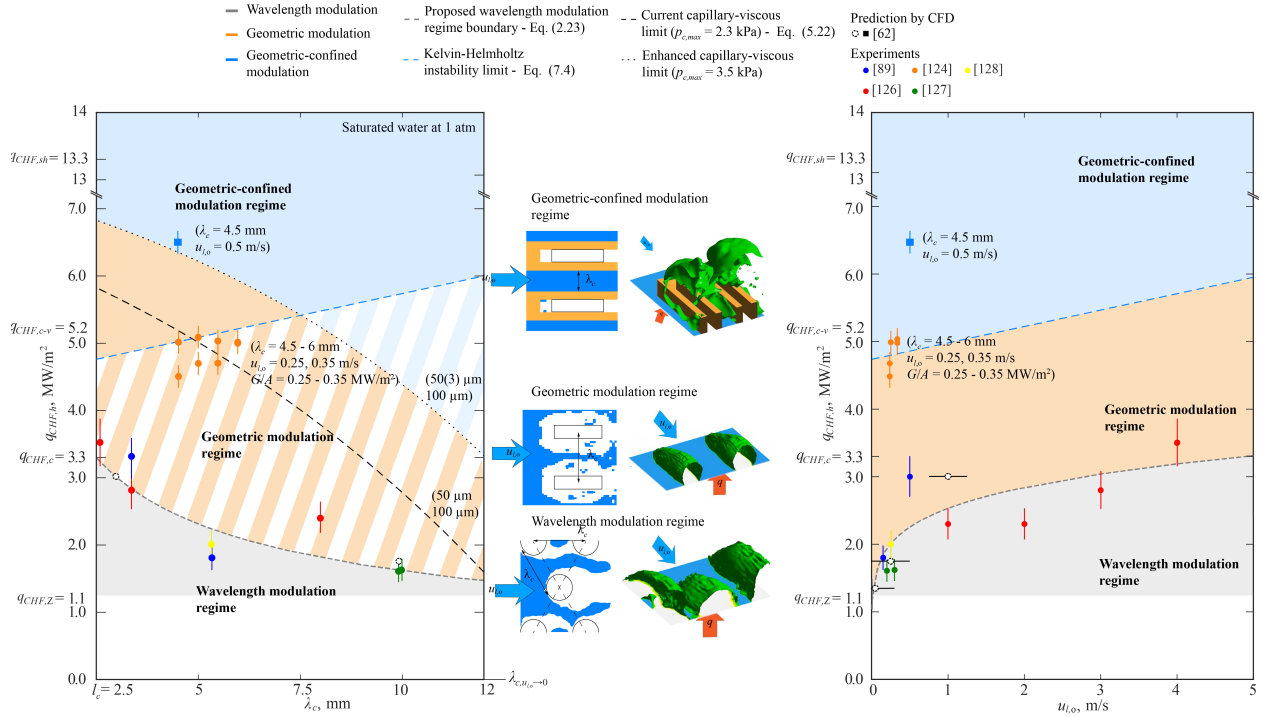
Figure 10.5: Regime diagram showing the variations of flow-boiling CHF with (a) wavelength and (b) inlet velocity. The three modulation regimes are highlighted: wavelength modulation, geometric modulation, and geometric-confined modulation, as well as their boundaries. Experimental data and CFD data are also shown. Orange circles denote experimental data for geometric modulation including length scale, inlet velocity and global thermal conductance.

$q_{CHF,sh} = 13.3 \, \text{MW/m}^2$ for the current FBCW [89]. The measured FBCW thermal conductance G/A, which is rather very high, is shown in Figure 10.5, the values are also listed in Table 6.1.

The analysis is supported by the visualization of the phase distribution in the channel for the various conditions discussed in Chapters 7 and 8. In Appendix B.1, video renderings of the CFD simulation of the three regimes are shown with an accompanying detailed explanation of the observed events and relevant timestamps (elapsed time snapshots).

10.4 Summary

The comparison between the CFD (DNS) predictions and the experimental results confirms the validity of CHF enhancement in the various modulation regimes, controlled by the FBCW porous metasurface. The comparisons also show good agreement between the experiments and the CFD

predictions, indicating the suitability of the adopted modeling. The flow-boiling crisis trigger mechanism, i.e., the onset of dryout in the leading-edge surface liquid track, is verified in the wavelength modulation regime, and the proposed control enhancement of the CHF by geometric arrangement of vapor escape sites was confirmed. The use of porous metasurfaces and their design and physical models used to predict the CHF and thermal conductance enhancements are successfully validated with experimental results.

CHAPTER 11

Conclusions

The main underlying postulate of this work is replacement of the random surface bubble nucle-ation and the consequent fate of the bubble, with thin liquid film evaporation in capillary surface structures. To arrive at this and propose such porous metasurfaces, the flow-boiling crisis hydro-dynamics is simplified and treated using two-phase flow unit-cell models. This unit cell and its two-phase flow, including numerical simulations, allow for understanding and engineering of the surface structure. A particular result of this was the observation of the leading-edge surface liquid track and its stability. This liquid track is destabilized by the shearing vapor adjacent to surface. This realization allowed for establishing this new dryout triggering mechanism and using the two-phase flow fundamentals to simulate and explain it. It also showed and allowed for the proper control (design) of the surface liquid and vapor sites to delay the surface dryout (boiling crisis). The capillary surface structure is envisioned and designed to provide these surface liquid and vapor supplies, while allowing for thin film evaporation underneath it.

In this work, direct simulation of saturated water (one atm) flow boiling crisis leading to sur-face dryout (CHF), based on the unit-cell, pool boiling hydrodynamic instability theory is used to develop the flow boiling wavelength modulation by the liquid-flow velocity $u_{l,\mathrm{o}}$. Different from simplified models available in the literature, here the turbulence-augmented interfacial transport is considered by employing the LES turbulence treatment. The unit-cell size is related to the critical wavelength, which in turn is related to the CHF. In the flow boiling DNS, the vapor and liquid ve-locities on the heated surface are prescribed, according to the Zuber liquid-vapor counter flow with

110

columnar vapor jets. The forced flow directs the vapor downstream, breaking the symmetry of the Zuber unit cell, establishing the axial liquid supply. The results for $u_{l,o} > 0$ show a leading-edge, surface liquid track formed on the heated surface leading to an axial, inertial-dominated liquid supply, in comparison with perpendicular, gravity-dominated liquid supply. This track meanders between the vapor columns and becomes unstable once the CHF is reached. At this point, dryout occurs within the first (leading edge) unit cell.

This is called the wavelength-modulation CHF enhancement regime and ranges from a low $u_{l,o}$ value corresponding to the Zuber pool boiling CHF $q_{CHF,Z} = 1.1\,\mathrm{MW/m^2}$ to the capillarity limit of about $q_{CHF,c} = 3.3\,\mathrm{MW/m^2}$, where the wavelength reaches the capillarity length based on the critical Bond number. This predicted range is in good agreement with experiments and a correlation is proposed based on the product of the Bond and liquid Reynolds numbers relating the critical wavelength and $u_{l,o}$. By resolving the small scale turbulent eddies, the effects of the fundamental forces (inertial, viscous, gravity and surface tension) can be understood, leading to a novel physical relation between the inlet velocity and the modulated hydrodynamic CHF. This new relation has $q_{CHF,h}$ proportional to $u_{l,o}^{1/6}$.

The DNS results also show that to reach beyond the wavelength-modulation CHF enhancement regime, the vapor site geometry should be anisotropic, with rectangular vapor sites aligned with the flow direction to allow for stable leading-edge liquid tracks. This is called the geometric-modulation regime and upon optimization of the site geometry using fabricated wicks reaches the next hydrodynamic limit $q_{CHF,h}$ which is over $10\,\mathrm{MW/m^2}$, and is made possible by delaying the vapor shearing (Kelvin-Helmholtz) destabilizing the surface liquid tracks. The geometric confinement of the liquid track by levees placed around the vapor sites prevents the onset of the Kelvin-Helmholtz instability and further enhances the CHF.

The geometric modulation, including liquid track confinement, is achieved by porous metasurfaces, which are 3-D porous and perforated wicks such as the flow-boiling canopy wick (FBCW). The FBCW structure delivers liquid from the liquid tracks formed on a perforated, porous canopy to porous posts and finally to a thin evaporator wick. The fabricated porous metasurface controls

the vapor-site geometry with a multicomponent sintered wick structure. The liquid transport arteries and the liquid spreading layer beneath the canopy allow for the formation of a vapor space. The vapor formed over the evaporator flows between posts and escapes through the perforated canopy, mixing with the flowing liquid in the channel. The geometric modulation moderates the vapor lateral expansion, reducing the vapor shearing and allowing the leading-edge surface-liquid track to remain stable. This effect is more pronounced under the geometric-confined regime where the levees anchor the liquid track and divert the vapor toward the channel flow.

The capillary network introduces the internal hydrodynamic limit within the porous structure, the capillary-viscous limit $q_{CHF,c\text{-}v}$. It is controlled by the maximum capillary pressure and the wick effective (volumetric) properties, which are estimated using surface energy minimization principles and 3-D numerical solvers. The predicted capillary-viscous limit for saturated (one atm) water is $5.2\,\mathrm{MW/m^2}$. Direct numerical simulations of the two-phase flow above and below the canopy are used to verify the geometry modulation CHF enhancement limited by Kelvin-Helmholtz instability, including the geometric confinement performed by the levees. The predicted results are validated with experimental results for the fabricated canopy.

CHAPTER 12

Future Work

Further studies of the flow-boiling crisis trigger mechanisms in different modulation regimes (wavelength and geometry) will provide insights and novel physical understanding of the surface dryout phenomenon. Here, possible extensions of the CHF and thermal conductance enhancement capabilities of the porous metasurfaces are suggested.

- Investigation of novel wick fabrication methods that enable the verification of the theoretical monolayer maximum capillary pressure. Currently, the capillary action is the bottleneck of CHF enhancement due to particle packing defects observed in the sintered evaporator wicks.

- The DNS CFD simulations of the flow-boiling at the low velocity limit and the recovery of the pool-boiling CHF limit. Verification of the pool-boiling CHF limit as the lower bound of the wavelength modulation regime will provide the basis for a unified boiling crisis theory spanning the range of liquid inlet velocity $0 \leq u_{l,o} \leq u_{l,o,max}$.

- Extension of the analysis for different working fluids and porous materials. Saturated water is very suitable for capillary flows, due to its high heat of evaporation, surface tension and thermal conductivity, along with a low viscosity. Different heat dissipation applications may require inert, synthetic fluids with different physical properties and chemical compatibility with the wick materials, therefore different optimized porous metasurface for the various modulation regimes.

- In the channel flow simulations, the perforated canopy surface which is permeable, is treated

with prescribed liquid suction and vapor injection. The surface is otherwise treated as smooth, i.e., the roughness of the porous surface is not addressed. This exclusion needs to be evaluated considering the sintered particle size used in the canopy wick (comparison with the laminar sublayer thickness.)

- The case of subcooled liquid channel flow would bring in vapor condensation and this should be addressed, since some subcooling does occur in practice.

- Although not addressed here, surface porous structures when working with not pure water, are subject to fouling which alters the pore structure. This and similar practical aspects should be addressed to identify the level of purity required from the working fluid.

- The meniscus analysis is based on the static simulations with the Surface Evolver. So, any advancing or receding contact angle features is not addressed. Future studies can address this contact angle dynamics.

- This study used a $45°$ contact angle, typical of water on copper surface. Future studies can extend these to more hydrophobic or hydrophilic surfaces.

- The hydrodynamics marginal, linear stability analysis did not include the viscous effects. These can be included to extend the results and perhaps replace the empirical viscous effect which was introduced and led to the $u_{l,o}^{1/6}$ relation of the hydrodynamics CHF.

APPENDIX A

Uncertainties in the Flow-Boiling Experimental Results

The uncertainty sources of a measured parameter X can be defined as systematic (statistical bias) or random. The systematic uncertainty b_X explains uncertainties regarding the measurement instrument or method, diminished by calibration procedures. The random uncertainty s_X conversely, justifies random sources [129, 130]. The combined uncertainty of X is then calculated as

$$u_X^2 = b_X^2 + s_X^2 \qquad (A.1)$$

where s_X is often approximated as the sample standard deviation. When dealing with a derived parameter $R = f(X_1, X_2, \ldots, X_k)$, its combined uncertainty can be calculated by the uncertainty propagation method [129]

$$u_R = \left[\sum_{j=1}^{k} \left(\frac{\partial R}{\partial X_j} \right)^2 u_{X,j}^2 \right]^{1/2} . \qquad (A.2)$$

The uncertainty reported is the expanded uncertainty

$$U_R = K_R u_R, \qquad (A.3)$$

where K_r is the coverage factor, a number representative of the confidence interval associated with the reported uncertainty. A confidence interval of $95\,\%$ is commonly used; for a large number of

measurements, $K_r = 1.96$. If the coverage factor is concealed in the manufacturer's datasheet, a rectangular distribution is assumed, $K_r = 1.73$.

The uncertainties for the heat flux and thermal resistance are now derived. The heat flux is calculated employing the electrical power method as

$$q = \eta_e \frac{Q}{A} = \eta_e \frac{\Delta\varphi}{AR_e}, \tag{A.4}$$

where η_e is the effectiveness of heat absorption, $\Delta\varphi$ is the voltage, R_e is the electric resistance, A is the heater block area.

If the conduction method was used instead, the heat flux would be calculated as

$$q = \frac{k_{\mathrm{Cu}} \left(T_{\mathrm{Cu},2} - T_{\mathrm{Cu},1} \right)}{L}, \tag{A.5}$$

where k_{Cu} is the thermal conductivity of copper, L is the distance between the two thermocouples inside the block and $T_{\mathrm{Cu},i}$ is the temperature measured in the block.

By employing Eq. (A.4) (electrical power method), the combined uncertainty expression for the heat flux is derived

$$u_q = \left[\left(\eta_e \frac{2\Delta\varphi}{AR_e} \right)^2 u_V^2 + \left(\eta_e \frac{\Delta\varphi^2}{AR_e^2} \right)^2 u_{R,e}^2 + \left(\eta_e \frac{\Delta\varphi^2}{A^2 R_e} \right)^2 u_A^2 \right]^{1/2}, \tag{A.6}$$

where u_A is the uncertainty of the heater block cross-sectional area $A = LW$, given as

$$u_A = \left(W^2 u_L^2 + L^2 u_W^2 \right)^{1/2}, \tag{A.7}$$

where L and W are the length and width, respectively.

Similarly, by employing Eq. (A.5) (conduction method), the following expression for the combined uncertainty is derived

$$u_q = \left\{ \left[\frac{(T_{\text{Cu},2} - T_{\text{Cu},1})}{L} \right]^2 u_k^2 + \left(\frac{k_{\text{Cu}}}{L} \right)^2 u_T^2 + \left[\frac{k_{\text{Cu}} (T_{\text{Cu},2} - T_{\text{Cu},1})}{L^2} \right]^2 u_L^2 \right\}^{1/2}, \qquad \text{(A.8)}$$

where u_k is the thermal conductivity uncertainty and u_L is the thermocouple distance uncertainty.
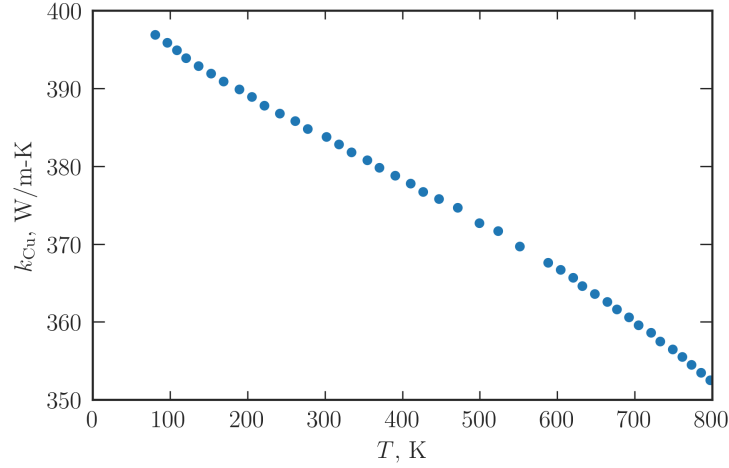
Figure A.1: Variations of the copper thermal conductivity with temperature [131].

The thermal conductivity of copper is calculated employing the data in Figure A.1 and the associated uncertainty is

$$u_k = \left[\frac{\sum (k_{\text{Cu}} - k)^2}{N - (1 + M)} \right]^{1/2}, \qquad \text{(A.9)}$$

where $k_{\text{Cu}}(T)$ is from Figure A.1 data, $k(T) = AT + B$ is the linear curve fit with $N = 42$ as the number of data points and $M = 1$ is the order of the polynomial fit.

The global conductance G/A is defined as

$$\frac{G}{A} = \frac{q}{T_s - Tlg} = \frac{q}{\frac{1}{3} \sum_{i=1}^{3} \left(T_{o,i} - \frac{q}{k_{\text{Cu}}} L_s \right) - T_{lg}}, \qquad \text{(A.10)}$$

therefore its combined uncertainty is

117

$$u_{GA} = \left[\left(\frac{\frac{1}{3}\sum_{i=1}^{3} T_{o,i} - T_{lg}}{\frac{1}{3}\sum_{i=1}^{3} \left(T_{o,i} - \frac{q}{k_{\mathrm{Cu}}} L_s \right) - T_{lg}} \right)^2 u_q^2 + \left\{ \frac{q}{\left[\frac{1}{3}\sum_{i=1}^{3} \left(T_{o,i} - \frac{q}{k_{\mathrm{Cu}}} L_s \right) - T_{lg} \right]^2} \right\}^2 u_T^2 + \right.$$

$$\left. + \left\{ \frac{q}{\left[\frac{1}{3}\sum_{i=1}^{3} \left(T_{o,i} - \frac{q}{k_{\mathrm{Cu}}} L_s \right) - T_{lg} \right]^2} \right\}^2 u_{T,lg}^2 \right]^{1/2}, \tag{A.11}$$

where u_T is the uncertainty of the temperature measuring device and $u_{T,lg}$ is the uncertainty of the saturation temperature, calculated as

$$u_{T,lg} = \left[\left(\frac{\partial T_{lg}}{\partial p} \right)^2 u_p^2 + u_{EOS}^2 \right]^{1/2}, \tag{A.12}$$

where u_p is the pressure measurement uncertainty, u_{EOS} is the uncertainty of the employed equation of states. Usually, it is of a higher order than the other two, therefore, it can be safely neglected. The differential term in Eq. (A.12) can be approximated with the forward differential scheme

$$\frac{\partial T_{lg}}{\partial p} = \lim_{\Delta p \to 0} \frac{T_{lg}(p + \Delta p) - T_{lg}(p)}{\Delta p}. \tag{A.13}$$

The measured and derived expanded uncertainties are indicated in Table A.1. These heat flux and temperature uncertainties are marked as error bars in Figures 10.3 and 10.4.

Table A.1: Expanded uncertainties of relevant measured and derived parameters for $K_r = 1.96$ (95%).

U_T (K)	U_p (kPa)	U_L (mm)	U_A (mm^2)	$U_{T,lg}$ (K)
0.5	2.03	0.20	2140	0.5

$U_{\Delta\varphi}$ (V)	$U_{R,e}$ (Ω)	U_q (MW/m^2)	U_k (W/m-K)	U_{GA} (MW/m^2-K)
0.08	0.006	0.08–0.16	1.37	0.08

<center>**APPENDIX B**</center>

Visualization of Numerically Simulated and Experimentally Observed FBCW Results

Visualization of the phase interactions is a very powerful tool in analyzing two-phase flow. The topology of the phases is identified in video recordings of the FBCW experiments and is used to decipher the flow regime diagrams to support the analyses. The recorded videos are compared with the predicted, visualized phasic behavior for verification of the assumptions and condition used in the DNS.

Here, a series of video recordings from the experiments and the numerical simulations are presented. Each subsection corresponds to a supplementary video. The text in the subsection describes the video. Timestamps and description of relevant events are highlighted.

B.1   Modulation Regimes

B.1.1   Wavelength Modulation Regime

The full video is available at this link and also alongside the print version of this work.

Video B.1.1.mp4 shows the Wavelength Modulation Regime (WMR) in flow boiling for saturate water at one atm. Three heat fluxes at different inlet liquid velocities are shown: (a) $q = 1.35\,\mathrm{MW/m^2}$ and $u_{l,\mathrm{o}} = 0.05$, 0.07 and $0.09\,\mathrm{m/s}$, (b) $q = 1.75\,\mathrm{MW/m^2}$ and $u_{l,\mathrm{o}} = 0.25$, 0.5 and $1\,\mathrm{m/s}$, (c) $q = 3\,\mathrm{MW/m^2}$ and $u_{l,\mathrm{o}} = 1$, 1.5 and $2.5\,\mathrm{m/s}$.

<center>119</center>

0′0″ The vapor site configuration for all nine cases can be seen. Dimensions are scaled based on the largest critical wavelength $\lambda_c = 17.7\,\mathrm{mm}$.

0′6″ The high heat flux, $q = 3\,\mathrm{MW/m^2}$, videos loop. Dryout is observed for the lowest velocity, $u_{l,\mathrm{o}} = 1\,\mathrm{m/s}$.

0′26″ The vapor oscillation passes through the $q = 1.75\,\mathrm{MW/m^2}$ and $u_{l,\mathrm{o}} = 0.25\,\mathrm{m/s}$ video but the surface liquid track does not recover.

0′29″ No leading-edge surface liquid track is observed for the lowest velocity, $u_{l,\mathrm{o}} = 0.05\,\mathrm{m/s}$, and low heat flux, $q = 0.25\,\mathrm{MW/m^2}$.

B.1.2   Geometry Modulation Regime

The full video is available at this link and also alongside the print version of this work.

Video B.1.2.mp4 shows the Geometry Modulation Regime (GMR) in flow boiling for saturate water at one atm. Three vapor site arrangements: staggered circular vapor sites, inline circular vapor sites, and inline rectangular vapor sites. Heat flux $q = 1.75\,\mathrm{MW/m^2}$ and $u_{l,\mathrm{o}} = 0.25\,\mathrm{m/s}$.

0′0″ Vapor site configuration for all three cases can be seen.

0′1″ The liquid track is still observed due to the effect of the liquid flow path for the inline vapor sites configurations.

0′08″ After the vapor oscillation passes through two inline configurations, the surface liquid track is recovered. The liquid track width for the inline rectangular is larger than the inline circular vapor sites by a three-fold figure.

0′21″ The otherwise stable liquid track for the circular, inline vapor sites configuration starts to diminish due to lateral oscillations.

B.1.3 Confined-Geometry Modulation Regime

The full video is available at this link and also alongside the print version of this work.

Video B.1.3.mp4 shows Confined-Geometry Modulation Regime (C-GMR) in flow boiling for saturate water at one atm. Heat flux $q = 10\,\mathrm{MW/m^2}$ and $u_{l,\mathrm{o}} = 0.5\,\mathrm{m/s}$.

0′0″ Vapor site configuration with levees shielding the liquid track in the aqueduct can be seen.

0′1″ Vapor admitted into the flow channel expands laterally above the canopy height $H_l = 3\,\mathrm{mm}$ without disturbing the surface liquid track.

0′02″ Expanding vapor penetrates into the intralevee channel, but does not go beyond $z = 2\,\mathrm{mm}$.

0′09″ Vapor penetrates into the intralevee channel in an oscillatory pattern at the edge of the second row of perforations.

0′13″ Vapor goes further into the aqueduct but does not reach the liquid track plane ($z = 0.25\,\mathrm{mm}$).

0′58″ After another oscillation, vapor recoils, leaving the surface liquid track untouched.

B.2 Flow-Boiling Canopy Wick

B.2.1 Experiment

The full video is available at this link and also alongside the print version of this work.

Video B.2.1.mp4 shows the video recording of the experimental condition in the flow-boiling loop presented in Chapter 9. Saturated water at one atm, $q = 2.1\,\mathrm{MW/m^2}$ and $u_{l,\mathrm{o}} = 0.25\,\mathrm{m/s}$.

0′0″ Side view of the FBCW is shown. The evaporator wick cannot be identified in the frame due to its small thickness. Posts, canopy, and levees can be seen. Vapor escapes through the perforations and above the levees $H_l = 5\,\mathrm{mm}$.

0′03″ The oscillatory vapor pattern observed in the simulations is also seen.

0′08″ Vapor penetrates into the intralevee channel but does not go beyond $z = 4\,\mathrm{mm}$.

B.2.2   Experiments and CFD

The full video is available at this link and also alongside the print version of this work.

Video B.2.2.mp4 shows the comparison of phase distribution from experiments and CFD. Experiments by [124], CFD by [89, 63, 132]. Saturated water, one atm, $q = 2.2$–$2.5\,\mathrm{MW/m^2}$ and $u_{l,\mathrm{o}} = 0.25\,\mathrm{m/s}$.

$0'0''$ Perspective view of the experiment showing the channel and side view of the canopy wick are shown. Perspective view of the CFD domain showing the channel and side view of the canopy wick are shown. Cross-section at $y = 0\,\mathrm{mm}$ (middle of the channel) and $x = 13$, 26 and $39\,\mathrm{mm}$ (after 2, 4 and 6 perforations) are also shown.

$0'03''$ The oscillatory vapor escaping pattern is observed in both recordings.

$0'04''$ Shallow vapor penetration into the intralevee channel is observed for both recordings.

$0'12''$ Wavy liquid-vapor interface in the CFD intralevee channel. The height of surface liquid track reduces axially due to increased vapor-flow shearing. Vapor velocity in the intralevee channel is reduced due to geometric confinement, postponing K-H instability.

B.2.3   CFD

The full video is available at this link and also alongside the print version of this work.

Video B.2.3.mp4 shows the phase distributions and flows above and below the canopy wick for the CFD simulated 2x6 perforations FBCW, with snapshots of the phase distributions along selected axial and lateral locations. Saturated water at one atm, $q = 15\,\mathrm{MW/m^2}$ and $u_{l,\mathrm{o}} = 0.2\,\mathrm{m/s}$.

$0'0''$ Perspective view of the CFD domain showing the channel and wick domains is shown. Cross-section at $y = -1$ and $1\,\mathrm{mm}$ and $x = 13$, 26 and $39\,\mathrm{mm}$ (after 2, 4 and 6 perforations) are also shown.

0′02″ Vapor disturbance of the surface liquid track in the intralevee channel is more pronounced due to the high heat flux $q = 15\,\mathrm{MW/m^2}$. Leading-edge region remains unchanged ($0\,\mathrm{mm} < x < 6.5\,\mathrm{mm}$).

0′08″ Leading-edge liquid track height is affected by the vapor but quickly recovers. Downstream, the interface oscillates but the instability is not triggered due to geometric confinement.

0′21″ Intralevee surface liquid track thins down severely in the downstream region but does not dry.

0′25″ Local dryout in the $y = -1\,\mathrm{mm}$ plane is observed between $x = 26$ and $30\,\mathrm{mm}$.

0′40″ Local surface liquid track recovers and re-wets the canopy. The cross-sectional views at $x = 13$, 26 and $39\,\mathrm{mm}$ show that, although local dryout is observed, the liquid track does not dryout completely along the liquid path, securing the wetting of the canopy.

BIBLIOGRAPHY

[1] G. Hewitt. Ch. 15 - boiling. In Y. I. Cho W. M. Rohsenow, J. P. Hartnett, editor, *Handbook of Heat Transfer*. McGraw-Hill, 1998.

[2] S. Mostafa Ghiaasiaan. *Pool Boiling*, chapter 11, page 287–320. Cambridge University Press, 2007.

[3] L. S. Tong and Y. S. Tang. *Boiling Heat Transfer and Two-Phase Flow*. Taylor & Francis, 2nd edition, 1997.

[4] V. P. Carey. *Phase Stability and Homogeneous Nucleation*, chapter 5, pages 127–168. Taylor & Francis, 1992.

[5] Massoud Kaviany. *Fluid Particle Energy Storage, Transport, and Transformation Kinetics*, chapter 6, page 434–518. Cambridge University Press, 2 edition, 2014.

[6] H. Nariai S. G. Kandlikar. Ch. 15 - flow boiling in circular tubes. In V. K. Dhir S. G. Kandlikar, M. Shoji, editor, *Handbook of Heat Transfer*. Taylor & Francis, 1999.

[7] G. Hewitt. Ch. 8 - introduction and basic models. In V. K. Dhir S. G. Kandlikar, M. Shoji, editor, *Handbook of Heat Transfer*. Taylor & Francis, 1999.

[8] Massoud Kaviany. *Fluid-Fluid Systems*, pages 417–487. Springer New York, New York, NY, 2001.

[9] S. Mostafa Ghiaasiaan. *Flow Boiling*, chapter 12, page 321–370. Cambridge University Press, 2007.

[10] Yasuo Koizumi. Chapter 1 - outline of boiling phenomena and heat transfer characteristics. In Yasuo Koizumi, Masahiro Shoji, Masanori Monde, Yasuyuki Takata, and Niro Nagai, editors, *Boiling*, pages 1–11. Elsevier, Boston, 2017.

[11] Wenxiao Chu, Gang Yan, Hao Zhang, Fufeng Zhao, Qingxian Wang, and Qiuwang Wang. A review on experimental investigations of refrigerant/oil mixture flow boiling in horizontal channels. *Applied Thermal Engineering*, 196:117270, 2021.

[12] Yang Liu, Wei Liu, Long Gu, Jianqiang Shan, Lu Zhang, and Xingkang Su. Existing dnb-type chf mechanistic models and relations with visualized experiments in forced convective flow boiling: A review. *Progress in Nuclear Energy*, 148:104225, 2022.

[13] M.V. Piskunov and P.A. Strizhak. Using planar laser induced fluorescence to explain the mechanism of heterogeneous water droplet boiling and explosive breakup. *Experimental Thermal and Fluid Science*, 91:103–116, 2018.

[14] V. Voulgaropoulos, G.M. Aguiar, C.N. Markides, and M. Bucci. Simultaneous laser-induced fluorescence, particle image velocimetry and infrared thermography for the investigation of the flow and heat transfer characteristics of nucleating vapour bubbles. *International Journal of Heat and Mass Transfer*, 187:122525, 2022.

[15] Matthew J. Rau, Tianqi Guo, Pavlos P. Vlachos, and Suresh V. Garimella. Stereo-piv measurements of vapor-induced flow modifications in confined jet impingement boiling. *International Journal of Multiphase Flow*, 84:19–33, 2016.

[16] Matthew J. Rau, Pavlos P. Vlachos, and Suresh V. Garimella. A tomographic-piv investigation of vapor-induced flow structures in confined jet impingement boiling. *International Journal of Multiphase Flow*, 84:86–97, 2016.

[17] Chirag R. Kharangate and Issam Mudawar. Review of computational studies on boiling and condensation. *International Journal of Heat and Mass Transfer*, 108:1164–1196, 2017.

[18] Manish Dadhich, Om Shankar Prajapati, and Vikas Sharma. A systematic review on the heat transfer investigation of the flow boiling process. *Chemical Engineering and Processing - Process Intensification*, 165:108425, 2021.

[19] D.B. Marchetto, D.C. Moreira, R. Revellin, and G. Ribatski. A state-of-the-art review on flow boiling at high reduced pressures. *International Journal of Heat and Mass Transfer*, 193:122951, 2022.

[20] A. Mariani G. P. Celata. Ch. 17 - CHF and post-CHF (post-dryout) heat transfer. In V. K. Dhir S. G. Kandlikar, M. Shoji, editor, *Handbook of Heat Transfer*. Taylor & Francis, 1999.

[21] SS Kutateladze. On the transition to film boiling under natural convection. *Kotloturbostroenie*, 3:10–12, 1948.

[22] Novak Zuber. *Hydrodynamic Aspects Of Boiling Heat Transfer*. PhD thesis, University of California, Los Angeles, 1959.

[23] J. H. Lienhard and V. K. Dhir. Hydrodynamic Prediction of Peak Pool-boiling Heat Fluxes from Finite Bodies. *Journal of Heat Transfer*, 95(2):152–158, 05 1973.

[24] V. Sernas, J.H. Lienhard, and V.K. Dhir. The taylor wave configuration during boiling from a flat plate. *International Journal of Heat and Mass Transfer*, 16(9):1820–1821, 1973.

[25] Vijay K. Dhir and John H. Lienhard. Taylor stability of viscous fluids with application to film boiling. *International Journal of Heat and Mass Transfer*, 16(11):2097–2109, 1973.

[26] K. Sefiane, D. Benielli, and A. Steinchen. A new mechanism for pool boiling crisis, recoil instability and contact angle influence. *Colloids and Surfaces A: Physicochemical and Engineering Aspects*, 142(2):361–373, 1998.

[27] V. S. Nikolayev, D. Chatain, Y. Garrabos, and D. Beysens. Experimental evidence of the vapor recoil mechanism in the boiling crisis. *Phys. Rev. Lett.*, 97:184503, Nov 2006.

[28] Dong Eok Kim and Junseok Park. Visualization study of phase distribution on a boiling surface. *Experimental Thermal and Fluid Science*, 121:110261, 2021.

[29] Yves Garrabos, Carole Lecoutre, Daniel Beysens, Vadim Nikolayev, Sebastien Barde, Gabriel Pont, and Bernard Zappoli. Transparent heater for study of the boiling crisis near the vapor–liquid critical point. *Acta Astronautica*, 66(5):760–768, 2010.

[30] Shuai Gong, Lenan Zhang, Ping Cheng, and Evelyn N. Wang. Understanding triggering mechanisms for critical heat flux in pool boiling based on direct numerical simulations. *International Journal of Heat and Mass Transfer*, 163:120546, 2020.

[31] Lenan Zhang, Shuai Gong, Zhengmao Lu, Ping Cheng, and Evelyn N. Wang. Boiling crisis due to bubble interactions. *International Journal of Heat and Mass Transfer*, 182:121904, 2022.

[32] Q. Li, Y. Yu, and Z. X. Wen. How does boiling occur in lattice boltzmann simulations? *Physics of Fluids*, 32(9):093306, 2020.

[33] Chong Li, Xiande Fang, and Qiumin Dai. Two-phase flow boiling instabilities: A review. *Annals of Nuclear Energy*, 173:109099, 2022.

[34] Byong Guk Jeon, Moon Hee Choi, Dong Hoon Kam, Young Jung Youn, and Sang-Ki Moon. Observation of departure from nucleate boiling under flow using optical visualization and ir thermometry. *International Journal of Heat and Mass Transfer*, 185:122417, 2022.

[35] Seol Ha Kim, In Cheol Chu, Moon Hee Choi, and Dong Jin Euh. Mechanism study of departure of nucleate boiling on forced convective channel flow boiling. *International Journal of Heat and Mass Transfer*, 126:1049–1058, 2018.

[36] Jean-Marie Le Corre, Shi-Chune Yao, and Cristina H. Amon. Two-phase flow regimes and mechanisms of critical heat flux under subcooled flow boiling conditions. *Nuclear Engineering and Design*, 240(2):245–251, 2010. Twelfth International Topical Meeting on Nuclear Reactor Thermal Hydraulics (NURETH-12).

[37] Kaneyasu Nishikawa. Historical developments in the research of boiling heat transfer. *JSME international journal*, 30(264):897–905, 1987.

[38] Shangzhen Xie, Mehrdad Shahmohammadi Beni, Jiejin Cai, and Jiyun Zhao. Review of critical-heat-flux enhancement methods. *International Journal of Heat and Mass Transfer*, 122:275–289, 2018.

[39] Xiande Fang, Yafeng Chen, Helei Zhang, Weiwei Chen, Anqi Dong, and Run Wang. Heat transfer and critical heat flux of nanofluid boiling: A comprehensive review. *Renewable and Sustainable Energy Reviews*, 62:924–940, 2016.

[40] Gangtao Liang and Issam Mudawar. Review of single-phase and two-phase nanofluid heat transfer in macro-channels and micro-channels. *International Journal of Heat and Mass Transfer*, 136:324–354, 2019.

[41] Sudhir Kumar Singh and Deepak Sharma. Review of pool and flow boiling heat transfer enhancement through surface modification. *International Journal of Heat and Mass Transfer*, 181:122020, 2021.

[42] Gangtao Liang and Issam Mudawar. Review of channel flow boiling enhancement by surface modification, and instability suppression schemes. *International Journal of Heat and Mass Transfer*, 146:118864, 2020.

[43] G. Hwang and M. Kaviany. High-heat-flux distributed capillary evaporators. In Kambiz Vafai, editor, *Handbook of Porous Media*, pages 535–555. Taylor and Francis & CRC Press, 2015.

[44] John R. Thome. Boiling in microchannels: a review of experiment and theory. *International Journal of Heat and Fluid Flow*, 25(2):128–139, 2004. Selected Papers from the 5th ECI International Conference on Boiling Heat Transfer.

[45] E. Manavela Chiapero, M. Fernandino, and C.A. Dorao. Review on pressure drop oscillations in boiling systems. *Nuclear Engineering and Design*, 250:436–447, 2012.

[46] Daxiang Deng, Long Zeng, and Wei Sun. A review on flow boiling enhancement and fabrication of enhanced microchannels of microchannel heat sinks. *International Journal of Heat and Mass Transfer*, 175:121332, 2021.

[47] Christopher Konishi and Issam Mudawar. Review of flow boiling and critical heat flux in microgravity. *International Journal of Heat and Mass Transfer*, 80:469 – 493, 2015.

[48] Behnam Parizad Benam, Abdolali Khalili Sadaghiani, Vedat Yağcı, Murat Parlak, Khellil Sefiane, and Ali Koşar. Review on high heat flux flow boiling of refrigerants and water for electronics cooling. *International Journal of Heat and Mass Transfer*, 180:121787, 2021.

[49] S. Chandrasekhar. *The stability of superposed fluids: the Kelvin-Helmholtz instability*, chapter 11, pages 481–514. International series of monographs on physics. Clarendon Press, 1961.

[50] V. P. Carey. *Transport efects and interface behavior*, chapter 4, pages 85–126. Taylor & Francis, 1992.

[51] Massoud Kaviany. *Carrier Energy Transport and Transformation Theories*, chapter 3, page 119–172. Cambridge University Press, 2 edition, 2014.

[52] H. Kim, J. C. Padrino, and D. D. Joseph. Viscous effects on kelvin–helmholtz instability in a channel. *Journal of Fluid Mechanics*, 680:398–416, 2011.

[53] Scott G Liter and Massoud Kaviany. Pool-boiling CHF enhancement by modulated porous-layer coating: theory and experiment. *International Journal of Heat and Mass Transfer*, 44(22):4287–4311, 2001.

[54] A. Bar-Cohen and A. McNeil. Parametric effects on pool boiling critical heat flux in dielectric liquids. In *Pool and External Flow Boiling*, pages 171–175, 1992.

[55] S. S. Kutateladze and A. I. Leont'ev. Some applications of the asymptotic theory of the turbulent boundary layer. In *International Heat Transfer Conference*, volume 3, pages 1–6, 1966.

[56] J. Weisman and B.S. Pei. Prediction of critical heat flux in flow boiling at low qualities. *International Journal of Heat and Mass Transfer*, 26(10):1463–1477, 1983.

[57] C.H. Lee and I. Mudawwar. A mechanistic critical heat flux model for subcooled flow boiling based on local bulk flow conditions. *International Journal of Multiphase Flow*, 14(6):711–728, 1988.

[58] J.E. Galloway and I. Mudawar. CHF mechanism in flow boiling from a short heated wall—I. Examination of near-wall conditions with the aid of photomicrography and high-speed video imaging. *International Journal of Heat and Mass Transfer*, 36(10):2511–2526, 1993.

[59] J.C. Sturgis and I. Mudawar. Critical heat flux in a long, rectangular channel subjected to one-sided heating-II. Analysis of critical heat flux data. *International Journal of Heat and Mass Transfer*, 42(10):1849 – 1862, 1999.

[60] L.S. Tong. Boundary-layer analysis of the flow boiling crisis. *International Journal of Heat and Mass Transfer*, 11(7):1208 – 1211, 1968.

[61] Cho-Ning Huang and Chirag R. Kharangate. A new mechanistic model for predicting flow boiling critical heat flux based on hydrodynamic instabilities. *International Journal of Heat and Mass Transfer*, 138:1295 – 1309, 2019.

[62] Júlio Ferreira and Massoud Kaviany. Geometric-confinement suppression of flow-boiling instability using perforated wick: Part I CHF and conductance enhancement. *International Journal of Heat and Mass Transfer*, 159:120080, 2020.

[63] Júlio Ferreira and Massoud Kaviany. Geometric-confinement suppression of flow-boiling instability using perforated wick: Part II CHF limits and wick properties. *International Journal of Heat and Mass Transfer*, 159:120079, 2020.

[64] Ian H. Bell, Jorrit Wronski, Sylvain Quoilin, and Vincent Lemort. Pure and pseudo-pure fluid thermophysical property evaluation and the open-source thermophysical property library coolprop. *Industrial & Engineering Chemistry Research*, 53(6):2498–2508, 2014. PMID: 24623957.

[65] ANSYS. *Fluent Reference Manual*, 2009.

[66] R. Balasubramaniam, E. Rame, J. Kizito, and M. Kassemi. Two Phase Flow Modeling: Summary of Flow Regimes and Pressure Drop Correlations in Reduced and Partial Gravity. Technical report, National Center for Space Exploration Research, 2006.

[67] Robert Eymard, Thierry Gallouët, and Raphaèle Herbin. Finite Volume Methods. In J. L. Lions and Philippe Ciarlet, editors, *Solution of Equation in Rn (Part 3), Techniques of Scientific Computing (Part 3)*, volume 7 of *Handbook of Numerical Analysis*, pages 713–1020. Elsevier, 2000.

[68] Stanley Osher and James A Sethian. Fronts propagating with curvature-dependent speed: Algorithms based on hamilton-jacobi formulations. *Journal of Computational Physics*, 79(1):12–49, 1988.

[69] C.W Hirt and B.D Nichols. Volume of fluid (vof) method for the dynamics of free boundaries. *Journal of Computational Physics*, 39(1):201–225, 1981.

[70] G. Tomar, G. Biswas, A. Sharma, and A. Agrawal. Numerical simulation of bubble growth in film boiling using a coupled level-set and volume-of-fluid method. *Physics of Fluids*, 17(11):112103, 2005.

[71] David Youngs. Time-dependent multi-material flow with large fluid distortion. *Num. Method Fluid Dyn.*, 24:273–285, 01 1982.

[72] David Youngs. An interface tracking method for a 3d eulerian hydrodynamics code. Technical report, 1984.

[73] Pierre Sagaut. *Application to Navier—Stokes Equations*, chapter 3, pages 45–81. Springer Berlin Heidelberg, Berlin, Heidelberg, 2006.

[74] Stephen B. Pope. *Turbulent Flows*. Cambridge University Press, Cambridge, 2000.

[75] F. Nicoud and F. Ducros. Subgrid-Scale Stress Modelling Based on the Square of the Velocity Gradient Tensor. *Flow, Turbulence and Combustion*, 62:183–200, 09 1999.

[76] Shanshan Long, Jie Yang, Xiaobing Huang, Guang Li, Weibin Shi, Martin Sommerfeld, and Xiaogang Yang. Large-eddy simulation of gas–liquid two-phase flow in a bubble column reactor using a modified sub-grid scale model with the consideration of bubble-eddy interaction. *International Journal of Heat and Mass Transfer*, 161:120240, 2020.

[77] Yuichi Murai, Xiang qun Song, Takashi Takagi, Masa aki Ishikawa, Fujio Yamamoto, and Junichi Ohta. Inverse energy cascade structure of turbulence in a bubbly flow : PIV measurment and results. *JSME International Journal Series B*, 43(2):188–196, 2000.

[78] Jinhee Jeong and Fazle Hussain. On the identification of a vortex. *Journal of Fluid Mechanics*, 285:69–94, 1995.

[79] Jie-min Zhan, Yu-tian Li, Wing-hong Onyx Wai, and Wen-qing Hu. Comparison between the q criterion and rortex in the application of an in-stream structure. *Physics of Fluids*, 31(12):121701, 2019.

[80] Mahdi Saeedipour, Stefan Puttinger, Nikolaus Doppelhammer, and Stefan Pirker. Investigation on turbulence in the vicinity of liquid-liquid interfaces – large eddy simulation and piv experiment. *Chemical Engineering Science*, 198:98–107, 2019.

[81] Mahdi Saeedipour and Simon Schneiderbauer. Favre-filtered les-vof of two-phase flows with eddy viscosity-based subgrid closure models: An a-posteriori analysis. *International Journal of Multiphase Flow*, 144:103780, 2021.

[82] Minki Kim and Massoud Kaviany. Flow-boiling canopy wick for extreme heat transfer. *International Journal of Heat and Mass Transfer*, 117:1158 – 1168, 2018.

[83] R. Courant, Friedrichs K., and H. Lewy. On the partial difference equations of mathematical physics. *Mathematische Annalen*, 100(1):32–74, 1928.

[84] Syed S. Bukhari, J (Yiannis) Vardaxoglou, and William Whittow. A metasurfaces review: Definitions and applications. *Applied Sciences*, 9(13), 2019.

[85] Tatjana Gric and Ortwin Hess. Chapter 5 - metasurfaces. In Tatjana Gric and Ortwin Hess, editors, *Phenomena of Optical Metamaterials*, Micro and Nano Technologies, pages 131–154. Elsevier, 2019.

[86] Andrew Lininger, Alexander Y. Zhu, Joon-Suh Park, Giovanna Palermo, Sharmistha Chatterjee, Jonathan Boyd, Federico Capasso, and Giuseppe Strangi. Optical properties of metasurfaces infiltrated with liquid crystals. *Proceedings of the National Academy of Sciences*, 117(34):20390–20396, 2020.

[87] Naim H. Afgan, Larisa A. Jovic, Sergey A. Kovalev, and Victor A. Lenykov. Boiling heat transfer from surfaces with porous layers. *International Journal of Heat and Mass Transfer*, 28(2):415–422, 1985.

[88] G.-S. Hwang and M. Kaviany. Critical heat flux in thin, uniform particle coatings. *International Journal of Heat and Mass Transfer*, 49(5):844–849, 2006.

[89] Tong Kyun Kim, Júlio Ferreira, HangJin Jo, and Massoud Kaviany. Flow-boiling canopy wick capillary-viscous limit. *International Journal of Heat and Mass Transfer*, 181:121999, 2021.

[90] D.H. Min, G.S. Hwang, Y. Usta, O.N. Cora, M. Koc, and M. Kaviany. 2-d and 3-d modulated porous coatings for enhanced pool boiling. *International Journal of Heat and Mass Transfer*, 52(11):2607–2613, 2009.

[91] Ömer Necati Cora, Dahye Min, Muammer Koç, and Massoud Kaviany. Microscale-modulated porous coatings: fabrication and pool-boiling heat transfer performance. *Journal of Micromechanics and Microengineering*, 20(3):035020, feb 2010.

[92] G.S. Hwang, M. Kaviany, W.G. Anderson, and J. Zuo. Modulated wick heat pipe. *International Journal of Heat and Mass Transfer*, 50(7):1420–1434, 2007.

[93] D.H. Min, G.S. Hwang, and M. Kaviany. Multi-artery, heat-pipe spreader. *International Journal of Heat and Mass Transfer*, 52(3):629–635, 2009.

[94] G.S. Hwang, Y. Nam, E. Fleming, P. Dussinger, Y.S. Ju, and M. Kaviany. Multi-artery heat pipe spreader: Experiment. *International Journal of Heat and Mass Transfer*, 53(13):2662–2669, 2010.

[95] G.S. Hwang, E. Fleming, B. Carne, S. Sharratt, Y. Nam, P. Dussinger, Y.S. Ju, and M. Kaviany. Multi-artery heat-pipe spreader: Lateral liquid supply. *International Journal of Heat and Mass Transfer*, 54(11):2334–2340, 2011.

[96] Y. Sungtaek Ju, M. Kaviany, Y. Nam, S. Sharratt, G.S. Hwang, I. Catton, E. Fleming, and P. Dussinger. Planar vapor chamber with hybrid evaporator wicks for the thermal management of high-heat-flux and high-power optoelectronic devices. *International Journal of Heat and Mass Transfer*, 60:163–169, 2013.

[97] W. R. Gambill and J. H. Lienhard. An Upper Bound for the Critical Boiling Heat Flux. *Journal of Heat Transfer*, 111(3):815–818, 08 1989.

[98] D. W. Green and R. H. Perry. *Perry's Chemical Engineer' Handbook*. McGraw-Hill, 8th edition, 2007.

[99] Pijush K. Kundu, Ira M. Cohen, and David R. Dowling. Chapter 15 - Compressible flow. In Pijush K. Kundu, Ira M. Cohen, and David R. Dowling, editors, *Fluid Mechanics (Fifth Edition)*, pages 729 – 778. Academic Press, Boston, fifth edition edition, 2012.

[100] Minki Kim and Massoud Kaviany. Multi-artery heat-pipe spreader: monolayer-wick receding meniscus transitions and optimal performance. *International Journal of Heat and Mass Transfer*, 112:343 – 353, 2017.

[101] Massoud Kaviany. *Principles of heat transfer in porous media*. Springer, 2nd edition, 1995.

[102] Ifiyenia Kececioglu and Yuxiang Jiang. Flow Through Porous Media of Packed Spheres Saturated With Water. *Journal of Fluids Engineering*, 116(1):164–170, 03 1994.

[103] J. L. Lage, B. V. Antohe, and D. A. Nield. Two Types of Nonlinear Pressure-Drop Versus Flow-Rate Relation Observed for Saturated Porous Media. *Journal of Fluids Engineering*, 119(3):700–706, 09 1997.

[104] A. J. Ward-Smith, Robert P. Benedict, and Warren M. Hagist. Internal Fluid Flow: The Fluid Dynamics of Flow on Pipes and Ducts and Fundamentals of Pipe Flow. *Journal of Fluids Engineering*, 104(1):129–129, 03 1982.

[105] Kenneth A. Brakke. The surface evolver. *Experimental Mathematics*, 1(2):141–165, 1992.

[106] S. Modak, M. Kaviany, S. Hoenig, and R. Bonner. Numerical analysis of meniscus dynamics in monolayer-wick dropwise condensation. *Numerical Heat Transfer, Part A: Applications*, 76(5):301–322, 2019.

[107] M.C. Leverett. Capillary Behavior in Porous Solids. *Transactions of the AIME*, 142(01):152–169, 12 1941.

[108] G.R. Hadley. Thermal conductivity of packed metal powders. *International Journal of Heat and Mass Transfer*, 29(6):909–920, 1986.

[109] ANSYS. ANSYS Fluent - CFD Software, version 2022 R1, 2022.

[110] Siemens Digital Industries Software. Simcenter STAR-CCM+, version 2020.1, Siemens 2020.

[111] Katherine J. Humphry, Armand Ajdari, Alberto Fernández-Nieves, Howard A. Stone, and David A. Weitz. Suppression of instabilities in multiphase flow by geometric confinement. *Physical Review E*, 79(5):056310, May 2009.

[112] L. Tadrist. Review on two-phase flow instabilities in narrow spaces. *International Journal of Heat and Fluid Flow*, 28(1):54–62, 2007. The International Conference on Heat Transfer and Fluid Flow in Microscale (HTFFM-05).

[113] David Corson, Rajeev Jaiman, and Farzin Shakib. Industrial application of RANS modelling: capabilities and needs. *International Journal of Computational Fluid Dynamics*, 23(4):337–347, 2009.

[114] Tsan-Hsing Shih, William W. Liou, Aamir Shabbir, Zhigang Yang, and Jiang Zhu. A new k-epsilon eddy viscosity model for high reynolds number turbulent flows. *Computers & Fluids*, 24(3):227–238, 1995.

[115] Jie-Min Zhan, Qing Fan, Wen-Qing Hu, and Ye-Jun Gong. Hybrid realizable k-epsilon/laminar method in the application of 3D heaving OWCs. *Renewable Energy*, 155:691–702, 2020.

[116] Qiang Xu, Liang Liang, Yonglu She, Xiangdong Xie, and Liejin Guo. Numerical investigation on thermal hydraulic characteristics of steam jet condensation in subcooled water flow in pipes. *International Journal of Heat and Mass Transfer*, 184:122277, 2022.

[117] D.C. Wilcox. *Turbulence Modeling for CFD*. Number v. 1 in Turbulence Modeling for CFD. DCW Industries, 2006.

[118] J. O. Hinze. *Turbulence*. McGraw-Hill, 2nd ed. edition, 1975.

[119] M. Lesieur. *Shear Flow Turbulence*, pages 121–154. Springer Netherlands, Dordrecht, 2008.

[120] Brian Launder and D.B. Spalding. The numerical computation of turbulent flows. *Comput. Methods Appl. Mech. Eng.*, 103:456–460, 01 1974.

[121] G. Iaccarino, A. Ooi, P.A. Durbin, and M. Behnia. Reynolds averaged simulation of unsteady separated flow. *International Journal of Heat and Fluid Flow*, 24(2):147–156, 2003.

[122] Han Wang, Shunqi Wang, and Daogang Lu. Turbulent flow of water in a 3×3 rod bundle – numerical results from RANS, URANS and LES. *Progress in Nuclear Energy*, 129:103516, 2020.

[123] B.A. Kader. Temperature and concentration profiles in fully turbulent boundary layers. *International Journal of Heat and Mass Transfer*, 24(9):1541–1544, 1981.

[124] Tong Kyun Kim. *Enhancement of critical heat flux in a flow channel with capillary wicking structure*. PhD thesis, Pohang University of Science and Technology, Pohang, 2022.

[125] Osvaldo Oliveira. Langmuir-blodgett films-properties and possible applications. *Braz. J. Phys.*, 22:60–69, 01 1992.

[126] Ho Seon Ahn, Hyungdae Kim, HangJin Jo, SoonHo Kang, WonPyo Chang, and Moo Hwan Kim. Experimental study of critical heat flux enhancement during forced convective flow boiling of nanofluid on a short heated surface. *International Journal of Multiphase Flow*, 36(5):375–384, 2010.

[127] Taeseung Lee, Dong Hoon Kam, Jong Hyuk Lee, and Yong Hoon Jeong. Effects of two-phase flow conditions on flow boiling CHF enhancement of magnetite-water nanofluids. *International Journal of Heat and Mass Transfer*, 74:278–284, 2014.

[128] P. Weber and K. Johanssen. Study of the critical heat flux condition at convective boiling of water: temperature and power-controlled experiments. In *9th International Heat Transfer Conference*, New York, 1990.

[129] Robert J. Moffat. Describing the uncertainties in experimental results. *Experimental Thermal and Fluid Science*, 1(1):3–17, 1988.

[130] Glenn Steele Hugh Coleman. *Detailed Uncertainty Analysis*, chapter 5, pages 131–146. John Wiley & Sons, Ltd, 2018.

[131] P. E. Liley R. W. Powell, C. Y. Ho. Thermal conductivity of selected materials. Technical report, National Standard Reference Data Series - National Bureau of Standards, West Lafayette, IN, 1966.

[132] Júlio Ferreira and Massoud Kaviany. Direct simulation of flow-boiling crisis and its porous-metasurface control for very large dryout limit. *International Journal of Heat and Mass Transfer*, 194:123051, 2022.